Direct Imaging of Ultrafast Charge Carrier Dynamics in Semiconducting Nanowires Using Two-Photon Excitation and Spatially-Separated Pump-Probe Microscopy

Justin Robert Kirschbrown

A dissertation submitted to the faculty of the University of North Carolina at Chapel Hill in partial fulfillment of the requirements for the degree of Doctor of Philosophy in the Curriculum in Materials Science and Engineering.

Chapel Hill
2013

Approved By:

John Papanikolas

Ed Samulski

Richard Superfine

Sean Washburn

Rene Lopez

ABSTRACT

Justin Kirschbrown: Direct Imaging of Ultrafast Charge Carrier Dynamics in Semiconducting Nanowires Using Two-Photon Excitation and Spatially-Separated Pump-Probe Microscopy
(Under the direction of Dr. John M. Papanikolas)

The increasing use of nanoscale materials in scientific research and device design places a greater emphasis on characterizing the heterogeneity of nanostructures. When designing electronic components around the use of individual nanoparticles, it is important to understand variability between seemingly identical particles produced in the same synthesis. To do this, we have developed an ultrafast optical microscope capable of studying single nanostructures with spatial resolution of hundreds of nanometers. Emission images of zinc oxide needle-like nanowires show a modulated pattern along the long axis of the wire that are attributed to the coupling of the optical field into structurally dependent resonance modes. Simulations suggest that these are size dependent hybrid modes, containing character of both whispering gallery and Fabry-Perot modes. By incorporating transient absorption pump-probe techniques into the microscope design, we can observe the recombination dynamics of excited carriers on femtosecond timescales following excitation. Due to the high resolution of the instrument, it is possible to observe the dynamics at different locations within a single nanostructure. This technique is used to study the correlation between the decay kinetics of silicon nanowires and doping density for a variety of surface treatments. The motion of excited carriers in silicon nanowires was directly imaged by holding the pump beam in a particular

location and scanning the probe beam over the entire structure. The resulting images show free carriers spreading out from the area of excitation, leaving the immobile trapped carriers behind.

To my fiancée, my parents, and my brother.

ACKNOWLEDGEMENTS

First of all, I would like to express my deepest gratitude to my advisor Dr. John Papanikolas for his invaluable input and advice on topics not only concerning science, but also life in general. I would also like to thank Dr. Ralph House and Dr. Brian Mehl for their initial development of the microscope, and for taking me under their wings when I first joined the Papanikolas group. Their instruction and friendship were of the utmost importance to my success. I would like to thank Michelle Gabriel for her collaboration on these projects, and for helping to make the oft mundane task of data collection entertaining. I would also like to thank the other members of the Papanikolas group, past and present; especially Stephanie Bettis, Dr. Erik Grumstrup, Emma Cating, Scott Barnes, Chuan Zhang, Dr. David Zigler, and Dr. Kyle Brennaman. Additional recognition is required for Dr. James Cahoon and his research group, for providing silicon nanowire samples and helping me to better understand their growth process. I consider myself very fortunate to have had the pleasure to work with such wonderful people.

I also wish to express my gratitude to my mother and father, Cindi and Len Kirschbrown, as well as my brother David, for their support and encouragement throughout the course of my study. Most importantly, I would like to offer my special thanks to my fiancée, Dr. Whitney Caron, for standing by me throughout this entire process. Her strength and support made this accomplishment possible.

TABLE OF CONTENTS

LIST OF TABLES

LIST OF FIGURES

LIST OF ABBREVIATIONS

AFM	atomic force microscopy
AOM	acousto-optic modulator
BE	band edge emission
BS	beamsplitter
CCD	charged-coupled device
DC	direct current
DFG	difference frequency generation
EHP	electron-hole plasma
FDFD	finite difference frequency domain
FDTD	finite difference time domain
FP	Fabry-Pérot
IMP	Instrument Management Platform
LBO	lithium triborate
MCP	microchannel plate
NA	numerical aperature
NSOM	near-field scanning microscopy
OPO	optical parametric oscillator
PLL	phase-locked loop
PMT	photomultiplier tube
PSD	phase sensitive detector
RF	radio frequency
SEM	scanning electron microscopy

SFG	sum frequency generation
SHG	second-harmonic generation
SOPP	spatially-overlapped pump-probe
SRV	surface recombination velocity
SSPP	spatially-separated pump-probe
STM	scanning tunneling microscopy
TEM	transmission electron microscopy
UNC	University of North Carolina
WGM	whispering gallery mode

CHAPTER 1. INTRODUCTION

A great deal of materials research is shifting away from investigating properties of bulk structures and focusing more heavily on studying the properties of nanoscale structures. This puts greater emphasis on techniques that investigate the electrical and optical characteristics of single particles over ensembles. To date, few techniques have emerged that can achieve spatial resolution needed to investigate different regions within single particles. Techniques such as scanning-electron (SEM) and transmission electron (TEM) microscopy use electron beams to image, leading to resolutions in the nanometer range, however, achieving high temporal resolution proves to be more difficult and costly[(1)]. Near field scanning optical microscopy (NSOM), scanning tunneling microscopy (STM), and atomic force microscopy offer nanometer scale methods of probing[(2-4)]. However, not only are these techniques complex and often expensive, but incorporation into a pump-probe experimental configuration is not straightforward.

The introduction of femtosecond pulsed lasers allows for the development of pump-probe techniques with take advantage of intense, diffraction-limited excitation with temporal resolution on the order of the pulse duration. By bringing together far-field optical microscopy techniques and femtosecond laser excitation, we have developed an instrument capable of studying regions within a single particle with spatial resolution of ~300-400 nm and ~300 femtosecond time resolution. The instrument is capable of optically exciting the sample in one location and probing the response in another at a later

time. The instrument is controlled by a custom-written software package which integrates and synchronizes all of the components during operation.

The organization of this thesis is as follows: Chapter 2 contains an overview of the overall experimental setup. This discusses some of the more important components of the microscope along with its characterization. Chapter 3 discusses the software design, and acts as both a user manual and development guide for future users. Chapter 4 discusses the role of optical modes in the hexagonal cross-section of tapered zinc oxide nanostructures. This is addressed by comparing FDFD simulations to images collected via the two-photon excitation imaging capabilities of the instrument. Chapter 5 discusses the direct observation of the motion of excited carriers in single silicon nanowires using spatially-separated pump-probe microscopy. Lastly, chapter 6 discusses the effects of doping level and surface passivation on carrier lifetime in silicon nanowires.

CHAPTER 2. EXPERIMENTAL

2.1. Microscope Layout

The experimental setup consists of a complex arrangement of optical and mechanical devices organized on a vibrationally-damped optical table. A schematic diagram of the experimental setup is shown in Figure 1. The pump and probe beams are derived from a combination of two lasers and an oscillator, allowing tuning from 350 nm-1900 nm. This system is explained in greater detail in previous publications from our group[(5)], but a brief overview is provided here.

The femtosecond laser source consists of a mode-locked Ti:Sapphire laser (L2, Spectra-Physics: Tsunami) pumped by a solid-state diode-pumped Nd:YVO_4 laser (L1, Spectra-Physics: Millennia Pro-15sJ). The output of the Ti:Sapphire laser consists of a tunable (700-1000 nm) laser pulses that are approximately 80 fs in duration with a repetition rate of 80.4 MHz. This output alone can be used as an excitation source for emission imaging experiments, or part of it can be picked off for use in pump-probe experiments. In the case of the latter, the un-picked portion of the beam is sent into an optical parametric oscillator (OPO, Spectra-Physics: Opal). The OPO takes advantage of parametric down conversion to generate tunable (1.1-1.9 μm) pulses that are around120 fs in duration.

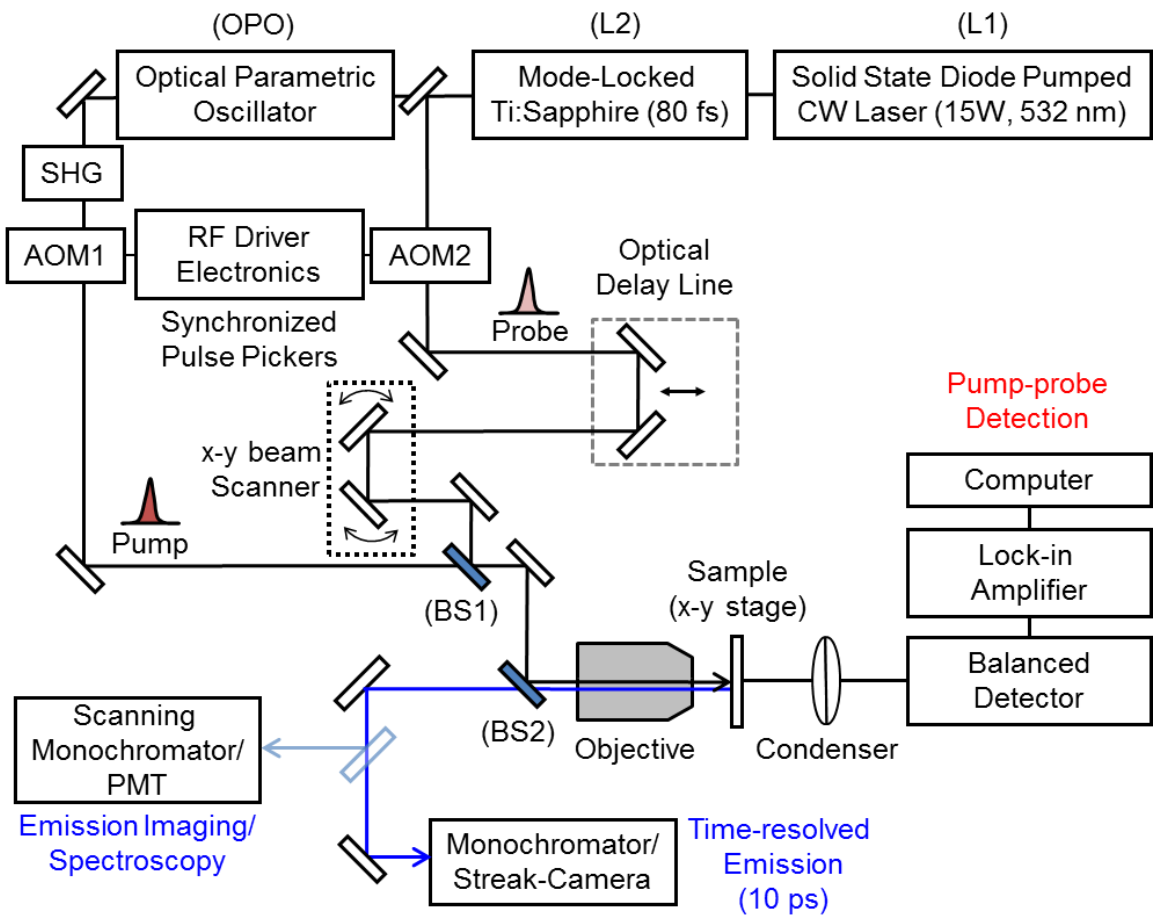

Figure 1: Schematic of the spatially-separated pump probe microscope.

To allow for observation of longer kinetics, the time between pulses is increased by focusing each beam through one of two synchronized acousto-optic modulators (AOM1 and AOM2, Gooch and Housego). The pump beam is modulated (50% duty cycle) by the acousto-optic modulator. The pump passes through a dichroic beamsplitter (BS1) and is directed into the 50x objective (Olympus, NA=0.8) focusing it on the sample. Before the probe beam gets to the objective, it must first go through the delay line and x-y beam scanner.

To control the delay time between the pump excitation and the arrival of the probe beam at the sample, the probe beam is sent into the optical delay line, consisting of a

retro-reflector mounted to a motorized linear stage (Newport: ILS250CCHA). This increases the distance that the probe must travel to reach the sample, resulting temporal resolution on the order of hundreds of femtoseconds.

The probe beam is then sent through the x-y beam scanner, consisting of two mirrors controlled by linear actuators (Newport: CMA-25CCCL). The mirrors are configured to work as a master-slave pair. This concept is illustrated in Figure 2.

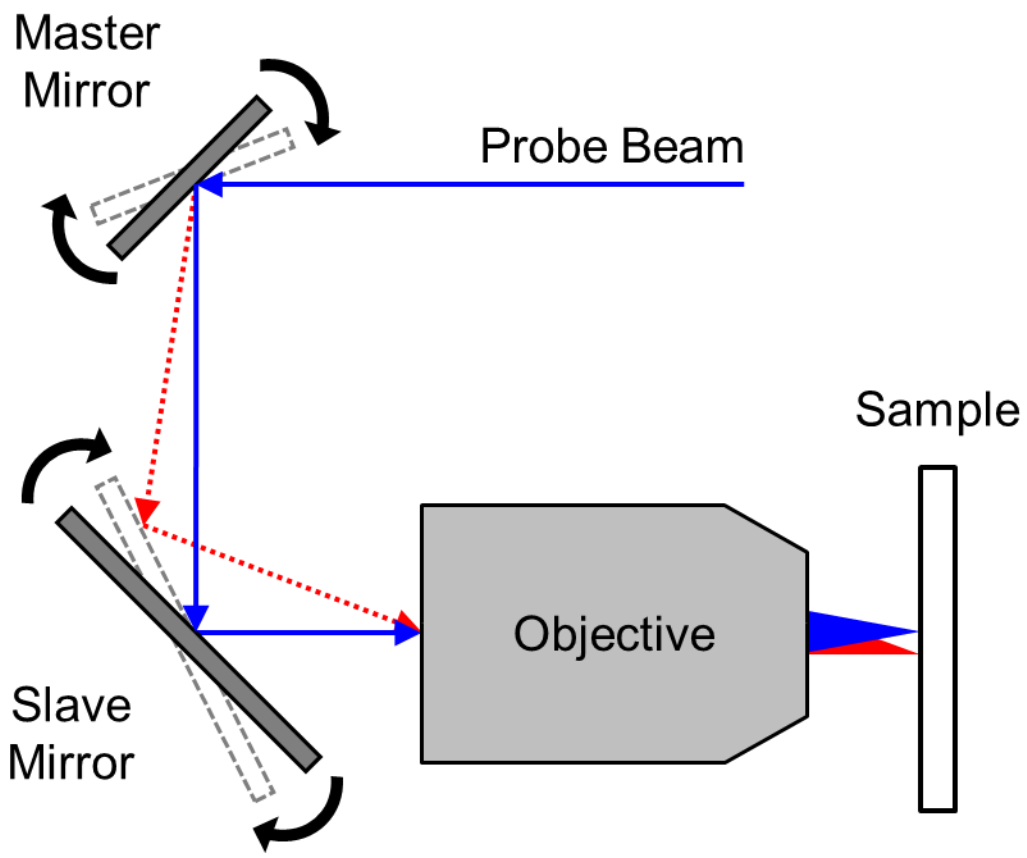

Figure 2: Schematic of the operation of the x-y beam scanner.

The first mirror in sequence (master mirror) is used to change the angle of the beam, and the second mirror (slave mirror) is used to redirect the beam onto the opening on the back of the objective. By passing through the center of an infinity corrected objective at an angle, the focused beam from the front of the objective will translate laterally along

the sample. Only the probe is exposed to the x-y beam scanner, which allows it to be spatially separated from the pump. Imaging with the x-y beam scanner involves moving the master and slave in a synchronized manner. The master mirror is scanned at a constant velocity and the slave mirror compensates to keep the beam centered on the back of the objective.

After the x-y beam scanner, the probe beam rejoins the pump beam after reflecting off the dichroic beam splitter (BS1) and is sent into the objective.

The pump and probe beams interact with the sample and the resulting signal can be collected in both forward and backward directions. In the forward scattered direction, a condenser focuses the probe light onto a balanced detector. The signal from the balanced detector goes into a lock-in amplifier to obtain the pump-induced change in the probe intensity, ΔI. In the backward scattered direction, the light can be directed into one of two possible detectors: a time-resolved streak camera, or through a monochromator and onto a photomultipler tube (PMT).

2.2. Instrument Management Platform (IMP) Software

2.2.1. Overview

Scientific experimentation consists of methodical execution of a procedure that involves controlling and changing relevant parameters, collecting data, and interpreting the results. It is a complex and fluid process that often requires an ever-changing array of tools, which makes capturing it in software a challenge. The main idea behind this software was to give users the ability to plan an experiment, write a custom experiment class type that executes it, and analyze the results. To accomplish this, the software must manage everything from controlling the individual components of the microscope to collecting and organizing the data.

To operate and synchronize the vast number of physical components present in the instrument a custom software architecture named IMP (**I**nstrument **M**anagement **P**latform) was written using the Matlab programming language. The aims of the software design are as follows:

- A bottom-up approach should be taken to maximize reusability of the code. Classes should be designed in a way that ensures that complex elements of the code are composed of the simplest possible sub-elements.
- Users need a level of control that does not limit experiment design. This means control of all equipment must be achievable while maintaining a simple command structure.
- Instruments of the same type (i.e. monochromators) should be interchangeable inside experiment objects with no reprogramming necessary. As the equipment is upgraded or changed, this will allow for seamless transition.

After consideration, we could best accomplish these aims by designing software that takes advantage of the object-oriented architecture of MATLAB. MATLAB is a highly documented, non-compiled language, making it easy for future users to both understand the existing code and develop it further. This reduces the learning curve and gives the software the flexibility required to keep up with experimentation in the academic environment, where the set of users is constantly changing.

The choice to develop the software using an object-oriented model was based on the need to define a strict set of rules for each type of equipment. This ensures interchangeability of objects of the same type, as well as defining the commands that are needed when new equipment of that type is introduced in the future. Furthermore, objects inherently result in compartmentalization of information, which aids in the bottom-up design. Each object contains only its own information, but copies can be created, used, and deleted as needed. This allows multiple different complex elements of the software to have access to the information without having to repeatedly type the same code into each one. As a result, complex elements can be broken into their simplest parts.

2.2.2. Object Oriented Software

Object oriented programming focuses on developing programs based on the interaction of units known as objects. For lack of a better definition, an object is an instance (or realization) of a class. In this way, a class can be thought of as a template for creating objects of that type. This concept is illustrated in Figure 3.

The Dog class in Figure 3 is a template for creating a dog object, and as it will contain properties and methods of a dog object. It has three properties associated with it: Gender, Size, and Nose. The Nose property is assigned the value of “wet” by default, but the other

properties remain unassigned. There are also three methods associated with its definition: Sit, Roll_Over, and Speak. Methods are identical to functions, except that are specifically used only when referencing an object of the class type in which they are defined. For example, if a cat class was also created and it contained a Speak method, a dog object and a cat object would each have its own unique version of the speak method. This is further explained later when discussing inheritance in objects.

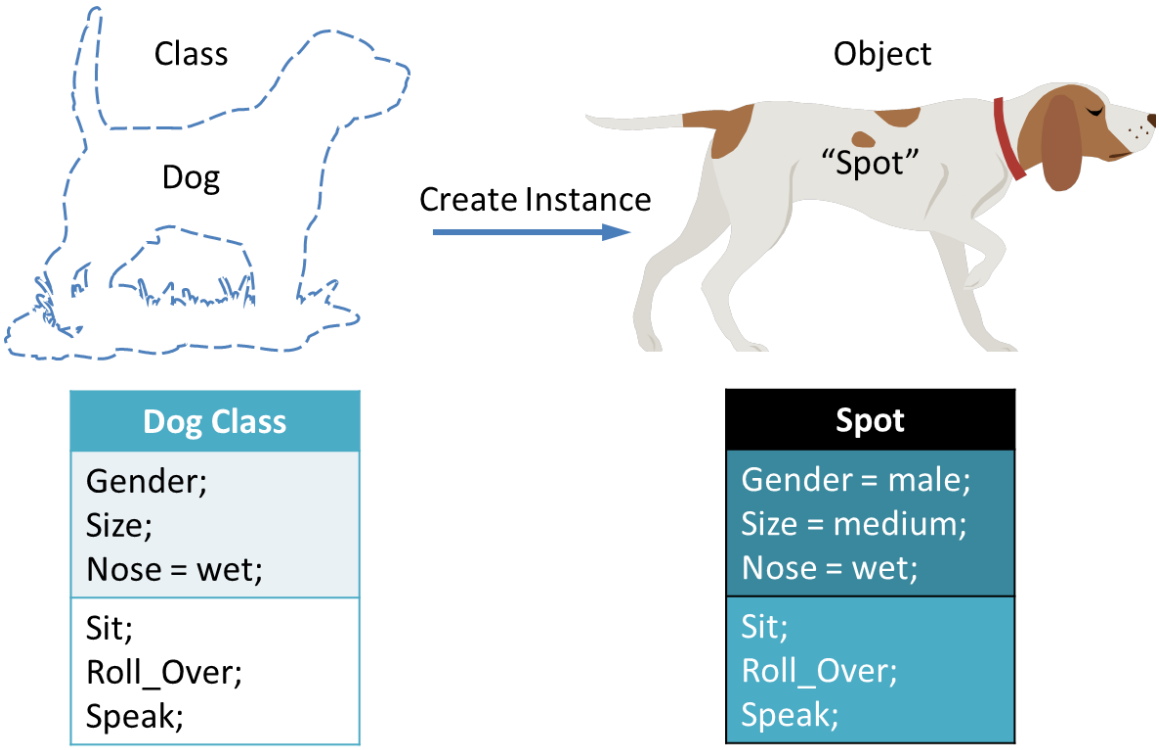

Figure 3: Demonstration of classes and objects. The "Dog" class is shown on the left and provides a template for the object "Spot".

All of the properties grouped together with the methods that control how it "behaves" define the Dog class type. The computer stores all of the property values in its memory as a group, and will reference the methods of the dog class when needed. Multiple dog objects can be created from the dog class, and each can be assigned its own unique value for Gender and Size. While all of the created objects will have the default Nose property

of “wet”, this can even be changed within the individual dog objects. However, any dog objects that are created will share the same set of methods of roll_over, sit, or speak.

In Figure 3, Spot is an example of an object created from the Dog class type that has been assigned the traits of “male” gender and “medium” size. If a command of roll_over, sit, or speak is addressed to Spot, it will react as defined by the Dog class. Spot’s unique property values are the only thing that sets him apart from any other object of type Dog, which may work for describing simple systems. However, as the system complexity increases there may be a need to have different objects that share some properties and methods, but have other properties and methods that are unique. To handle this, objects can take advantage of inheritance.

2.2.2.1. Class Inheritance

Complex object-oriented architectures take advantage of class inheritance to group similar classes which may share properties and methods. This is illustrated in Figure 4 by expanding upon the previous Dog class example to include dog classes to represent different breeds.

In this example, there is a class for a “p_Dog” object, and two other classes for “c_Pitbull” and “c_Pointer” objects. They are linked by an inheritance relationship that establishes that p_Dog is a parent class for c_Pitbull and c_Pointer. The “p” and “c” before the class names is a common notation to represent that they are parent or child classes, respectively. What this relationship means is that when a child object (c_Pitbull

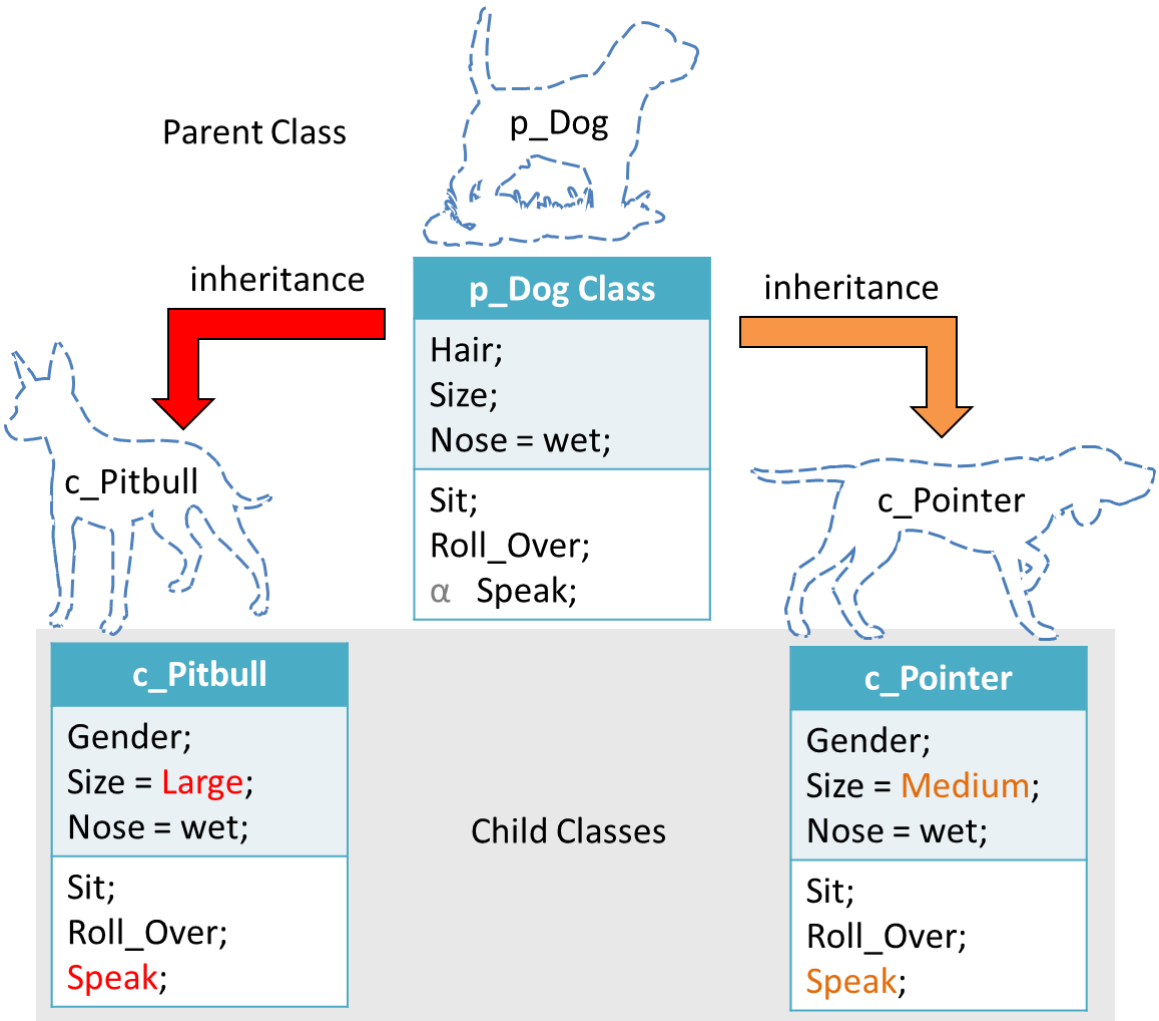

Figure 4: Demonstration of the concept of inheritance. The child classes (c_Pointer and c_Pitbull) inherit properties and methods from the parent class (p_Dog). The Size property and the Speak method are uniquely defined in each child class.

or c_Pointer) is created, they inherit all properties and methods from their parent object (p_Dog).

Looking at the p_Dog class, the Speak method is now listed as an abstract method (symbolized by the α-symbol). Abstract methods are methods that are listed in the parent class, but are not defined until the child classes. This means that a method for Speak must exist for an object to be a valid Dog object, but the actual execution of that method will be defined by each child class individually. If a Speak command is issued to a c_Pitbull

object, it will have a different behavior than if a Speak command is issued to a c_Pointer object. This is useful for interchangeability of objects within the software architecture. If a program is written around making a c_Pitbull object Speak, it will still work if that is replaced with a c_Pointer object. The execution of the Speak command may differ, but the definition of how to execute the command is defined separately in each object.

While this same effect could be created by fully writing a new class every time, the other commands for Sit and Roll_Over are the same for c_Pitbull and c_Pointer objects. By storing these commands in the parent class, it is not necessary to make multiple copies of identical programming code in several locations. This saves programming memory and makes the modifying of shared methods less confusing. Any changes in the parent class method will affect all child classes as opposed to having to change the method in each child class individually.

Inheritance also helps to ensure consistency amongst newly created class types by defining the requirements of their design. If a new c_Chihuahua class was designed, it would require a Speak method to be included in its class definition. Because it is defined as an abstract method in the parent class, its existence is required in any child classes. This strict rule ensures that classes with similar parents are interchangeable within the software. For example, the aforementioned program written around making the c_Pitbull object execute the Speak method would not work with the c_Chihuahua class because it has no Speak method. This situation would create problems in the introduction of new class types into the existing software. By preventing this, inheritance acts as a system of checks and balances.

2.2.2.2. Handle Versus Value Objects

At their core, objects are merely complicated data structures in the memory of a computer program. Multiple copies of the same object can be created, changed, and further copied without consequence. However, when they begin to represent and control a physical entity having multiple copies is counterintuitive. In the Matlab language, this is managed by the existence of two distinct types of objects: value objects and handle objects. This concept is illustrated in Figure 5.

In Figure 5, a Switch Object is shown that contains only one property called State. The State property can be either “On” or “Off”, and let’s imagine that the Switch object has been designed to communicate with a real switch outside of the computer. If the user changes the State property in the object, the real switch will change. In this way, the user can control the real switch through the computer by interacting with the object. The State property of the Switch object represents the state of the real switch.

When another object or function needs to use the Switch object, the software must pass a copy of the original Switch object into it. If two copies are made of same object, the way each copy is treated as the object is changed depends on whether it is a handle object or value object. In the top of Figure 5, a copy of the Switch object with the State set to “On” is made. As the State is set to “Off” in the copy the handle case object also reflects that change, while in the value case object remains in the “On” State.

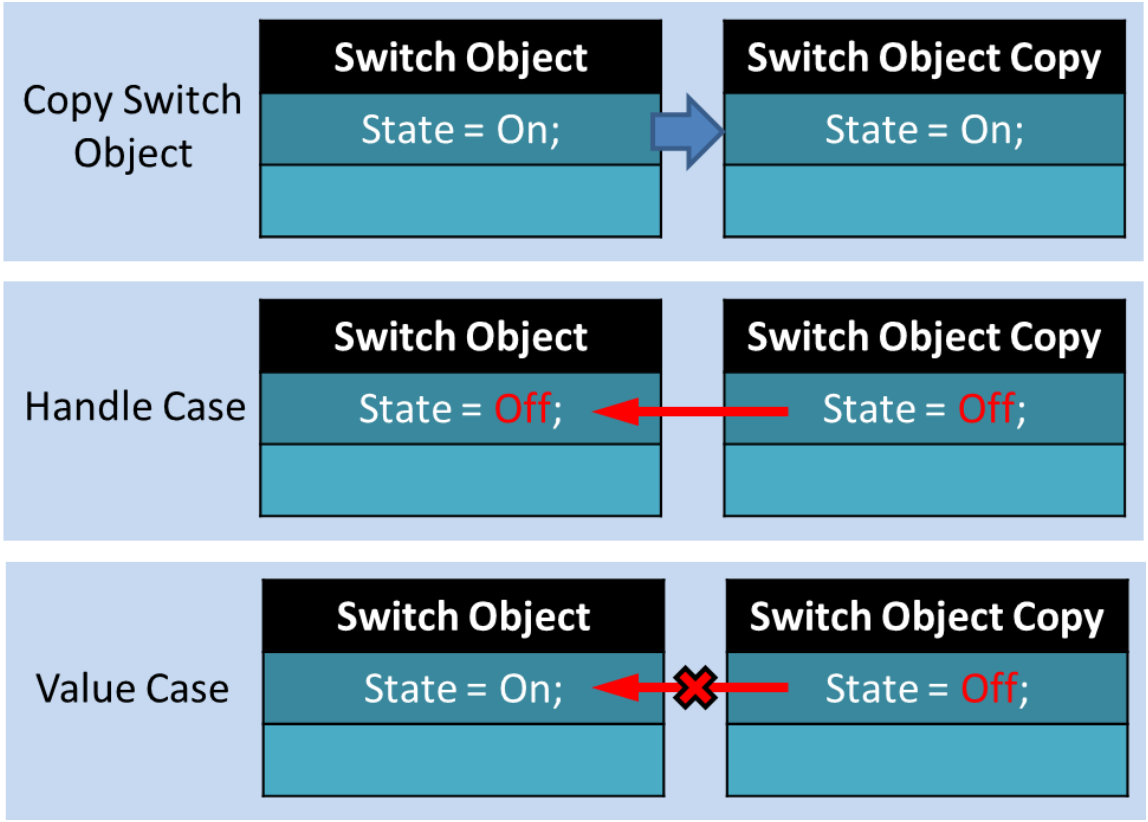

Figure 5: Demonstration of MATLAB handle and value classes with a switch object. State changes are linked in all copies of handle objects, but independent in value classes.

What this means is that in the case of handle objects, there is effectively only one object that exists. As copies are made, they are only just referencing the original object. In other programming languages this is known as creating and reading "pointers", and each object type has its purpose. When representing a physical entity such as in the Switch example, the real switch can only exist in one state at a time, and thus it would be counterintuitive to allow individual copies to have their own value for State. Therefore, it would likely be best to represent it as a handle class.

2.2.2.3. Relating These Concepts to IMP

All of the tools needed to conduct experiments exist in the software as objects, and similar objects are grouped and defined by parent classes. Some objects represent

physical tools (motion controllers, DAQ cards, etc.) while others represent abstract computer constructs that are necessary tools of the experiments.

By designing parent classes for each type of equipment needed for the operation of the instrument, a strict set of properties and abstract methods is assigned to all devices of that type. While the specific operation of the device may be different, the same set of properties and methods are used to interface with them, making them virtually interchangeable. This layout is demonstrated with an abbreviated Monochromator class diagram in Figure 6.

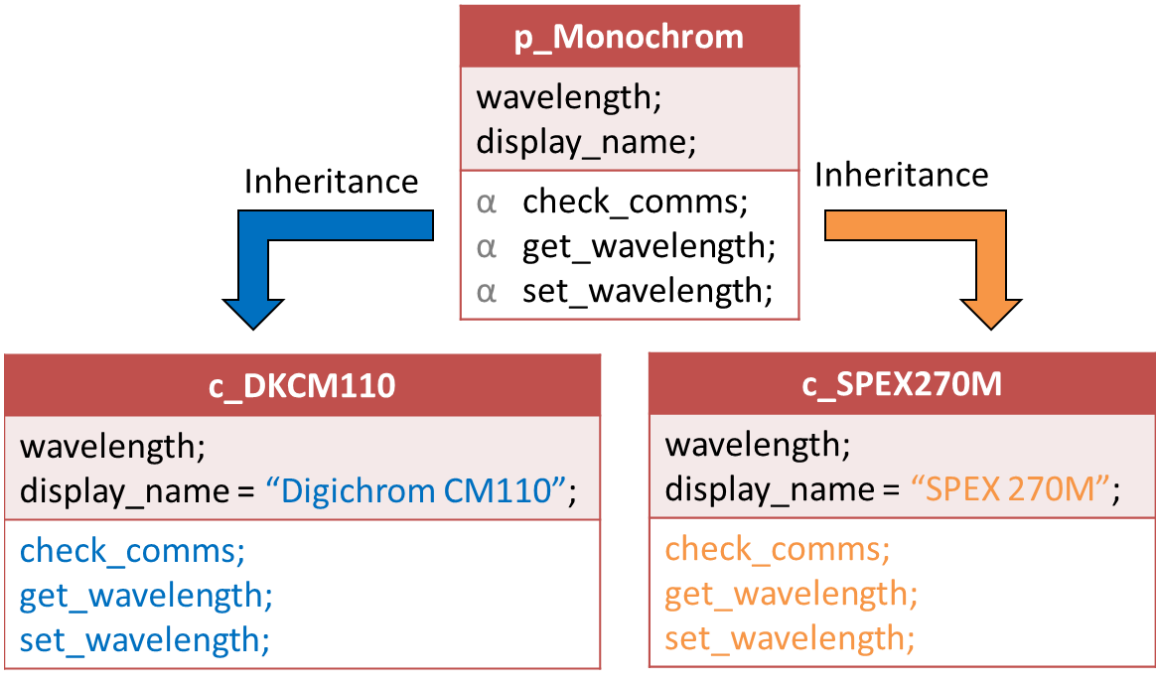

Figure 6: Inheritance relationship for the monochromator equipment type object. The p_Monochrom parent class defines the functions that are required of the child classes, while the child classes dictate how a particular instrument executes the commands.

The parent class p_Monochrom defines the functions that are required for an object to be a valid monochromator object in the software. The parent class defines, via abstract functions, that there must be a check_comms, get_wavelength, and set_wavelength function defined in any child class. The details as to how the Digikrom CM110 and the

SPEX 270M actually perform these actions are drastically different, but the user will use the exact same function regardless. If an experiment is designed around one type of monochromator, any other valid monochromator object can easily replace it. Due to the shared set of methods and properties defined in the parent class, no changes to the programming would be necessary.

2.2.3. Software Class Layout

The software consists of six main categories of objects: framework, equipment, equipment component, experiment, experiment component, and data objects. The general software layout is shown in Figure 7.

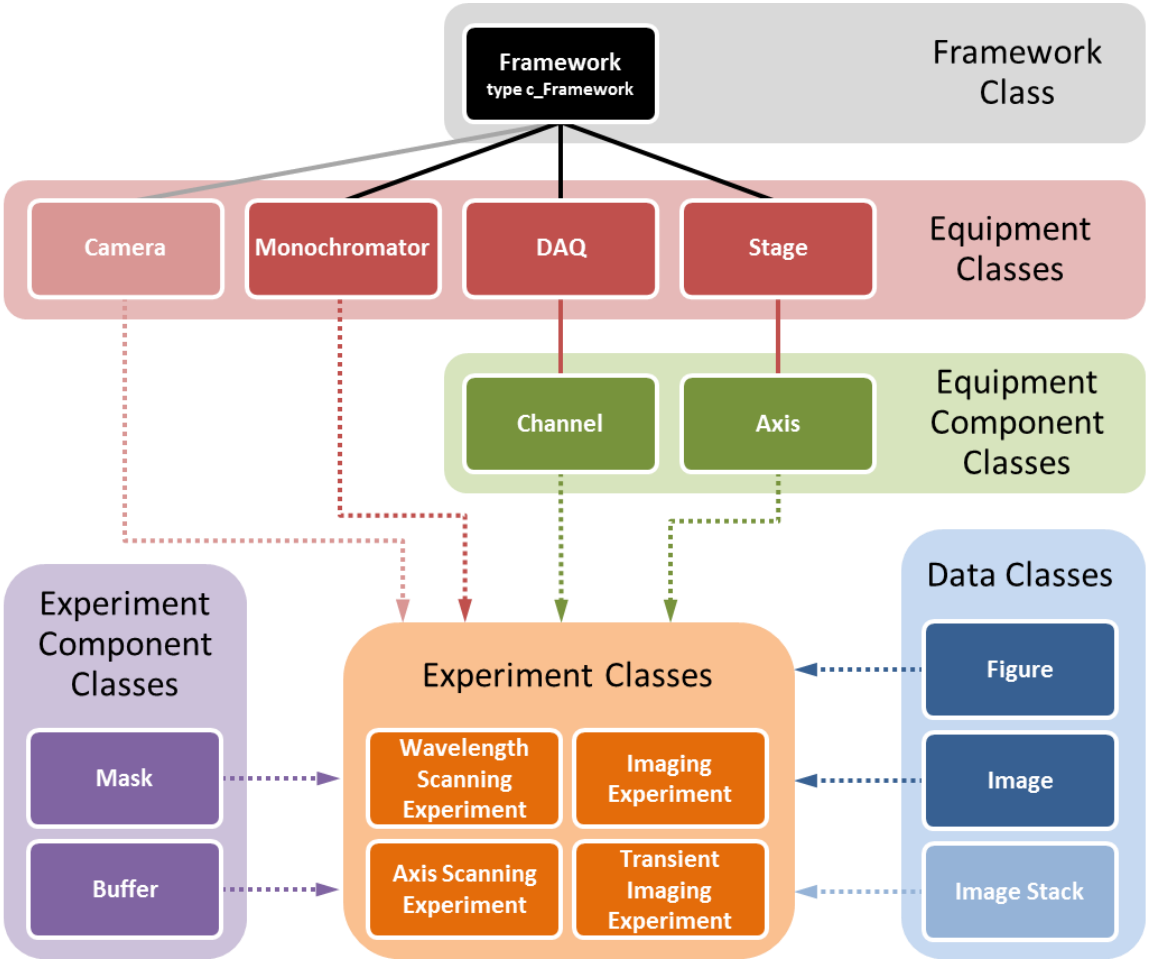

Figure 7: Layout of the organizational structure of classes in the software. Each class type plays an important role in the execution of the experiments.

2.2.3.1. Framework Object

The framework object is the organizational backbone for the entire software platform. On startup, it initializes and stores all of the equipment and equipment component objects available to the experimenter. Because the equipment objects need to be accessed by multiple experiments, having them in a single location provides an easy way for experiment classes to reference them.

By passing a copy of the framework into an experiment object, all of the available equipment is also passed into it. The framework class definition is shown in Figure 8.

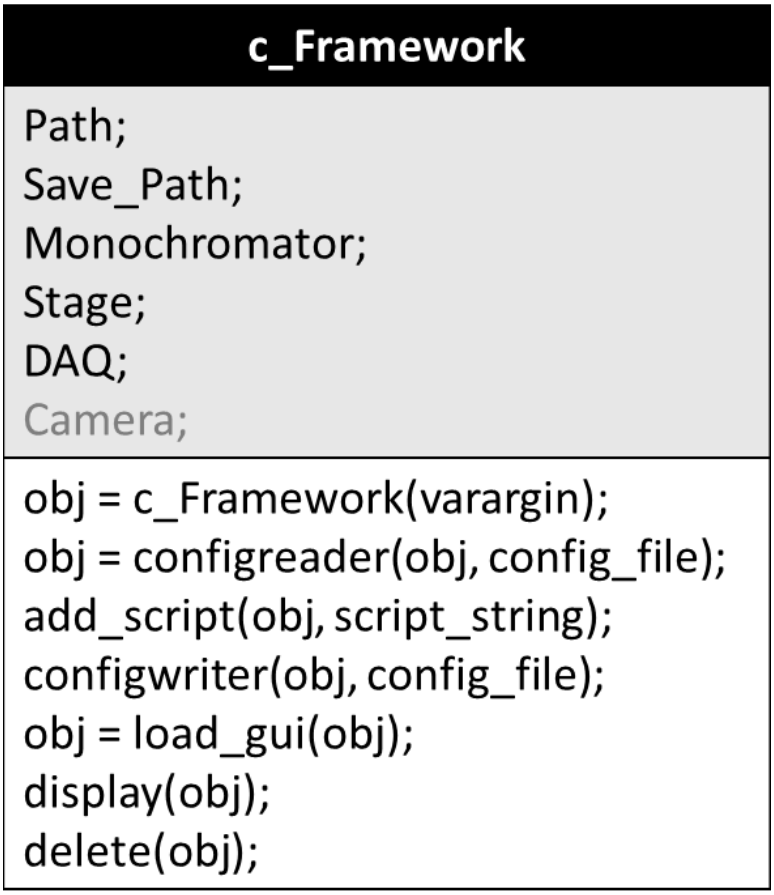

Figure 8: Class layout for the Framework class.

All equipment objects of the same type are stored in a cell array in the appropriate object property. There are currently four properties for storing equipment in the framework object: Monochromator, DAQ, Stage, and Camera. The Camera equipment type is under development, and thus is currently empty. Referencing equipment in the framework object is done in the same manner as referencing an object property in Matlab. For example, if the framework object is named “frame”, the first monochromator loaded by the framework would be located at: frame.Monochromator{1}.

The initial equipment setup is handled by the framework object by passing it a configuration file. This simplifies the day to day initialization of the system because the equipment available to the user will likely remain unchanged for long periods of time. However, the initialization can be changed easily as needed, or customized for different table configurations. While the software was written with this microscope in mind, it will eventually replace all the instrument control software in the lab, and be used to control any future instruments. The software has been adapted for use on 3 different optical tables in lab, each of which requires a unique configuration file.

2.2.3.2. Equipment and Equipment Component Objects

Equipment objects control the physical components that make up the microscope. This includes monochromators, motion controllers, and data acquisition (DAQ) cards. Their properties consist of useful parameters that are commonly associated with the type of equipment they represent. Because they represent physical entities, all equipment and equipment component objects are handle objects.

Equipment objects also have a property which contains the interface used by the computer to communicate with the physical component. This interface is often through a

serial port, Ethernet port, or dynamic linked library (dll). There are currently 3 types of equipment classes: Monochromator, DAQ, and Stage. The Camera equipment class is currently under development.

Equipment Component objects are objects that represent the controllable sub-units of equipment objects. In the case of the Stage and DAQ classes, there are multiple channels that may need to be addressed separately for use in experiments. In these cases, the equipment object handles any communication and data interpretation, while the user directly addresses the equipment component objects.

For objects of the Stage type, the sub-units are referred to as Axis objects and each controls a motion axis on the motion controller. For objects of the DAQ type, the sub-units are referred to as channel objects and are a configurable analog or digital IO channel on a data acquisition device.

Monochromator equipment objects refer to all of the available devices for spectral control. These are typically monochromators, but the c_Filter child class allows for the user to manually enter the wavelength for reference by other classes and methods. The Monochromator parent class, p_Monochrom, is shown in Figure 9. The description and available monochromator child classes are summarized in Table 1.

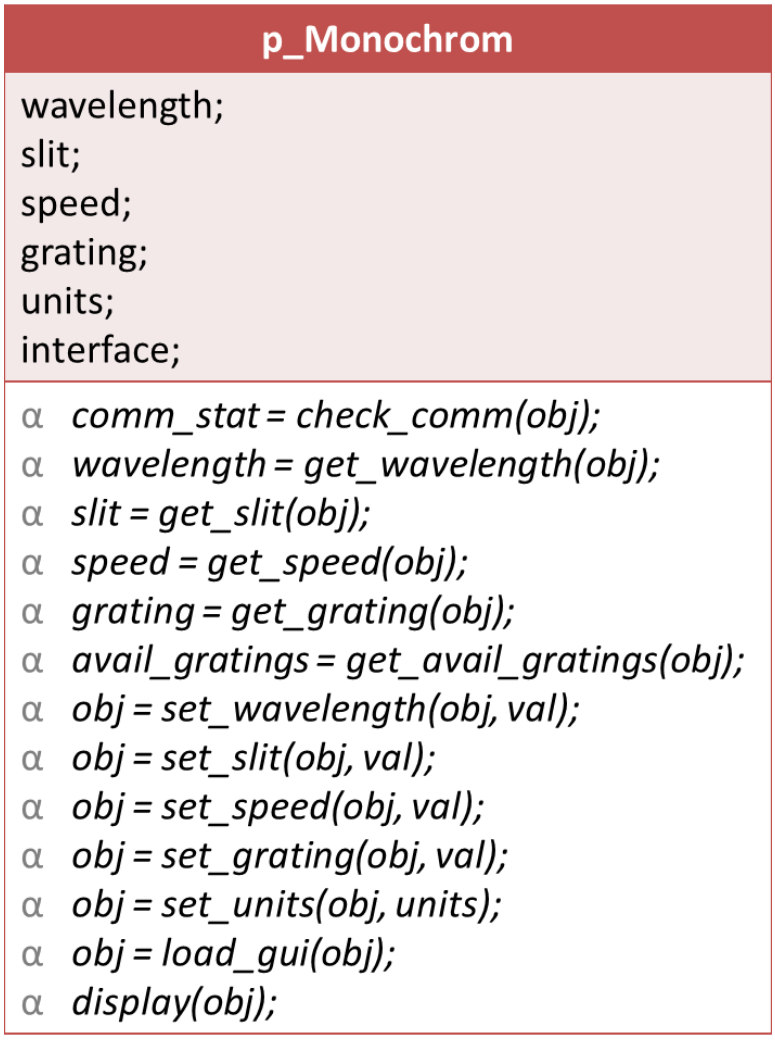

Figure 9: Class layout for the parent Monochromator class.

Table 1: Monochromator class summary.

p_Monochrom Object

Property	Type	Description
Wavelength	double	Current wavelength.
Slit	double	Current slit width.
Speed	double	Current speed.
Grating	uint	Current grating number.
Units	string	Current unit setting.
Interface	varies	Interface object for monochromator (typically serial port object).

Method	Description
check_comm	Checks the communication with the monochromator, returns true if successful and false if not.
load_gui	Opens the GUI for the monochromator object (if available).
display	Standard display function. Shows GUI (if loaded).
get_(property name)	Queries the monochromator device for the current state of the specified property and returns it. Get functions have been linked in the parent class so that they are run if referenced directly (e.g. object.slit returns slit width).
set_(property name)	Sets the specified property for the monochromator device to the value "val". Also works if referenced directly (e.g. object.units = 'nm' would set the units to nanometers).

Child Monochromator Classes

Instrument	Class	Additional Methods
Digikrom CM110	c_DKCM110	none
Digikrom 240	c_DKCM240	read_monocrom(obj)
Optical Filter	c_Filter	none
Princeton Instruments SP-2150i	c_SP2150i	check_for_bytes(obj) calibrate(obj)
SPEX 270M	c_SPEX270M	check_motor(obj)

DAQ equipment objects refer to data acquisition objects such as analog to digital converters, counter cards, multi-channel analyzers, etc. Devices that control data collection and transfer into the computer are DAQ objects. The class diagram for the DAQ parent class, p_DAQ, is shown in Figure 10. The description and available DAQ child classes are summarized in Table 2.

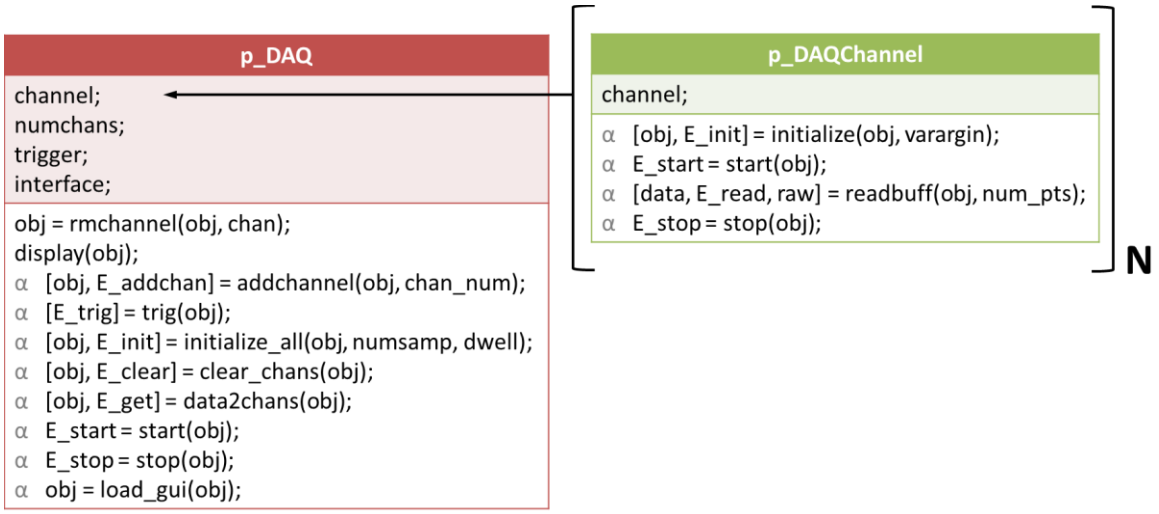

Figure 10: Class layout for the DAQ and Channel objects. Channel objects are housed inside of the DAQ object in the channel property.

Channel equipment component objects refer to the individually addressable inputs and outputs in a data acquisition card. Channel classes can be configured to function as analog input and output, digital input and output, counting. Some DAQ objects can contain various combinations of different kinds of Channels. All of the Channel objects are stored in the channel property of their corresponding DAQ object in an array of variable length represented in Figure 10. The available Channel child classes are listed in Table 3.

On creation of a DAQ object, the channel property is filled with an appropriately-sized array of non-functioning placeholder objects of type c_EmptyChannel (see Table 3). The user then uses the addchannel method to indicate which channels are being used.

This way, unused channels on the DAQ card are still valid Channel objects, but merely non-functioning ones.

Table 2: DAQ class summary.

p_DAQ Object

Property	Type	Description
channel	channel objects	Array of channel objects. By default is filled with c_EmptyChannel objects (See equipment component classes channel type object).
num_chans	double	Array containing the number of channels used and the total number of channels available.
trigger	double	Digital input line number for trigger.
interface	varies	Interface object for DAQ.

Method	Description
addchannel	Adds a Channel object to the specified channel number.
rmchannel	Replaces object in the specified channel with an c_EmptyChannel object.
trig	Sends a digital trigger on the trigger line defined in the trig property.
initialize_all	Initializes all channels that have been added.
clear_chans	Clears the task information from a channel object (Rarely needed).
data2chans	Disseminates collected data to the appropriate channels after collection to aid with data processing. Needed after every stop function execution. This is necessary because data processing occurs in the channel objects.
start	Starts data collection on initialized channels
stop	Stops data collection on initialized channels.
load_gui	Opens the GUI for the DAQ object (if available).
display	Standard display function. Shows GUI (if loaded).

Child DAQ Classes

Instrument	Class	Additional Methods
PCA Multiport Multichannel Analyzer	c_PCAMultiport	acquire getTime set_range
National Instruments PCI-6221 Card	c_PCI6221	none
National Instruments PCI-6320 Card	c_PCI6320	none
National Instruments PCI-6602 Card	c_PCI6602	none
National Instruments USB-6008	c_USB6008	none

Table 3: Channel class summary.

p_DAQChannel Object

Property	Type	Description
channel	string	Description of the type of channel for reference by the DAQ object. Mostly for bookkeeping.

Method	Description
initialize	Initialization procedure for each individual channel object. Handles necessary start up commands that are specific to each type of channel. Run by the initialize_all function in the DAQ object.
start	Starts acquisition in the instance that the type of channel must be started individually. Run by the start function in the DAQ object.
readbuff	Processes the data and returns the result. The most important function in the channel class.
stop	Stops acquisition in the instance that the type of channel must be stopped individually. Run by the stop function in the DAQ object.

Child Channel Classes

Channel Type	Class	Additional Methods
Analog Input Channel	c_AlgInChannel	none
Gated Counter Channel	c_GtdCtrChannel	none
Empty Channel (placeholder)	c_EmptyChannel	none

Stage equipment objects refer to motion controller objects, typically single or multi axis motion stages. In the microscope, these classes control translation of the sample, the beam, objectives, delay lines, etc. The class diagram for the Stage parent class, p_Stage, is shown in Figure 11. The description and Stage child classes are shown in Table 4.

Axis objects are the equipment component objects which address the individual motion axes for a Stage object. Axis objects to the Stage object that contains them are the similar to the Channel objects in the DAQ object. The Stage object handles the communication for all Axis objects it contains, but the Axis object is what is directly addressed by the user. This gives the user the ability to reference Axis objects from multiple controllers into a single experiment easily, enhancing the interchangeability of

different objects. As with the DAQ objects, all of the Axis objects are stored in the channel property of their corresponding Stage as an array of variable length represented in Figure 11. The available Axis child classes are listed in Table 5.

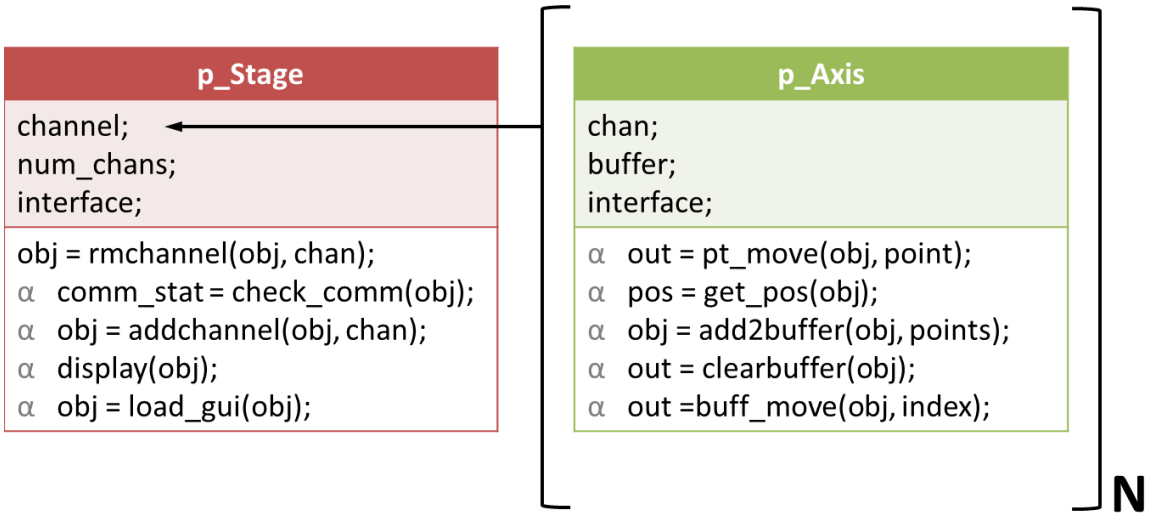

Figure 11: Class layout for the Stage and Axis objects. Axis objects are housed inside of the Stage object in the channel property.

On creation of a Stage object, the channel property is filled with an appropriately-sized array of non-functioning placeholder objects of type c_NullAxis (see Table 5). The user then uses the addchannel method to indicate which channels have a controllable physical component. This way, channels on the motion controller with nothing plugged into them are still valid Axis objects, but merely non-functioning ones.

Table 4: Stage class summary.

p_Stage Object

Property	Type	Description
channel	channel objects	Array of channel objects. By default is filled with c_NullAxis objects (See equipment component classes Axis type object).
num_chans	double	Array containing the number of channels used and the total number of channels available.
interface	varies	Interface object for Stage (typically serial port).

Method	Description
addchannel	Adds an Axis objet to the specified channel number.
rmchannel	Replaces object from specified channel with a c_NullAxis object.
check_comm	Checks the communication with the Stage, returns true if successful and false if not.
initialize_all	Initializes all channels that have been added.
load_gui	Opens the GUI for the Stage object (if available).
display	Standard display function. Shows GUI (if loaded).

Child Stage Classes

Instrument	Class	Additional Methods
Newport ESP-301 Controller	c_NP_ESP301	none
Newport NanoPZ Actuator	c_NP_NanoPZ	none
Queensgate NPS3330 Controller	c_QGNPS3330	send_command read_response
Newport SMC-100 Controller	c_SMC100	none

Table 5: Axis class summary.

p_Axis Object

Property	Type	Description
chan	double	Channel number on the Stage object.
buffer	c_Buffer	Buffer object containing pre-translated commands for use in experiment classes (See "Experiment Component Classes" section).
interface	varies	Interface of Stage object that it is contained in.

Method	Description
add2buffer	Adds an array of position values into the buffer.
clearbuffer	Clears all points from the buffer.
buff_move	Moves to the position in the buffer corresponding to the index provided.
pt_move	Moves to the absolute position indicated by val.
get_pos	Returns the current position.

Child_Stage Classes

Instrument	Class	Additional Methods
Newport ESP Compatible Axis	c_ESP301Axis	reset_home define_home
Newport NanoPZ Axis	c_NanoPZAxis	none
Newport Legacy Axis	c_NPAxis	reset_home get_status get_velocity set_velocity
Empty axis (placeholder)	c_NullAxis	none
Queensgate Axis	c_QGAxis	send_command (axis specific) read_response (axis specific)

2.2.3.3. Data Objects

Data objects are non-physical components that are necessary for the operation of the experiment classes. They are responsible for organizing, analyzing, displaying, and saving data. By defining them as classes, they are grouped with useful properties and the methods that perform operations on them. Actions such as displaying and saving can be customized to include useful information such as scale bars or time stamps.

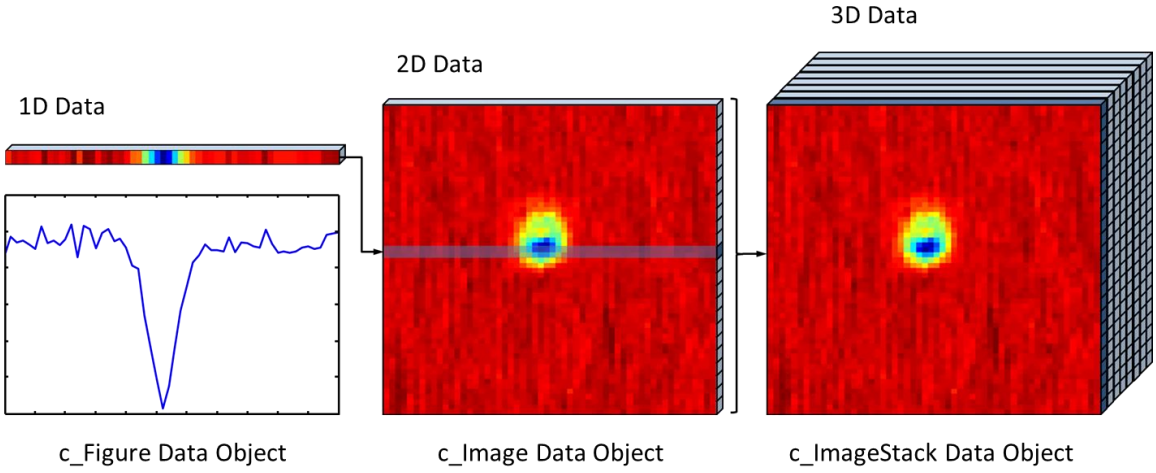

Figure 12: Data types in the IMP software. Depending on the experiment to be conducted the data complexity can continue to grow in the future, which the software would support.

The standard layout of data storage in IMP is shown in Figure 12. Data collected on the microscope is typically presented in either 1-D in the form of plots, or 2-D in the form of images. To cover these forms, two classes have been designed: c_Figure and c_Image. As transient data is becoming more prevalent, a new data type of c_ImageStack is being developed which will handle 3-D data consisting of stacks of multiple images or movies.

All c_Figure objects are used for displaying and working with one-dimensional data collected by changing a single variable and collecting. The c_Image object is used for displaying and working with two-dimensional data collected by changing two variables

and collecting. The class structures for the c_Figure and c_Image classes are shown in Figure 13. The descriptions of the c_Figure and c_Image classes are shown in Table 6.

There is an inheritance relationship between c_Figure and c_Image classes, in that c_Image classes inherit all of the properties and methods of c_Figure classes. However, this relationship exists because a c_Image class is essentially a c_Figure class, but with added properties and methods. This means that the c_Image class also contains all of the properties and methods of the c_Figure class. To save space, they have been left off the class diagram for the c_Image class.

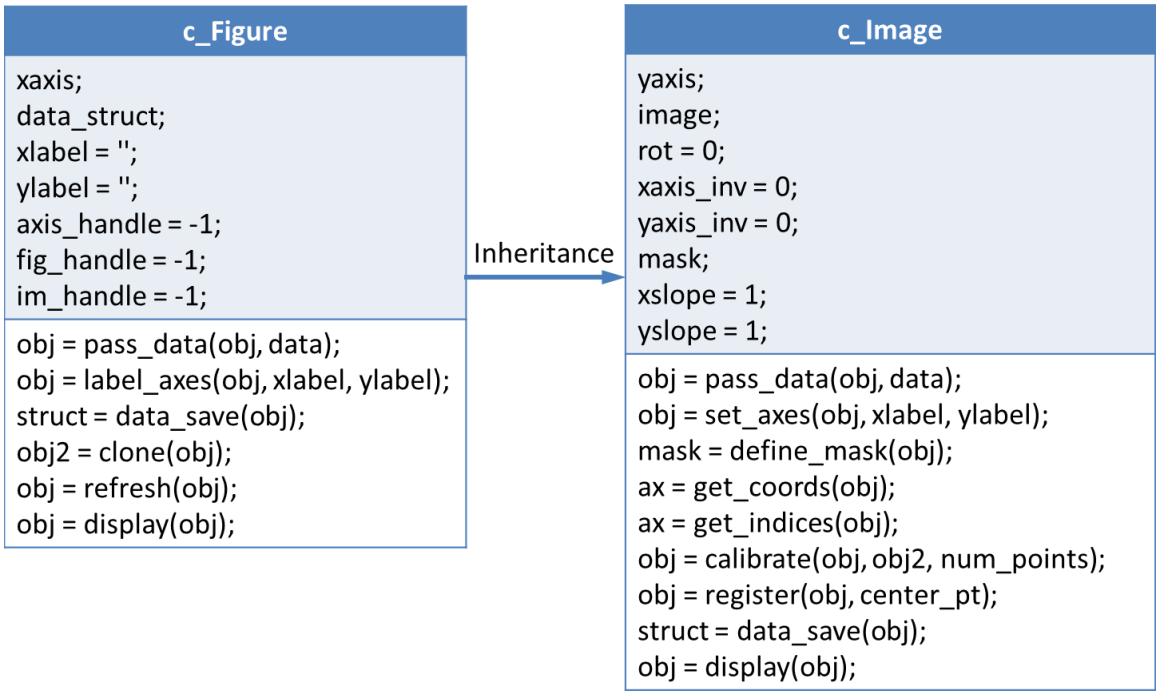

Figure 13: Class layout for the Figure and Image objects. The Image class inherits properties and methods from Figure class.

Table 6: Figure and Image class summary.

c_Figure Object

Property	Type	Description
xaxis	double	Position values for the x-axis.
data_struct	double	Data is stored in this property.
xlabel	string	Label for the x-axis.
ylabel	string	Label for the y-axis.
axis_handle	double	Handle value for the Matlab axis.
fig_handle	double	Handle value for the Matlab figure.
im_handle	double	Handle value for the Matlab image.

Method	Description
pass_data	Places provided data into the data_struct property.
label_axes	Puts a label on the axes of the plot.
data_save	Saves object information to a file.
clone	Creates a non-handle copy of the object.
refresh	Re-plots the data in data_struct
display	Standard display function.

c_Image Object

*Contains all of the properties and methods of a c_Figure object also.

Property	Type	Description
yaxis	double	Position values for the y-axis.
rot	boolean	Switch for 90 degree rotation on display.
xaxis_inv	boolean	Switch for x-axis flip on display.
yaxis_inv	boolean	Switch for y-axis flip on display.
mask	c_Mask object	Mask object for use in Experiment classes.
xslope	double	Multiplier for scaling the x-axis.
yslope	double	Multiplier for scaling the y-axis.

Method	Description
set_axes	Sets the rotation, x-inversion, and y-inversion to correctly display image.
define_mask	Creates a region of interest mask of rectangular or polygonal shape.
get_coords	Returns coordinates of a point selected by double-clicking on the image.
get_indices	Returns indices of a point selected by double-clicking on the image.
register	Coordinate registration by selecting specified number of points on a known image. If the num_points is 0, uses slope given in the image object.

2.2.3.4. Experiment Component Objects

The last set of objects needed for running experiments with the software are the experiment component objects. These are miscellaneous objects that aid in the experimental design, but do not fit into the other categories. They do not have parent classes and their existence enables extra features in experiment objects. As of now, there are only two experiment component objects: c_Buffer and c_Mask. The class structures for the c_Buffer and c_Mask classes are shown in Figure 14, and their descriptions are shown in Table 7 and Table 8, respectively.

c_Buffer
numpoints values commStrArray
obj = add2buffer(obj,varargin) obj = clearbuffer(obj) out = readbuffer(obj)

c_mask
imagemask; indexmask; rot; xaxis_inv; yaxis_inv;

obj = c_Mask(in_size);
obj = set_axes(obj,rot, flip_lr, flip_ud);
obj = custom_mask(obj, new_mask);
obj = add_mask(obj, add_mask);
obj = sub_mask(obj, sub_mask);
obj2 = clone(obj);
obj = clear_mask(obj);
display(obj);

Figure 14: Class layout for the Buffer and Mask experiment component classes.

The c_Buffer object takes in an array of axis position values, translates them into "move" commands to be sent to an Axis object interface, and stores them in the commStrArray property. This is done on the fly in the Axis object's pt_move method, but there is typically an associated overhead in building the command (e.g. checksum calculation). This overhead may be small for a single point, but imaging experiments involve doing this hundreds of thousands of times. Buffer classes eliminate this overhead by storing pre-translated move commands for each possible position. These commands are accessed by the buff_move command in the Axis class definition by imputing the index value of the pre-translated command. Each Axis object contains a c_Buffer object in its buffer property, whether or not it is actually used.

Table 7: Buffer class summary.

c_Buffer Object

Property	Type	Description
numpoints	double	Number of points in Buffer object.
values	double	Position values for the movements.
commStrArray	varies	Translated position movement commands.

Method	Description
add2buffer	Appends buffer to include specified position values.
clearbuffer	Clears buffer values and commStrArray
readbuffer	Translates commStrArray back to position values.

The c_Mask object is an object that modifies the c_Image class for use in image collection. The mask object contains a Boolean array which defines which points on an image should or should not be collected. This greatly reduces image collection time, while keeping the important parts of the image intact. The define_mask command in the Image object is used to draw rectangular or polygonal shapes to define areas to be included.

Table 8: Mask class summary.

c_Mask Object

*Contains all of the properties and methods of a c_Figure object also.

Property	Type	Description
imagemask	boolean	Boolean matrix representing the image.
indexmask	boolean	Boolean matrix representing the image with added dummy pixels.
rot	boolean	Switch for 90 degree rotation on display.
xaxis_inv	boolean	Switch for x-axis flip on display.
yaxis_inv	boolean	Switch for y-axis flip on display.

Method	Description
set_axes	Sets the rotation, x-inversion, and y-inversion to correctly display image.
custom_mask	Replaces the imagemask with the provided matrix and updates indexmask.
add_mask	Adds provided matrix to the existing mask
sub_mask	Subtracts the provided matrix from the existing mask.
clone	Creates a non-handle copy of the mask object.
clear_mask	Clears mask.
display	Standard display function.

2.2.4. Experiment Objects

Experiment objects are the central elements of the software that execute a specific experimental procedure. The purpose of all the aforementioned objects are pieces that come together to make the Experiment objects work. As such, Experiment objects are complex objects which contain and control the other objects in order to perform the desired experiment. These are the objects that a typical experiment designer will have to create if a satisfactory one does not exist.

Like the Framework object, Experiment objects read a configuration file on initial setup. This file contains default values for the properties as well as which equipment objects will be used to conduct the experiment. This way multiple experimental setups can be stored and readily accessible.

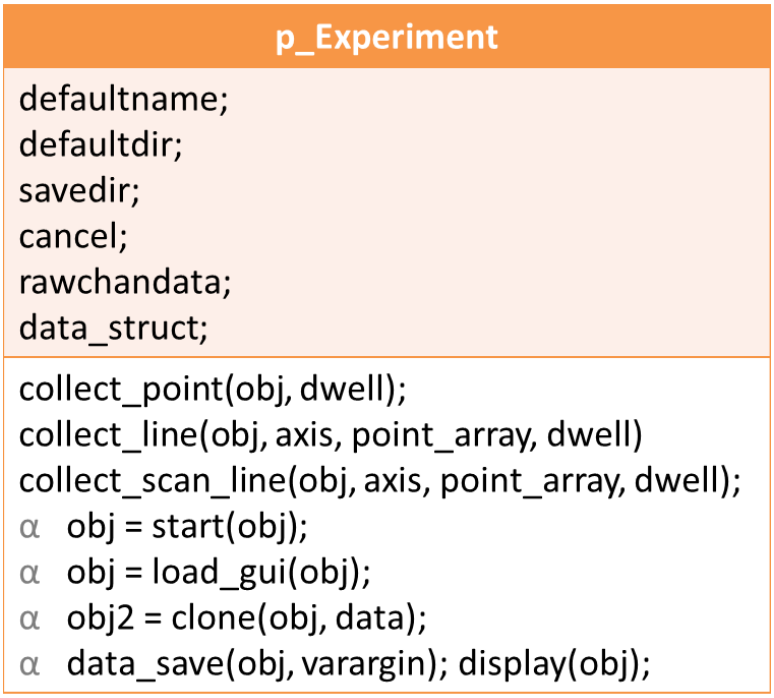

Figure 15: Class layout for the parent Experiment class.

Experiment classes are each very unique, containing drastically different arrays of equipment, data, and support objects. However, experiment objects inherit from a parent class, p_Experiment, which defines methods that should be available for all experiments. The class diagram for the Experiment parent class is shown in Figure 15, and a detailed description is in Table 9.

Table 9: Experiment class summary.

p_Experiment Object

Property	Type	Description
defaultname	string	String containing the name of the default configuration file for the Experiment object.
defaultdir	string	String containing the location of the directory containing the default configuration files.
savedir	string	String containing the directory for saving data into.
cancel	boolean	Switch indicating whether or not the Experiment has been aborted with [CTRL]+z.
rawchandata	double	Raw data is stored in this property.
data_struct	double	Data is stored in this property.

Method	Description
collect_point	Collects a single-point for the specified dwell time and returns it.
collect_line	Collects a line of points at the specified positions and returns their values.
collect_scan_line	Collects a line of points at the specified positions and returns their values.
start	Starts the execution of the experiment.
stop	Stops the experiment.
load_gui	Opens the GUI for the DAQ object (if available).
clone	Creates a non-handle copy of the mask object.
data_save	Saves object information to a file.
display	Standard display function. Shows GUI (if loaded).

Child Experiment Classes

Experiment	Class	Additional Methods
Single-Axis Scanning Experiment	c_1AxisScan_Exp	See section
Two-Axis Imaging Experiment	c_2AxisImage_Exp	See section
Two-Axis Laser Scanning Experiment	c_2AxisLaserScan_Exp	See section
Monochromator Scanning Experiment	c_Monoscan_Exp	See section

2.2.4.1. Methods for Experiment Class Design

When designing Experiment classes, there are three useful methods that are currently written in the p_Experiment class: collect_point, collect_line, and collect_scan_line. These are prewritten methods for data collection that are the basic ways of collecting and processing data. As the software develops further, future experiments may require the development of other methods within the parent experiment class; however, these existing methods are the building blocks for all experiments thus far.

2.2.4.2. The Collect_Point and Collect_Line Methods

The collect_point and collect_line methods in the Experiment classes are buffered data acquisition methods. This means that they use triggers to dictate the beginning and ending of data collection associated with a single point. One trigger signals the beginning of data collection, the program collects for a specific dwell time, and a second trigger signals the end.

The raw data and triggers is then sent to each DAQ Channel object and processed with the read_buff command. In the case of counters (c_GtdCtrChannel objects), the data is read directly from the buffer and the difference in counts gives the number of counts between triggers. In the case of analog inputs (c_AlgInChannel objects), the data between the triggers is averaged and the returned data is the result. These two methods are illustrated in Figure 16.

In the counter type input, each trigger signals the DAQ card to record the current number of counts. In this case the first trigger is sent, the system waits for the defined amount of dwell time, and then the second trigger is sent. This can occur either once, for

single-point acquisition, or multiple times, for line acquisition. The difference between successive counts represents the magnitude of the acquired signal for that point.

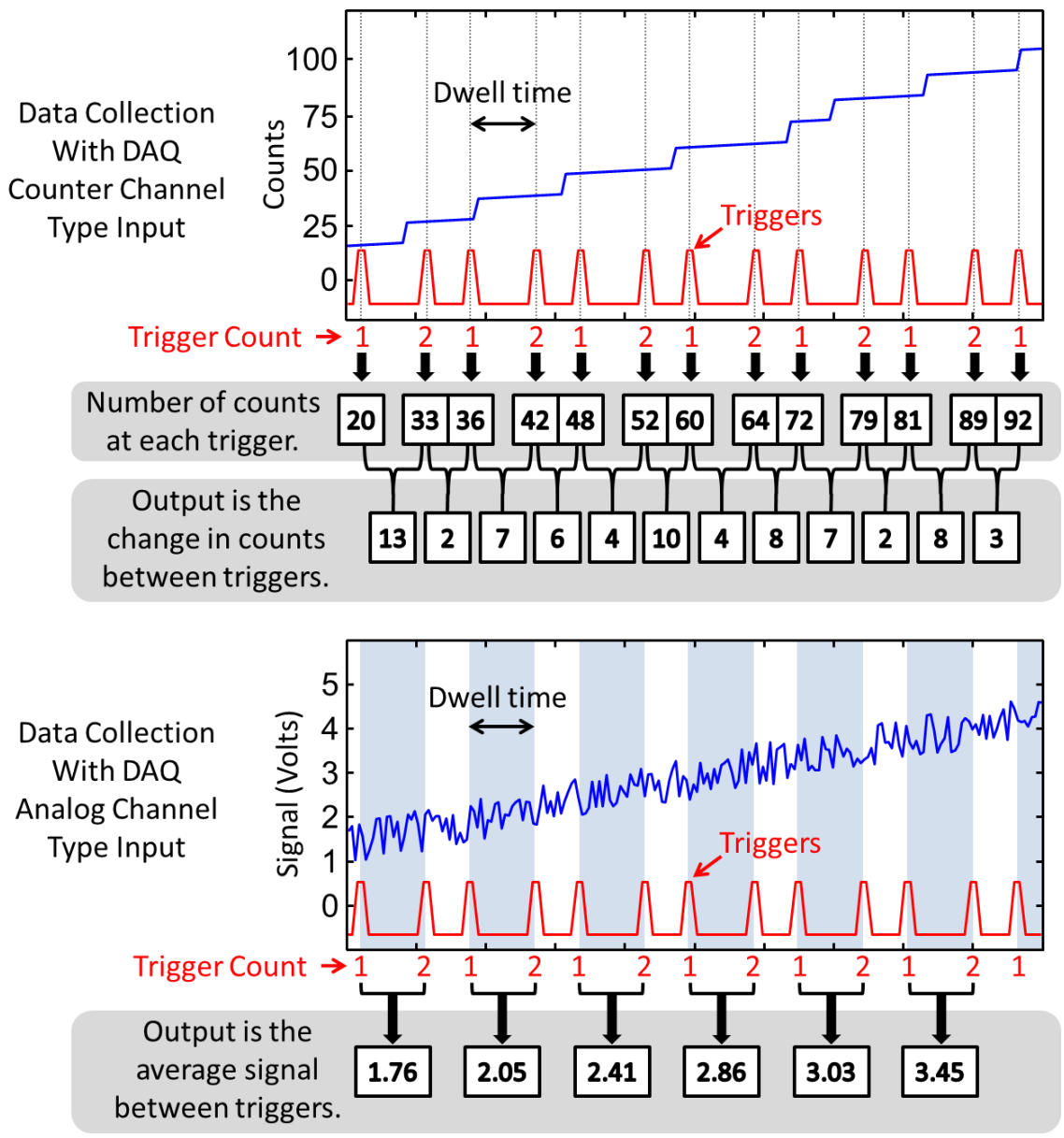

Figure 16: Data processing procedure for a DAQ Channel object configured for counting (TOP) and configured for continuous analog acquisition (BOTTOM). The procedure shown is the same for collect_point and collect_line methods, differing only by the number of points collected.

In the analog type input, data is collected continuously and the triggers are used to mark the beginning and end of the data associated with a single point. The data between

the first and second trigger is averaged to produce the collected value at that point. As with the counter, this can be done once to produce a single point or multiple times for a line.

The difference between the collect_point method and the collect_line method is automation of the motion axis. The collect_point method only requires the experiment class and a dwell time for inputs. It records a single data acquisition point for the specified dwell time and returns the result; a single data point. The collect_line method moves the specified Axis to each buffered index point provided, records for the specified dwell time, and returns the result; an array of data points. The collect_line method is used for raster scanning for imaging and reduces the overhead of processing each point before moving to the next one.

2.2.4.3. The Collect_Scan_Line Method

The collect_line_scan method performs a continuous acquisition while simultaneously recording position values for later use in registration. In this case, the specified Axis object is moved at a speed which satisfies the relationship $dwell\ time = d/v$ for the given positions. While the stage is moving, the instantaneous positions are recorded between two triggers, allowing the software to map the position measurements to the data collected. In this way, the continuously acquired data is binned into the appropriate position and averaged to produce the requested points. This is shown in Figure 17. This method is useful in the case where a motion control axis cannot be accurately sent to multiple points on a line due to speed restrictions or other repeatability issues.

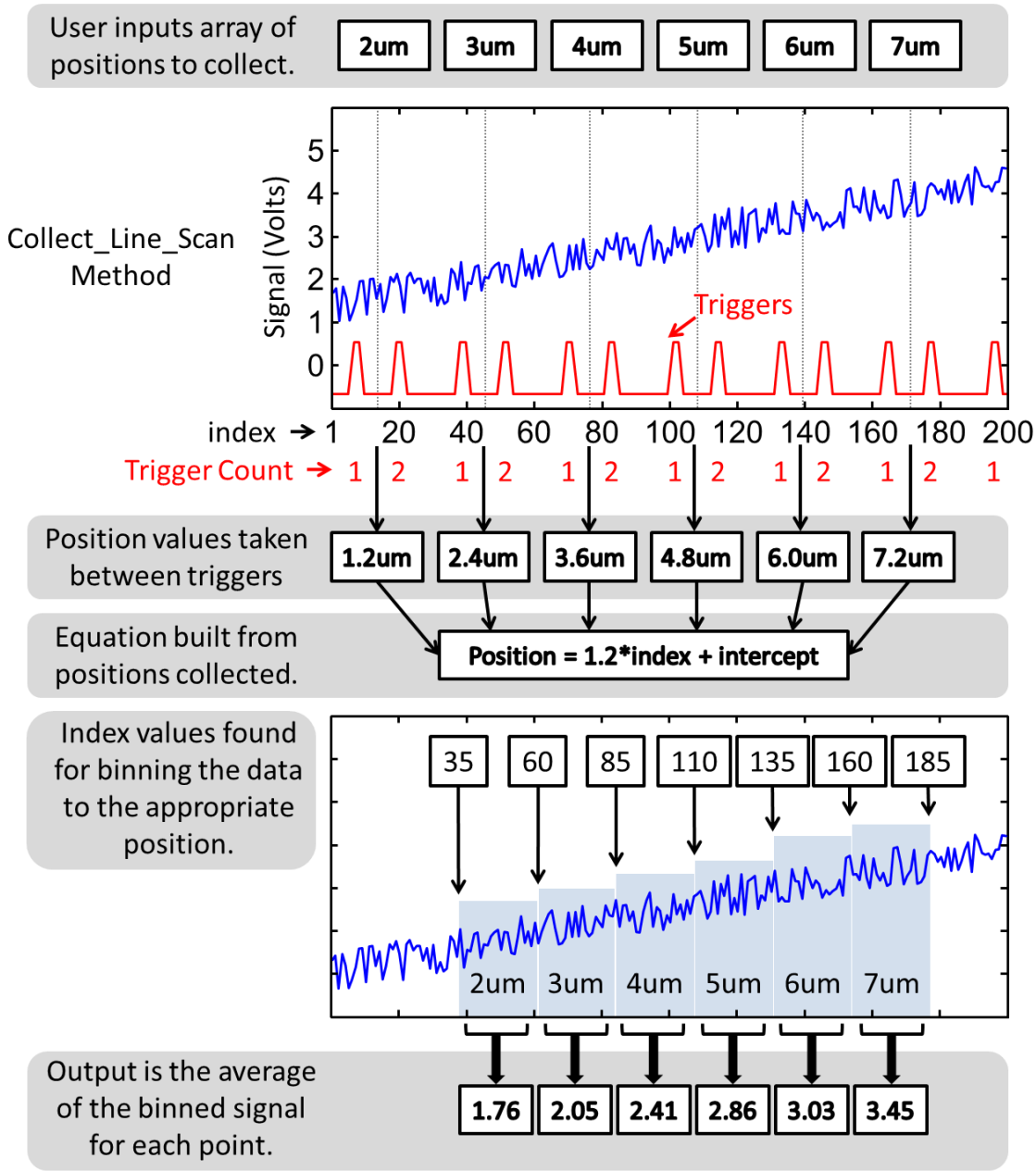

Figure 17: Data processing procedure for the collect_line_scan method. This is a continuous analog data acquisition method, which registers the coordinates of the data after collection has completed.

2.2.4.4. Single-Axis Scanning Experiment

For scans that require observing changes in signal as a result of changing an experimental variable by moving an Axis object, a single-axis scanning experiment can be used. When loaded, the configuration file will load the associated Equipment objects

into their properties. Monochromator, DAQ, and Stage classes are filled with the appropriate equipment objects to be used by the experiment. The axis1 property must contain the Axis object that will be scanned and the channel property must contain the DAQ Channel objects that will be used to collect the data. For each Channel object, a c_Figure object is created in the figure property.

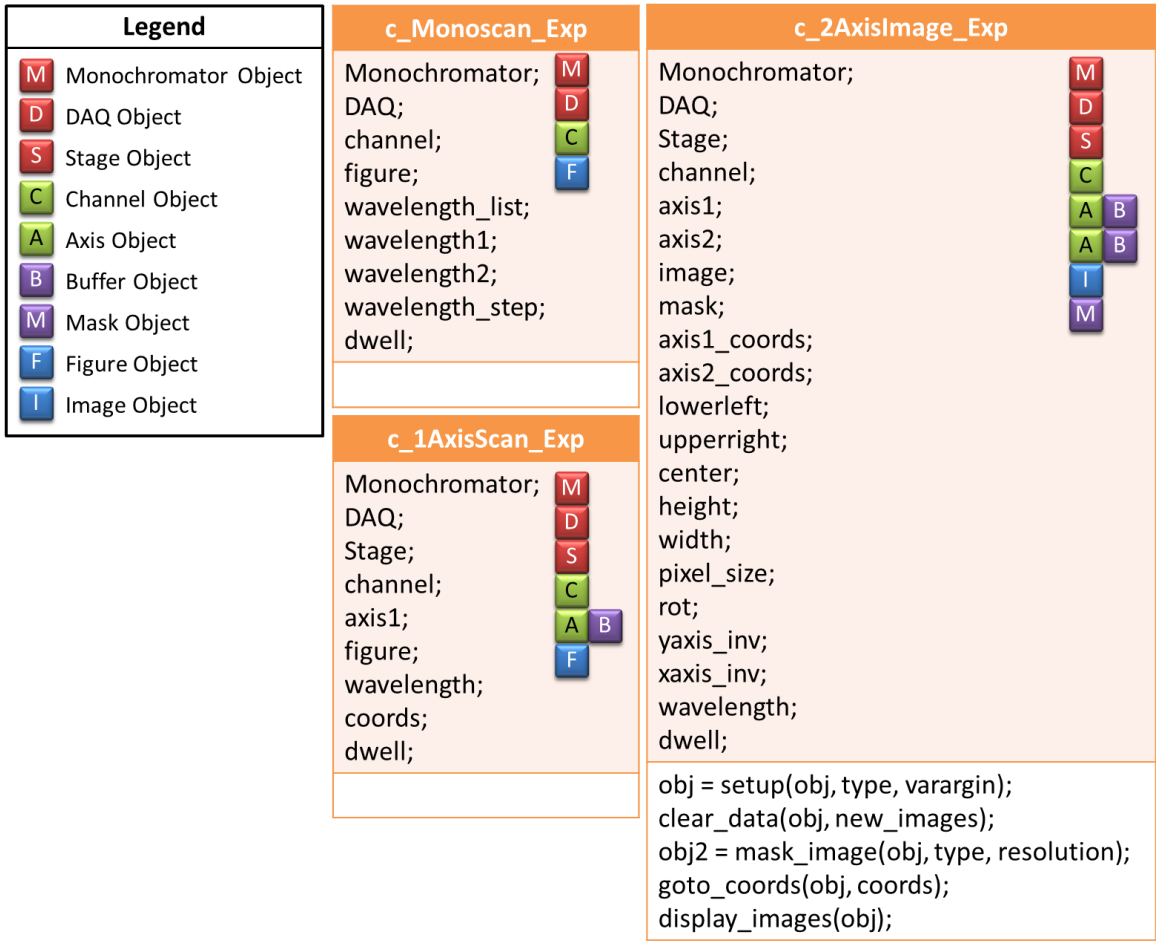

Figure 18: Diagram showing the layout of the most commonly used experiment classes. Also shown are the objects contained in the properties of the experiment classes. The symbols are defined in the legend on the left side.

The remaining properties are set by the user in order to run the experiment as desired. The dwell property is the amount of time to remain in each position, in milliseconds, while collecting data for that position. The coords property contains the array of positions

at which to collect, and the wavelength property contains the wavelength that each Monochromator object should be set to. The class diagram for the c_1AxisScan_Exp is shown in Figure 18.

2.2.4.5. Two-Axis Imaging Experiment

For two-dimensional scanning involving two Axis objects, the c_2AxisImage_Exp class is used; the class diagram is shown in Figure 18. This Experiment object configuration file defines the Monochromator, DAQ, and Stage object to be used, as well as which DAQ Channel objects to use. In this object, axis1 and axis2 need to be defined as the two Axis objects to scan. The object in axis1 will be used as the x-axis in the image, and axis2 will be the y-axis (unless the image is rotated by the rot property).

For each Channel object defined in the configuration file, there will be an Image object created in the property image, and a Mask object will be created and stored in the mask property. The properties: axis1_coords, axis2_coords, pixel_size, rot, xaxis_inv, and yaxis_inv are defined in the configuration file and the Image and Mask objects are created based on their specifications. The properties: lowerleft, upperright, center, height, and width are calculated from these values as well. The remaining properties of wavelength and dwell (in milliseconds) are set by the user, though an initial value is present in the configuration file.

There are five extra methods available to the user for the 2-Axis Imaging Experiment: setup, clear_data, mask_image, goto_coords, and display_images.

2.2.4.6. Monochromator Scanning Experiment

Collecting spectra on the instrument is accomplished with the c_MonoScan_Exp, defined by the class diagram in Figure 18. This Experiment object configuration file

defines the Monochromator, and DAQ object to be used, as well as which DAQ Channel objects to use. For each Channel object in the channel property a c_Figure object is created in the figure property.

The other properties: wavelength1, wavelength2, wavelength_step, and dwell are defined by the user. The wavelength1 and wavelength2 properties define the starting and final wavelengths for the scan, respectively. The wavelength_step property is the step size to take during the scan, and the dwell is the amount of time to spend at each wavelength in milliseconds.

CHAPTER 3. HYBRID STANDING WAVE AND WHISPERING GALLERY MODES IN NEEDLE-SHAPED ZnO RODS: SIMULATION OF EMISSION MICROSCOPY IMAGES USING FINITE DIFFERENCE FREQUENCY DOMAIN METHODS WITH A FOCUSED GAUSSIAN SOURCE

[Reproduced from The Journal of Physical Chemistry C, 117(20), 2013, 10653-60]

3.1. Abstract

Two-photon emission microscopy is used to investigate the photoluminescence properties of individual ZnO rods. The rods are 10-20 μm in length with a tapered cross section that varies from 1-2 μm at the midpoint to several hundred nanometers at the ends. The tapered shape and hexagonal cross section result in complex optical resonator modes that lead to periodic patterns in the two-photon emission image. Finite-difference frequency domain methods using a series of excitation sources, including focused Gaussian, point dipole and plane wave, suggest that resonator modes have both standing wave (Fabry-Pérot) and whispering gallery mode character, whose relative contributions vary along the rod axis.

3.2. Background

Optical resonator modes appear as the dimensions approach the wavelength of light, impacting steady-state spectral properties. The ability to manipulate the structure of ZnO makes it an ideal material for shape dependent optical studies, and through a variety of facile synthetic methods many different forms have been produced, including nanorods with differing end morphologies, tetrapods, and nanohelices[(6-8)]. The simplest cavity resonances are longitudinal, standing-wave modes propagating along the long axis of

ZnO nanorods, which have been described by several groups[9-11]. The size of the resonator determines the optical frequencies that are supported, which are often observed spectroscopically as a series of narrow resonances superimposed on the broader band-edge and trap emission bands[12-19].

While longitudinal modes are clearly important to our understanding of the light-matter interactions of these structures, this work focuses on the cavity-modes supported within the hexagonal cross-section and lie transverse to the rod axis. The faceted crystalline structures of these ZnO materials give rise to a rich variety of optical cavity modes. Previous reports describe these modes using two classic resonator pictures: Fabry-Pérot (FP) modes supported between two opposing parallel facets, and whispering gallery (WG) modes arising from the circulation of light around the periphery of rod through total internal reflection at each crystal face[13, 15-22].

We observed both types of resonances in second-harmonic and two-photon emission images obtained from tapered ZnO rods[23-27]. The rods are 10-20 μm in length and have faceted hexagonal cross-sections with diameters that range from 1-3 μm at their widest point, down to 100-200 nm at the ends. Because the resonance conditions for both modes depend upon the diameter of the structure, and because of the tapered shape, a fixed excitation wavelength will go in and out of resonance as the source moves along the rod and the resonator diameter changes, resulting in a periodic intensity modulation along the long axis of the rod. This paper shows that while the classic FP and WG resonator models[15-19, 22, 28] reproduce the image features in a qualitative sense, finite-difference frequency-domain (FDFD) simulations indicate that the classical resonator models are overly simplistic. In this size regime (200-1000 nm diameter), the hexagonal resonator

modes actually contain characteristics of both the FP and WG resonances, whose relative contributions vary with resonator size. At smaller sizes, the modes have primarily standing-wave character with much of the optical intensity located in the core of the structure. As the size is increased, the intensity distribution shifts to the periphery of the structure, becoming more WG-like in character. These two different mode types may explain the spatial variation in electron-hole recombination that are observed these structures. Pump-probe microscopy experiments from our lab[25, 26] indicate that recombination in the tips of the rod proceeds through an electron-hole plasma state, suggesting that carriers are created in a bulk-like region of the rod, i.e. the core. In the larger sections of the rod, electron-hole recombination is trap mediated, consistent with carriers being produced in the depletion zone near the surface and undergoing rapid charge separation.

3.3. Experimental

ZnO rods were grown using hydrothermal methods adapted from previously published work[29, 30]. An aqueous solution of $Zn(NO_3)_2$ (50 mM) and hexamethylenetetramine ($(CH_2)_6N_4$) (50 mM) was heated in a closed bomb to yield needle-shaped rods ranging from 5 to 30 μm in length and 0.3 to 2 μm in diameter. Size control was achieved by varying reaction temperature, time, and/or concentration. After cooling the reaction to room temperature, the structures were harvested and suspended in ethanol using ultrasonication to break up aggregates. Microscopy samples were prepared by dropcasting a 250 μL of the suspension onto a microscope slide with an etched reference grid. The grid facilitated the locating of the rod observed in the optical microscope in a scanning electron microscope for structural characterization. The ability

to perform both optical and electron microscopy on the same structure allows photophysical observations to be correlated with detailed structural information.

Two-photon emission imaging was accomplished by combining an ultrafast laser source with a home-built far-field optical microscope (Figure 19A). The femtosecond laser source consisted of a mode-locked Ti:Sapphire laser (730 nm, 80 fs, 80 MHz) pumped by a solid-state diode-pumped Nd:YVO_4 laser. The laser output was directed onto the back aperture of a 50x microscope objective (0.8 NA), which focused it to a diffraction limited spot, resulting in two-photon excitation at a localized region of the ZnO rod. Light emanating from the structure was collected by the objective, passed through a dichroic beam-splitter, and focused onto the slit of a monochromator and photomultiplier tube (PMT). Emission images were collected by raster scanning the sample across the focal point of the objective with a piezoelectric nano-positioning stage while monitoring the intensity of the emitted light. Imaging was performed without a coverslip under ambient conditions.

The spatial resolution of the microscope is determined by the size of the laser spot at the focus of the objective. Since two-photon absorption scales with the square of the optical intensity, efficient excitation occurs only at the focus, resulting in confocal-like behavior and a lateral excitation dimension that is smaller than the diffraction limit[31]. Emission images of a 100 nm quantum dots (Figure 19B) indicate that the spatial extent of excitation is 410 nm for the 810 nm excitation, which is slightly larger than the theoretical limits of 380 nm for this wavelength[31]. The spatial extent for 730 nm excitation is slightly less, about 380 nm.

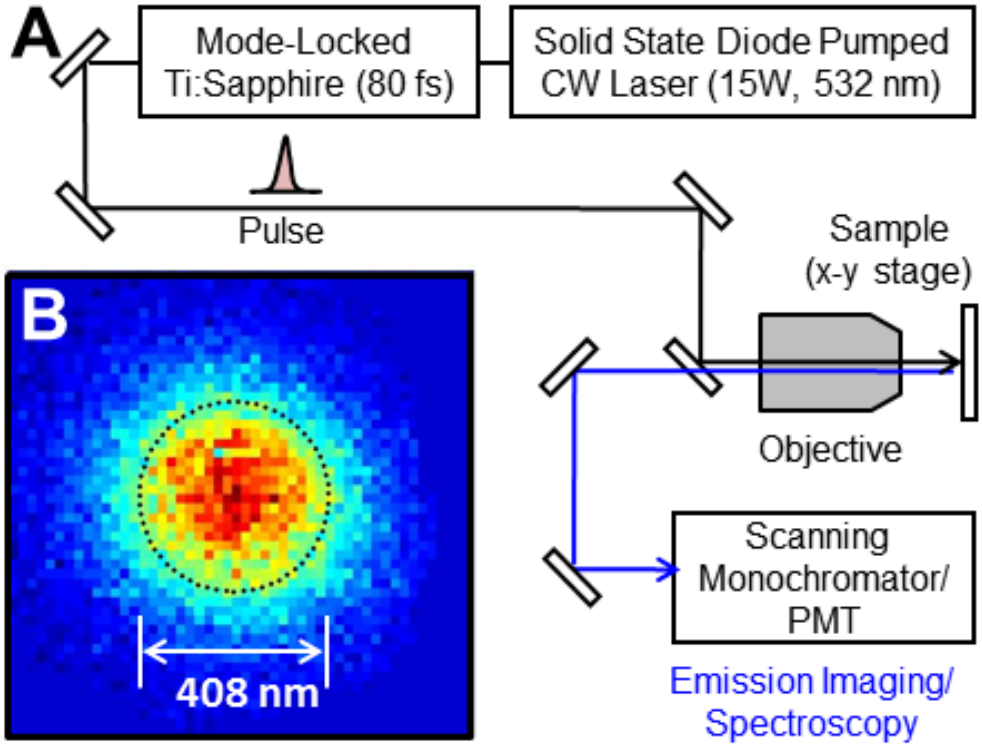

Figure 19: (A) Diagram of the two-photon emission microscope. The 730 nm output of a mode-locked Ti:Sapphire laser is directed onto the back aperture of the microscope objective (50x, 0.8 NA) and focused to a diffraction-limited spot at the sample. Imaging is achieved by raster scanning the sample stage across the focused laser spot and monitoring the emission collected by the objective with a scanning monochromator/PMT. (B) Two-photon emission image of a 100 nm quantum dot with 810 nm excitation. The size of the emission feature suggests that the lateral resolution at this wavelength is approximately 410nm.

3.4. Results And Discussion

Characterization of the optical modes combines two-photon emission imaging with detailed structural information garnered from scanning electron microscopy (SEM). The SEM image of a typical needle-shaped structure is shown in Figure 20A. The rod has an overall length of 17 μm and the hexagonal cross-section diameter (distance between parallel facets, d) that increases from 150 nm at the end to about 1 μm at the midpoint.

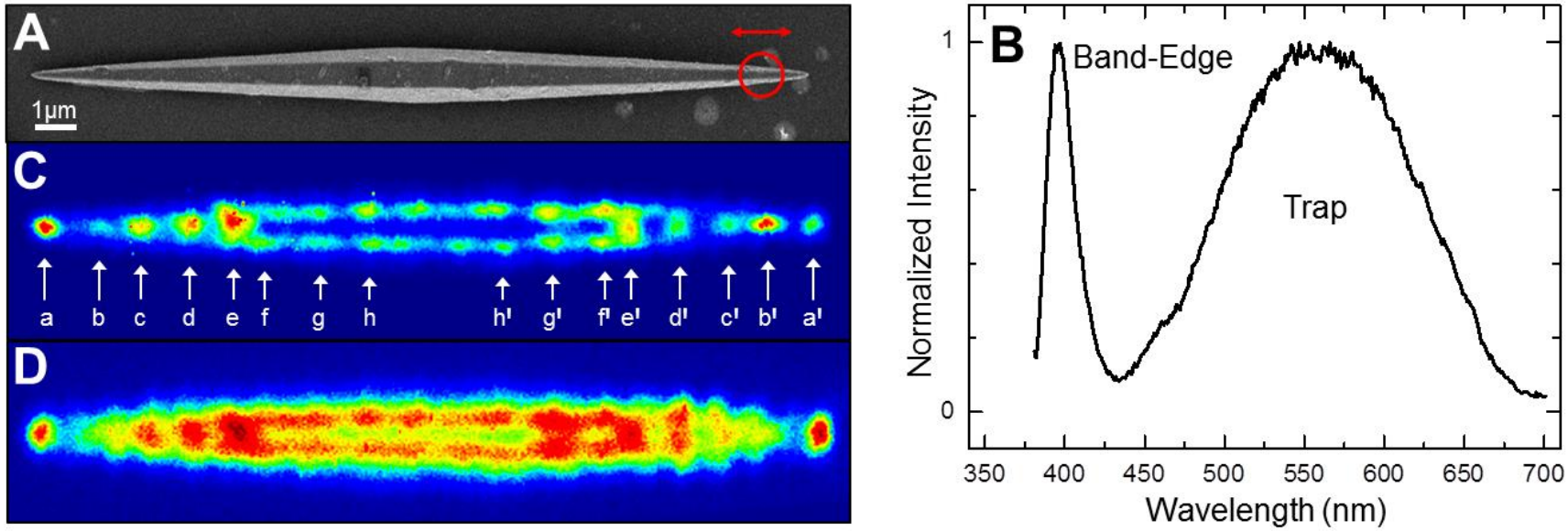

Figure 20: (A) SEM image and (B) emission spectrum of a tapered zinc oxide nanorod. The red circle and double-headed arrow indicate the location at which the spectrum was acquired and the direction of the excitation polarization vector, respectively. (C-D) Photoluminescence images taken at 390 nm and 550 nm, respectively, show a modulated emission pattern along the structure. The lower case letters in (C) indicate the resonance spots discussed in the text.

An individual structure is excited by a focused near infrared laser pulse polarized parallel to the long-axis of the rod, resulting in a two-photon absorption that promotes carriers from the valence band to the conduction band in a localized region of the structure. Because ZnO is transparent in the near infrared, two-photon absorption will occur throughout the excitation volume. Single UV photon absorption at 365 nm, by comparison, would occur within 100 nm of the surface. Free carriers produced by photoexcitation will either relax into excitons, resulting in the intense near-UV emission, or become trapped in defect sites, giving rise to the broad visible emission (Figure 20B).

Emission imaging is achieved by monitoring the photoluminescence intensity at a particular wavelength as a function of two-photon excitation position. Previous work in our lab showed that the majority of the emission detected emanates from the location of laser excitation, indicating that while coupling of light (either the excitation or emission) into wave-guiding modes propagating along the long axis of the rod does occur, it is relatively weak and contributes little to the observed emission at a given point[27]. A striking feature of images compiled from either band edge emission (λ_{em} = 390 nm) or trap emission (λ_{em} = 560 nm) is the axially symmetric intensity modulation along the length of the rod (Figure 20C-D). The emission spots appear along the middle of the rod at smaller diameters (labeled a-c and a'-c' in Figure 20C), becoming two separate spots at larger diameters (f-h and f'-h'). We have observed similar patterns in both second-harmonic and two-photon emission images of other needle-shaped rods[23, 24], and reports of spatially periodic patterns in cathodoluminescence images of tapered wires have been shown previously[13, 15]. Qualitatively, the patterns arise from optical resonator modes associated with a hexagonal cavity formed by the cross-section of the rod. Because of the

tapered structure, the cavity size changes along the long axis of the rod, causing the excitation wavelength to go in and out of resonance as the focused laser spot is moved along the rod. While in principle either the excitation or the emission wavelength could be resonant with the cavity, the qualitative similarity between the two images suggests that the excitation wavelength is largely responsible for the observed patterns.

3.5. Standing-Wave and Whispering Gallery Mode Descriptions

Generally, there are two types of optical modes: standing wave (Fabry-Perot, FP) resonances that are supported between two parallel facets, and whispering gallery (WG) modes that correspond to propagation of light around the periphery of the hexagonal cross-section through total internal reflection off each facet. Both are characterized by resonance conditions that depend upon the resonator size and wavelength, i.e.

$$d_{FP}^{m} = \frac{\lambda}{2n} m \tag{1a}$$

$$d_{WG}^{m} = \frac{\lambda}{3n}\left(m + \frac{6}{\pi} \tan^{-1}\left(\beta\sqrt{3n^2 - 4} \right) \right) \tag{1b}$$

where d_{FP}^{m} and d_{WG}^{m} are the facet separations for the mth mode in the FP and WG resonances, respectively, λ is the wavelength and n is the index of refraction. The value of β is based on the polarization of the excitation source, being $\beta = n$ for TM ($E \| c$) and $\beta = n^{-1}$ for TE ($E \perp c$).

The distance between resonance spots in the emission images, ΔL, depends upon the taper angle of the structure, with smaller cone angles giving rise to larger separations, i.e.

$$\Delta L = \frac{\Delta d}{\alpha} \tag{2}$$

where Δd is the mode spacing, i.e. (d^{m+1}-d^{m}), and α is the change in facet spacing per unit length along the structure.

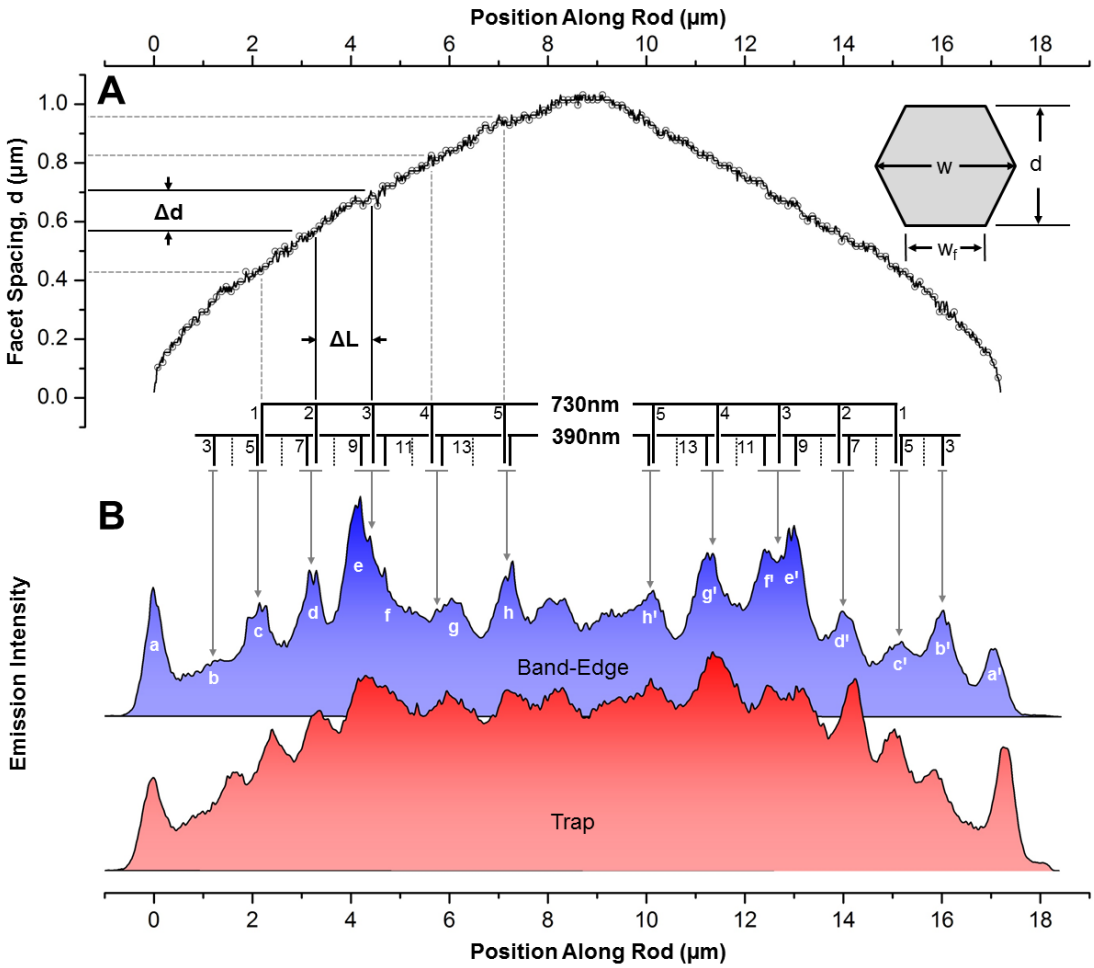

Figure 21: (A) Facet spacing determined from the SEM image in Figure 20A plotted as a function of position along the rod. (B) Intensity profiles obtained by integrating a column of pixels at each longitudinal position along the images for both the band-edge and trap emission images (Figure 20C and Figure 20D). The calculated whispering gallery mode locations for 730 nm and 390 nm light are indicted by the two brackets positioned between (A) and (B). The lower-case letters in the band-edge profile correspond to the resonance spots indicated in Figure 20B.

The value of α varies from one rod to the next, but its value for a particular rod can be estimated from the SEM image. Moreover, for this rod, the overall width (w) is twice the facet width (w_f) over most of the length, indicating that the cross section is nearly a perfect hexagon (Figure 21, inset). The facet spacing (d) is determined from *w* using

$d = \left(\sqrt{3}/2\right)w$, and is depicted as a function of position along the rod in Figure 21A. The α-values extracted from the slopes on the right and left side are 101 nm/μm and 103 nm/μm, respectively, indicating that the rod is nearly symmetric with a consistent taper throughout the much of the structure.

The predicted spacing between resonance spots along the rod are $\Delta L_{FP}=\lambda/2n\alpha$ and $\Delta L_{WG}=\lambda/3n\alpha$ for the two different optical mode types. Using an average α-value of 102 nm/μm, and n=2 for the index of refraction of ZnO at 730 nm[32] leads to predicted separations of ΔL_{FP} = 1.8 μm and ΔL_{WG} =1.2 μm.

Intensity profiles along the long axis for the band-edge and trap emission images (Figure 21B) show the resonances to be nearly equally spaced with an average ΔL of 1.0-1.2 μm. This spacing is qualitatively consistent with the WG mode description and significantly smaller than the spacing predicted by the FP resonance condition. The locations of the WG resonances for the first five modes (λ=730 nm), indicated by the bracket placed above the emission profile, coincide with the locations of the emission maxima.

If the modulated emission intensities were due solely to cavity resonance involving the excitation light, then the patterns observed in the band-edge and trap emission images should be the same. This is not the case. While the modulated pattern is present in both, the band-edge image exhibits a higher contrast compared to the trap, suggesting that the intensity pattern is influenced, to some degree, by the emission. We estimate that in this structure the resonance spacing, ΔL, for 390 nm light (n=2.33)[32] would be 0.54 μm. This is approximately half the spacing for the 730 nm resonances, leading to a possible double-resonance scenario in which the 730 nm modes coincide with every other 390 nm

mode (see 390 nm bracket, Figure 21). Amplified spontaneous emission, and even lasing, of the band-edge photoluminescence has been observed in ZnO nanostructures. While we do not observe evidence of actual lasing, previous work in our lab[23] showed that the band-edge emission has a greater than quadratic power dependence on pulse intensity. This is particularly true when the rod is excited at one of the resonance spots,[23] suggesting that the emission is likely reinforced by the cavity modes as the 390 nm emitted light is reflected off the facets and returns to the excitation region. The trap emission, on the other hand, shows simple quadratic dependence. The larger scaling factor for the band-edge emission effectively results in a higher spatial resolution, accounting for the greater contrast difference between the band-edge and trap emission images.

These WG mode description qualitatively account for many of the features observed in the emission images, but it does not explain, the existence of the spots at the ends of the rod (denoted a and a'). At this point d = 160 nm. This is far below the 450 nm predicted by the WG resonance condition (Eqn 1b) for the m=1 resonance with λ=730 nm, and also smaller than the 210 nm spacing obtained with λ=390 nm. Interestingly, it is close to the spacing calculated using the FP resonance condition (Eqn 1a) for the m=1 mode at 730 nm, underscoring the idea that neither picture adequately describes the resonance properties of these structures.

3.5.1. Finite Difference Frequency Domain (FDFD) Simulations

We have used finite element methods to map the optical intensity distribution created in the rod upon photoexcitation. We treat the 3D tapered rod as a stack of hexagonal resonators of different diameters, enabling the overall structure to be modeled using a

series of two-dimensional calculations. The 2D model of each individual resonator (see Figure 22A, for example) consists of a square box (air) with a hexagonal slab (ZnO) placed at the center. The box is surrounded by a perfectly matched layer (PML) that eliminates electromagnetic reflections at simulation boundaries. The mesh spacing used in the simulations, defined as the size of the largest cell, was 30 nm, which is approximately 10 times smaller than the wavelength inside the ZnO material. Simulations performed with a smaller mesh size (15nm) yielded identical results, confirming the appropriateness of this choice. FDFD methods, which were implemented using the COMSOL Multiphysics software package (version 4.3), solve for the electromagnetic field in response to a single-frequency source, resulting in a steady-state map of the optical intensity distribution inside the resonator. We have examined four different sources: (i) point-source, (ii) line source, (iii) focused Gaussian beam, and (iv) plane-wave. The first two provide a crude approximation of the localized laser excitation; the third is realistic representation of the focused laser beam used in the experiment, while the last provides a comparison with far-field excitation configurations. In each case, the source is polarized with the electric field perpendicular to the simulation plane and the output of the simulation is the EM field inside the simulation area.

(i) Point Source: The simplest localized excitation scheme is an oscillating (ν = 411 THz, λ = 730 nm) current density point source positioned 25 nm above the center of the topmost facet. Figure 22B shows the average optical intensity inside the resonator (i.e. $\langle I \rangle = \int |E|^2 dA / A_{hex}$) as a function of its size. The plot shows a series of sharp resonances for the larger cavity sizes that become increasingly broad for the smaller diameters. The intensity distribution inside the hexagonal cavity is depicted for four of

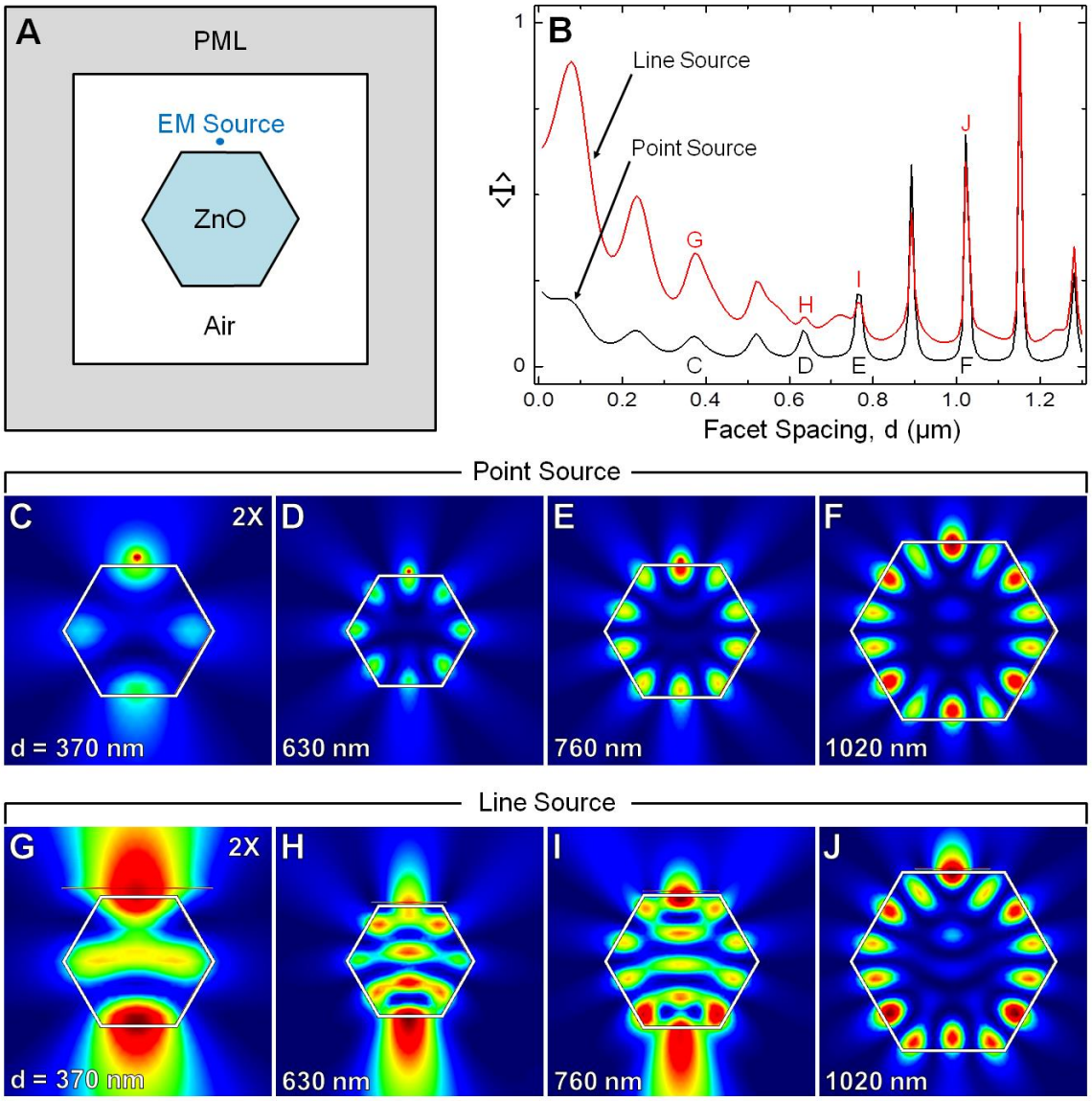

Figure 22: (A) Diagram of the simulation environment depicting the point source configuration. The line source (not shown) is placed in the same location and is 440 nm wide. (B) Plot of the average intensity $\left(\langle I\rangle = \int |E|^2 dA\,/A_{hex}\right)$ as a function of the facet spacing (d) for both the point source (black) and line source (red). (C-J) Spatial intensity maps $(|E|^2)$ for resonators with facet spacing d = 370 nm, 630 nm, 760 nm and 1020 nm for the point source (C-F) and line source (G-J). Blue corresponds to zero intensity, red is max intensity.

the resonances in Figure 22C-F. The largest resonators show the characteristic WG mode pattern in which the optical field is located near the periphery of the structure. The width of the resonances reflects the quality of the cavity. For the larger sizes, total internal

reflection at each facet minimizes loss, resulting in multiple round trips and narrow resonances. The broadening of the resonances as the cavity size decreases suggests an increased loss per round trip. This most likely occurs at the vertices, which become a dominant feature at the smaller sizes.

The spacing between modes is not constant across this size range. The Δd spacing between the sharp peaks at larger cavity size is 130 nm, similar to that predicted by the WG mode resonance condition (Eq 1b). Interestingly, for the broader resonances, at smaller cavity sizes, Δd is about 160 nm, which matches the FP spacing (Eq. 1a) Although the presence of standing-wave character is not obvious from the mode patterns, the EM sources described below suggest that the modes best described as hybrid resonance with both WG and FP character.

(ii) Line Source: While the point source is qualitatively appealing, it is not a good representation of the experimental configuration, where the spatial extent of excitation is several hundred nanometers. A similar calculation in which the point source is replaced by a line 400 nm long and centered at 25 nm above the top facet addresses this shortcoming. The results from this simulation, which are shown alongside those for the point source in Figure 22, highlight the role that the source plays in shaping the field patterns.

A key factor appears to be the size of the source in relation to that of the resonator. The resonances for the larger cavity sizes are unaffected by the increase in the size of the source. They have similar magnitude, width, and are located at the same diameters (Figure 22B). Furthermore, the field distributions (Figure 22J) are nearly identical to those obtained from the point source, with a small, but notable difference being a slight

increase in the intensity present in the center of the resonator. While the results for the larger diameter are unaffected by the change in source, there are significant differences at smaller sizes (d < 600 nm). First, the broad resonances at smaller diameters have drastically higher average intensities in the line source model than the point source (Figure 22B). Moreover, the field distributions are also affected. Whereas the point source produces a mode pattern in the 370 nm resonator that is largely WG in nature, the patterns obtained with the line source takes on more standing-wave character (Figure 22G). As the cavity size increases (630 nm and 760 nm), the modes are neither completely WG nor FP like in character (Figure 22H-I), but rather a combination of the two. The simulations point to the presence of two modes progressions, where at large cavity sizes the resonances are dominated by WG modes, and at small cavity sizes they are dominated by FP character. Hybrid resonances that contain elements of both are observed where the two progressions overlap, which appears to occur when the source and top facet are of similar sizes. These results underscore the need for adequately modeling the EM source in simulating the emission patterns of these structures.

(iii) Gaussian Source: An optical source that mimics the focused Gaussian beam used in the experiment is implemented by specifying the EM field along the boundary, i.e.

$$E(x) = E_0 \frac{\omega_0}{\omega(y_B)} \exp\left(\frac{-x^2}{\omega^2(y_B)} - ik\frac{x^2}{2R(y_B)} + i\zeta(y_B)\right) \quad (3)$$

where y_B is the distance from beam waist to the boundary, x is the coordinate along the boundary, and k is the wave vector for the propagating electric field (Figure 23A). The

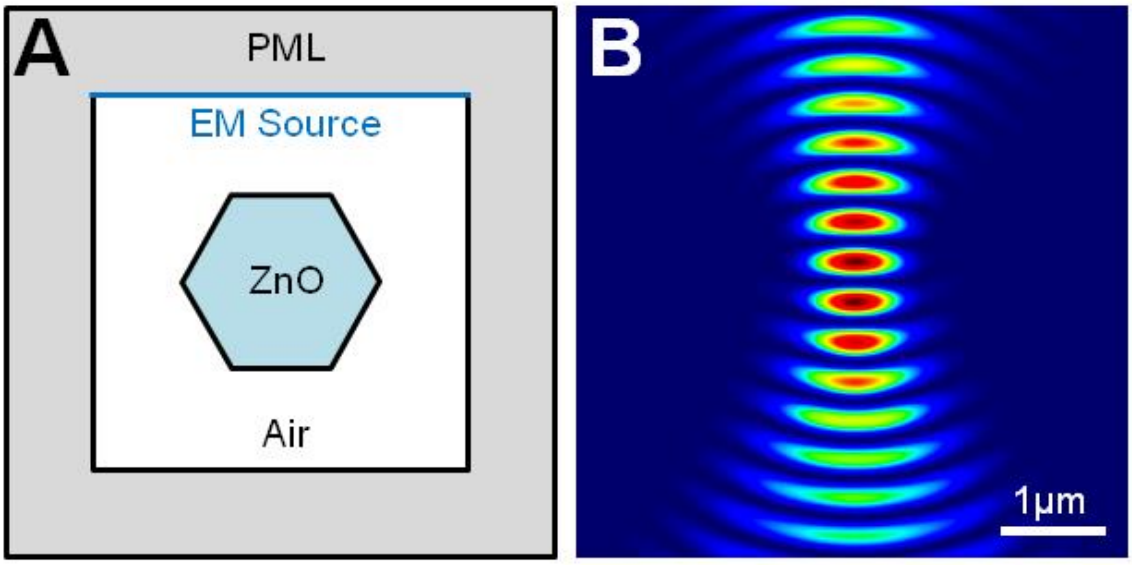

Figure 23: (A) Diagram of the focused Gaussian simulation environment. The EM source is functionalized according to Eq 3 with the x and y dimensions corresponding to the horizontal and vertical axes and the origin located at the center of the simulation box. (B) Spatial map of the optical field $(\boldsymbol{Re}(|\boldsymbol{E}|))^2$ produced by the Gaussian source in the absence of the resonator.

radius of the beam waist at the focus, ω_0, is defined at the 1/e width of the electric field. The functions $\omega(y_B) = \omega_0(1 + (y_B/y_R))^{1/2}$, $R(y_B) = y_B[1 + (y_R/y_B)^2\ ]$, and $\zeta(y_B) = \arctan(y_B/y_R)$ are the beam width, radius of curvature, and Gouy phase at the boundary, respectively, and $y_R = \pi\omega_0^2/\lambda$. With this boundary condition, the EM field focuses to a minimum spot size at the center of the simulation box (y = 0). An intensity map of the optical field, $(Re(|E|))^2$, produced by this Gaussian source, in the absence of the hexagonal resonator, is shown in Figure 23B. With $\omega_0 = 460nm$, the lateral width of the two-photon volume created by the source, obtained by examining $I^2 = (|E|^2)^2$, is around 420 nm, which is comparable to the lateral resolution of two-photon excitation in our microscope.

The top of Figure 24 shows a simulated two-photon emission image obtained using this focused Gaussian source. The image was reconstructed using a procedure analogous

to the experimental image collection. First, the cross-sectional diameter is determined at a particular position along the rod from the SEM image. For a given resonator size, a series of simulations are performed at different displacements between the central axis of the EM source and the midpoint of the resonator. For each configuration, the squared-intensity, i.e. $(|E|^2)^2$, is integrated inside the resonator to represent the total two-photon excitation; this series of integrated intensities is then represented by a column of pixels in the simulated image. The process is repeated for a series of resonator sizes to construct the two-dimensional image.

The simulated image is a reasonable mimic of the two-photon emission image, reproducing many of its qualitative features, including the appearance of off-centered spots at larger diameters that become single, centered spots near the ends of the rod. The mode patterns that correspond to resonance spots reveal two distinct progressions. When excited at the center, the smaller resonators near the tips of the rod show hybrid patterns with more FP than WG mode character (Figure 24A-D), while significant WG character is observed in the mode pattern when excited off-center (Figure 24E-H), especially at the larger diameters. The simulated image also shows the existence of modes at facet spacing values below the lowest predicted WG mode resonance for either 390 nm or 730 nm light (for 390 nm, $d_{WGM}^{1} = 210nm$) and predicts the intense spot at the tip of the rod.

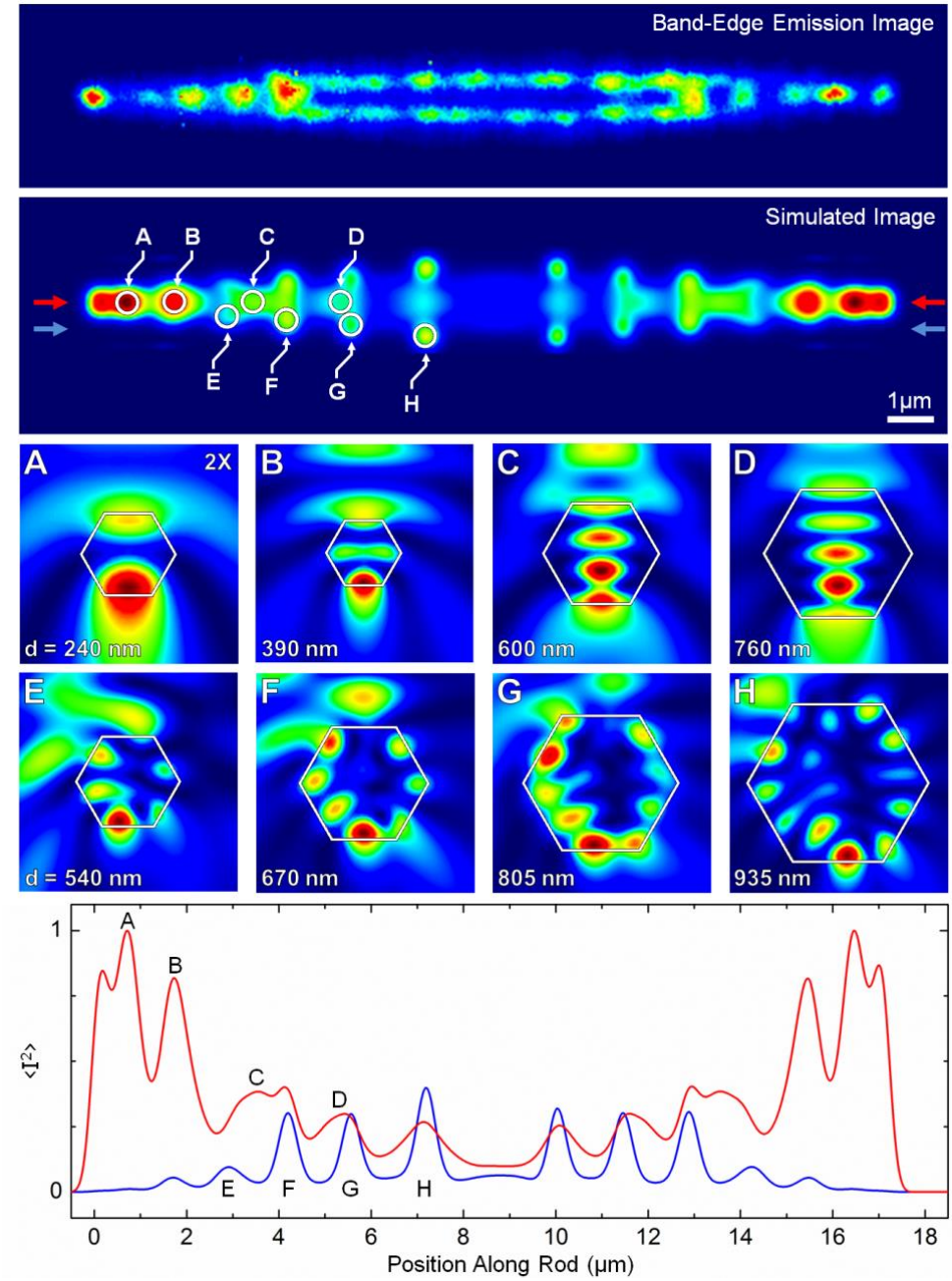

Figure 24: (TOP) Simulated emission image constructed from a series of calculations on resonators with sizes corresponding to width measurements taken from the SEM image (horizontal dimension). A series of calculations are performed for each resonator size in which the center of the Gaussian source is offset relative to the center of the resonator in the horizontal dimension. For each simulation, the average squared intensity $\left(\langle I^2\rangle = \int |E|^4 dA\,/A_{hex}\right)$ inside the resonator is calculated and its value is displayed as pixel in the image, with blue colors corresponding to zero intensity; red is maximum intensity. (A-H) Spatial intensity maps $(|E|^2)$ of the corresponding encircled modes from the image. (BOTTOM) Plot of average squared intensity per unit area for a slice through the center (red) and 500 nm from the center (blue).

Slices of the image taken down the center (red, dashed) and at 500 nm off-center (blue, dashed) are plotted as a function of position at the bottom of Figure 24. The intensity of the centered modes decreases with increasing the diameter, while the intensity of the off-centered modes follows the opposite trend.

(iv) Plane-wave Source: The dependence of the field patterns on source geometry raises the question: Is the spatial variation observed with the focused source also present when the structure is excited by a monochromatic plane-wave? We addressed this question by replacing the focused Gaussian beam with a plane wave source (Figure 25). Although the details differ, many of the features observed with the Gaussian source are preserved with plane wave excitation (Figure 25A). Both show a series of broad resonances with considerable FP character at small diameters (Figure 25B), which become increasingly WG mode like at larger diameters (Figure 25C-E). This suggests that the spatial heterogeneity observed within these single structures would also be present when illuminating the entire structure, as is done for ensemble measurements.

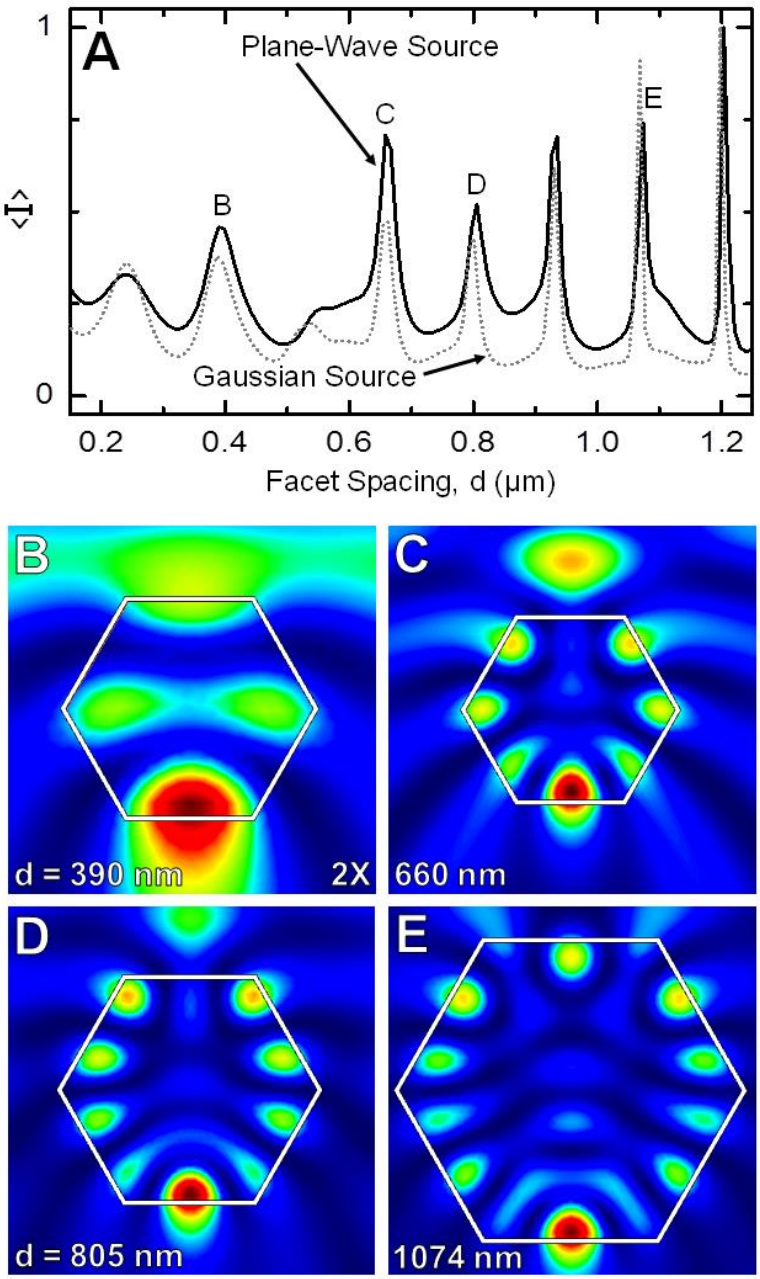

Figure 25: (A) Plot of the average intensity $\left(\langle I\rangle = \int |E|^2 dA\,/A_{hex}\right)$ as a function of facet spacing for the plane wave source (black) and the Gaussian source (gray, dotted), calculated by integrating each column of the simulated image in Figure 24. (B-E) Spatial intensity maps $(|E|^2)$ of several of the simulated resonant modes for the plane-wave excitation source.

3.5.2. Implications

Transient absorption microscopy experiments from our group shows that electron-hole recombination in the tips of these structures occurs primarily through band-edge states, whereas in the interior locations it is dominated by trapping[25, 26]. The qualitative difference between the WG and FP type modes offer a plausible explanation for this spatial dependence. In the larger diameter sections, the cavity resonances are almost completely WG in nature, with the largest intensity being located near the surface of the rod. When the optical intensity is concentrated in the periphery of the rod, photoexcited carriers will be produced in the surface depletion zone. The internal field present in this region (*i.e.* band bending) will separate the electrons and holes, resulting in a greater degree of carrier trapping and longer recombination times. The FP modes near the tips of the rods have the optical field localized primarily in the core of the structure. The standing wave patterns produced in these regions may result in the preferential production of photoexcited carriers in the core of the structure. Because of the low carrier mobility, electrons and holes created in this zone would remain there, and experience a lattice environment similar to that of the bulk, accounting for the greater degree of recombination observed at the band edge.

3.6. Conclusions

Two-photon emission microscopy is used to investigate the photoluminescence properties of individual ZnO rods. The rods are 10-20 μm in length with a tapered cross section that varies from 1-2 μm at the midpoint to several hundred nanometers at the ends. This structure, with its tapered ends and hexagonal cross section, results in a complex series of optical resonator modes. Two types of modes typically ascribed to

hexagonal resonators are Fabry-Pérot (FP) modes and whispering gallery (WG) modes. Finite-difference frequency domain methods suggest that resonator modes of these structures are better described as hybrid modes that have both standing wave (Fabry-Pérot) and whispering gallery mode character, whose relative contributions vary along the rod axis. In particular, at the tips of the rod the modes have significant standing wave character, whereas in the larger cross sections, near the rod midpoint, the modes are dominated by whispering gallery mode features.

3.7. Acknowledgement

Funding for this project came from grants from the National Science Foundation, initially CHE-0809045 and later CHE-1213379. The COMSOL simulation software was purchased under a grant from the U. S. Army Research Laboratory and the U. S. Army Research Office under contract number W911NF-04-D-0004. The project also made use of instrumentation purchased by the UNC-EFRC Center for Solar Fuels, an Energy Frontier Research Center funded by the U.S. Department of Energy, Office of Science, Office of Basic Energy Sciences under Award Number DE-SC0001011.

CHAPTER 4. DIRECT IMAGING OF FREE CARRIER AND TRAP CARRIER MOTION IN SILICON NANOWIRES BY SPATIALLY-SEPARATED FEMTOSECOND PUMP–PROBE MICROSCOPY

[Reproduced from Nano letters 13(3), 2013, 1336-40]

4.1. Abstract

We have developed a pump-probe microscope capable of exciting a single semiconductor nanostructure in one location and probing it in another with both high spatial and temporal resolution. Experiments performed on Si nanowires enable a direct visualization of the charge cloud produced by photoexcitation at a localized spot as it spreads along the nanowire axis. The time-resolved images show clear evidence of rapid diffusional spreading and recombination of the free carriers, which is consistent with ambipolar diffusion and a surface recombination velocity of ~104 cm/s. The free carrier dynamics are followed by trap carrier migration on slower time scales.

4.2. Background

The motion of charge carriers through nanoscale structures is of central importance to many emerging technologies in nanoscale electronics, optoelectronics and solar energy conversion[33-38]. Interaction of charge carriers with the surfaces, localized defects and electrical contacts in nanostructured devices can have a profound influence on the migration of electrons and holes through a semiconductor structure. These effects have generally been inferred through optical and electrical measurements that average over an entire structure, or an ensemble of structures, and do not directly measure the local carrier

motion. To acquire this information, methods with sub-micron spatial resolution and picosecond temporal resolution are needed. The pursuit of such methods is not new, and time-resolved optical microscopies have been applied to a broad range of problems[25-27, 39-48]. The most common approaches are emission-based but are limited to the picosecond time range and require fluorescent samples. Pump-probe methods provide access to faster time scales but are more difficult to implement. Nevertheless, several recent reports from our group[25, 26], and others[39-45, 47, 48], describe their extension to microscopy, particularly in far-field configurations.

4.3. Experimental

Here, direct imaging of carrier motion in Si nanowires is accomplished using a pump-probe microscope that can excite a structure in one location and monitor the arrival of photoexcited carriers in another. Similar examples[49-52] have appeared in the literature. In this work, we present results with diffraction-limited pump-probe beams that provide a high (sub-micron) lateral resolution. This unique configuration permits the collection of spatially-separated pump-probe (SSPP) *images,* allowing direct visualization of the carrier population over time. This capability permits us to distinguish between rapid free carrier motion and the slower migration of trapped carriers, as discussed below.

Intrinsic Si nanowires (i-Si) were grown by a vapor-liquid-solid (VLS) mechanism[53] using a home-built, hot-wall chemical vapor deposition (CVD) system[34]. For a typical growth run, Au nanoparticles with diameters of ~250 nm were dispersed on Si (100) wafers coated with 600 nm thermal oxide, and these wafers were inserted into the center of a quartz-tube furnace. Nanowires were grown with a total reactor pressure of 40 Torr using a gas flow of 2.00 standard cubic centimeters per minute (sccm) silane and 200

sccm hydrogen as carrier gas. The reactor was held at 600 °C for 2 minutes to nucleate wire growth and then cooled (10 °C/min) to 450 °C for continued wire growth over two hours. For n-type Si nanowires (n-Si), an additional flow of 10.00 sccm phosphine (1000 ppm in hydrogen) was used to provide a source of phosphorus dopant at a relative concentration of ~200:1 Si:P. After completion of wire growth, nanowires were thermally oxidized at 1000 °C for 60 s in 100 Torr flowing oxygen to form a 5-10 nm-thick thermal oxide. Nanowires were then mechanically transferred onto quartz substrates for microscopy imaging.

The transient absorption microscope is illustrated in Figure 26. The 850 nm output of a mode-locked Ti:Sapphire oscillator is split by a 10/90 beam splitter. The higher power beam is frequency doubled to 425 nm and used as the pump while the other is used as the probe. Two synchronized acousto-optic modulator (AOM) pulse pickers reduce the repetition rates of the pump and probe beams to 1.6 MHz, thus ensuring complete relaxation before the next pump-probe pulse pair arrives at the sample. A motorized linear stage controls the time delay between excitation and probe pulses. Both the pump and probe beams are attenuated to 20 pJ per pulse, recombined using a dichroic beam splitter, and then directed onto the back aperture of a 50x (0.8 NA) objective that focuses them to diffraction limited spots within a single structure. Diffraction limited spatial resolution in our instrument has been confirmed in two-photon emission images[26]. Images of an asymmetric Au feature on a quartz substrate (Figure 26C) obtained using the pump and probe beams (Figure 26D) are consistent with diffraction-limited focusing of the two spots, with the pump spot being smaller than the probe. The probe beam is collected by a condenser lens, filtered to remove residual pump light, and directed onto a

balanced photodiode. The pump beam is modulated at 10 kHz using the AOM, and pump-induced changes in the intensity of the probe pulse are monitored by a digital lock-in amplifier, producing the measured change in intensity, ΔI, plotted in the figures discussed below. The time-resolution of the instrument is ~500 fs[25, 26].

4.4. Results And Discussion

Initial experiments were performed by measuring kinetics from spatially overlapped pump and probe beams positioned 3-5 μm from the end of three nanowire samples (Figure 27). We estimate that photoexcitation by the pump pulse produced ~10^{19}-10^{20} carriers/cm^3 assuming an absorption efficiency of 10-100% at the excitation wavelength of 425 nm[35, 36]. Pump-probe transient signals are shown for two i-Si wires, NW1 and NW2, and an n-Si wire, NW3, with diameters of 160, 210, and 330 nm, respectively. Exact locations of excitation are indicated on the respective SEM images in Figure 27. The two i-Si NW transient signals exhibit an intense positive going (bleach) feature that becomes weakly negative (absorptive) at several 100 ps before returning to zero signal. These transient signals are similar to pump-probe measurements performed on ensembles of Si nanowires[54]. The signals include contributions from the free carrier (electron and hole) and trap carrier populations and can arise from changes in absorptivity and/or reflectivity upon photoexcitation as well as carrier lensing effects due to the spatially localized excitation[25, 26].

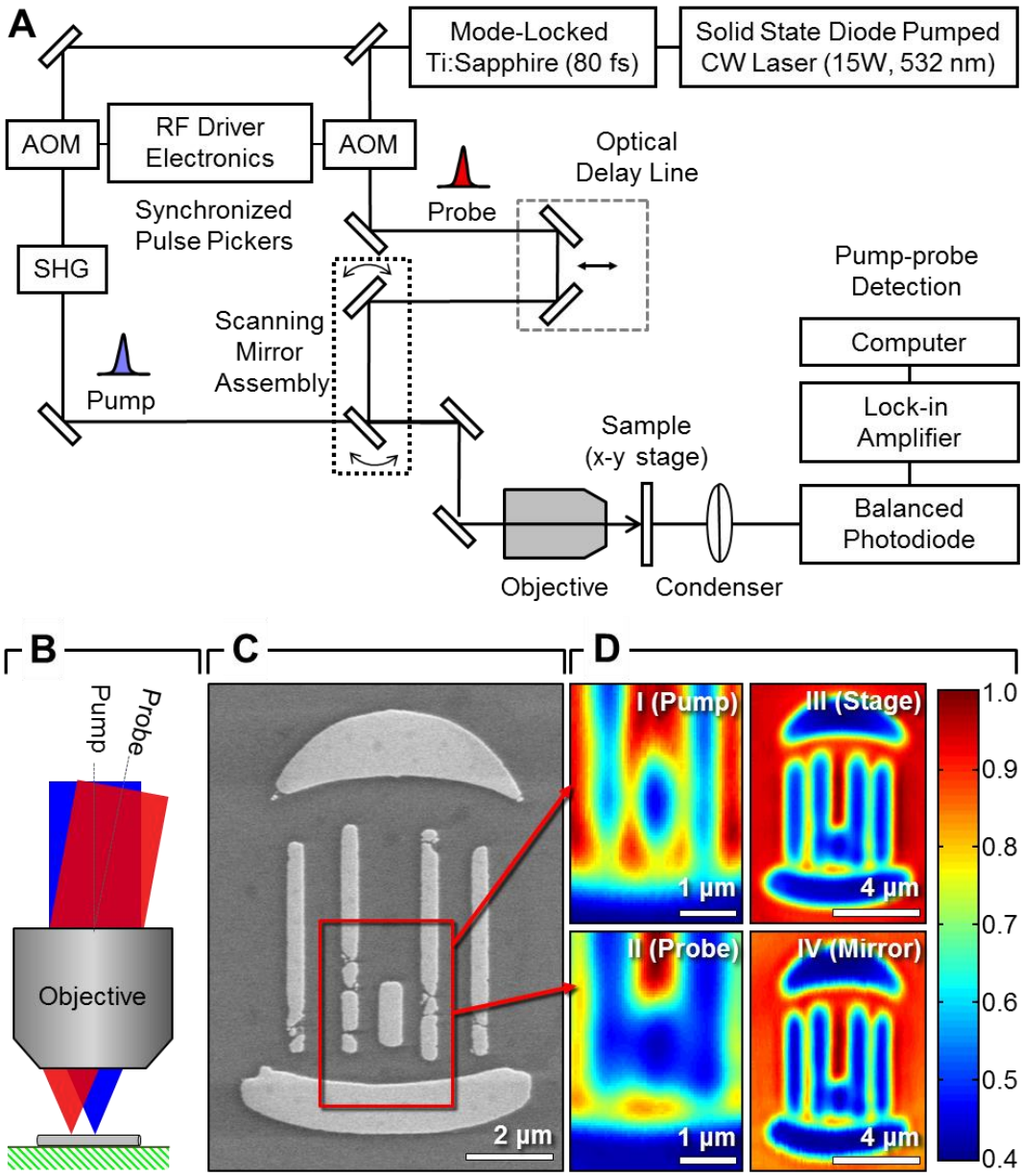

Figure 26: Overview of the experimental system. (A) Illustration of the spatially-separated pump-probe (SSPP) microscope. An x-y scanning stage positions the structure under the 425 nm pump spot; the 850 nm probe spot is positioned relative to the pump with a scanning mirror assembly. (B) Schematic illustration of spatially separated scanning. (C) SEM image of the UNC logo defined in Au by electron-beam lithography; scale bar, 2 µm. (D) Left, optical transmission images obtained with the pump (I) and probe (II) beams scanned over the upper-right portion of the Au structure, as denoted by the inset box in panel C, that contains an ~400 nm gap; scale bars, 1 µm. Red indicates maximum transmission and blue minimum transmission. Right, comparison of transmission images acquired by raster-scanning the probe beam over the entire Au structure shown in panel C using either the x-y stage (III) or the mirror assembly (IV); scale bars, 4 µm.

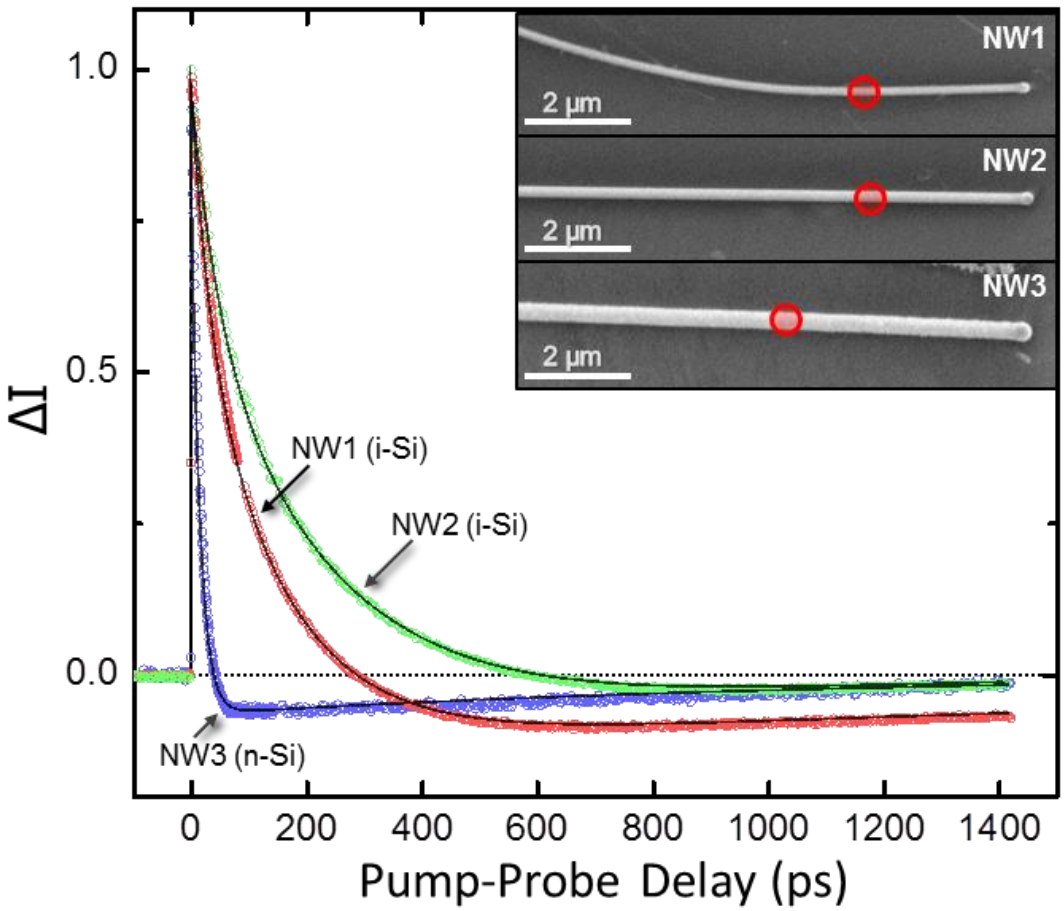

Figure 27: Normalized pump-probe microscopy decay kinetics following photoexcitation of a localized region in three different Si nanowires; NW1 (red) and NW2 (green) are intrinsic, NW3 (blue) is n-type. All three were fit to a triexponential decay (solid lines, see Table 10 for fitting parameters). Inset: SEM images of the three wires showing the location of pump excitation as a red circle; scale bars, 2 µm.

Table 10: Parameters used to fit kinetics derived from pump-probe microscopy to a sum of three exponentials, $\Delta I(t)=A_1e^{-t/\tau 1} + A_2e^{-t/\tau 2}+ A_3e^{-t/\tau 3}$.

	$\tau_1(A_1)$		τ_2 (A_2)		τ_3 (A_3)		τ_{avg}[a]
NW1	29.8 ps	(0.34)	144 ps	(0.78)	2300 ps	(-0.12)	67 ps
NW2	46.8 ps	(0.34)	248 ps	(0.87)	551 ps	(-0.23)	112 ps
NW3	1.75 ps	(0.06)	15 ps	(1.01)	1146 ps	(-0.07)	11 ps

[a] Average decay time for the two fast components, i.e. $(1/\tau_{Avg}) = [(A_1/ \tau_1) + (A_2/ \tau_2)]/(A_1+A_2)$

All three transient signals can be well fit to a superposition of a positive going signal that decays with biexponential kinetics (τ_1, τ_2), and a smaller negative going signal with a much slower decay time, τ_3 (see Table 10). The n-Si wire transient depicted in Figure 27 has been inverted (i.e. multiplied by -1). The reason this wire shows an initial absorption rather than a bleach is not entirely clear; however, in other experiments on ZnO we observed[34] similar sign-changes that stemmed from a Kerr lensing contribution (in addition to absorptive features) to the overall signal. This contribution could either be positive or negative, depending upon the details of the pump-probe overlap. This process could be at play in this wire. The two i-Si wires exhibit different decay kinetics, with NW1 showing a faster initial decay (τ_{avg} = 67 ps) than NW2 (τ_{avg} = 112 ps), but with a slower recovery time back to zero signal, τ_3 = 2300 ps (NW1) versus 551 ps (NW2). We attribute the initial decay to free carrier recombination and diffusion and the slower component to trap recombination. For semiconductor nanowires, surface recombination is often the predominant recombination mechanism, and the surface recombination velocity, S, can be calculated from the carrier lifetime, τ, as $S = d/4\tau$, where d is the nanowire diameter[34, 55-57]. The values derived from this analysis using the measured τ_{avg} are 6.0×10^4 cm/s and 4.7×10^4 cm/s for NW1 and NW2, respectively. These values are upper limits to the actual surface recombination velocities because Auger recombination and carrier diffusion (discussed below) also contribute to the decay. Nevertheless, the similarity between the S values for these two wires suggests that the initial decay is dominated by a surface recombination mechanism.

The n-Si wire (NW3) shows a much faster initial decay (τ_{avg} = 11 ps) and recovers with τ_3 = 1146 ps. The origin of the much faster decay in the n-Si wire is possibly a

result of increased Auger recombination due to the high electron majority-carrier concentration. A second possibility is the presence of an amorphous Si shell surrounding the crystalline core, as suggested by the rougher surface and larger diameter observed in the SEM image. Regardless of the exact origin, the electron-hole recombination rate in this n-Si wire is substantially greater than the i-Si wires.

In order to characterize the diffusion process in the Si nanowires, we have directly imaged charge carrier motion using SSPP microscopy, in which the structure is excited in one location and probed in another. This experiment is accomplished by incorporating two separate positioning mechanisms for the pump and probe beams. The pump spot is positioned over a particular point in the structure through adjustment of the x-y sample stage. Independent placement of the probe beam is accomplished by directing it through a pair of mirrors with computer-controlled actuators, which vary the angle of the probe beam relative to the fixed pump beam (Figure 26C). The use of two (master/slave) mirrors allows adjustment of this angle while keeping the beam centered on the objective aperture. By scanning this angle, the position of the focused probe spot can be displaced from the pump by a distance (Δ_{pp}) of 10-20 μm while still remaining within the objective's field of view. Figure 26D compares transmission images taken using the scanning mirror assembly and the scanning stage. Both transmission images reproduce not only the general shape, but also the finer details of the structure, and the similarity of these two images to the SEM image demonstrates the distortion-free imaging capability of this scanning mechanism.

The SSPP microscope can be operated in two different modes. In one operational mode, the delay time between the pump and probe beams is held fixed and the spatial

displacement of the pump and probe is scanned, resulting in an image of the spatial variation in the transient absorption signal at a particular time after photoexcitation. SSPP images are shown for three different nanowires (NW1, NW2 and NW3) in Figure 28. At early pump-probe delays (near $\Delta t = 0$ ps), the images show an intense positive (red) transient absorption feature, with a spatial extent commensurate with the size of the pump spot. For the i-Si wires (NW1 and NW2), this spot spreads rapidly along the long axis of the nanowire, growing 4-5 μm in length during the first 300-500 ps. At the pump-probe delay time in which the transient signal crosses zero (refer to Figure 27), a trough appears at the location of the excitation spot that eventually becomes a net negative signal. The final images show the positive features disappearing altogether, leaving behind a negative (blue) region that broadens on a slow time scale. We attribute the rapid evolution of the intense positive signal to the diffusion of free carriers (electrons and holes) out of the excitation volume and the negative signal at long times to trap carrier motion. Rapid electron-hole recombination in the n-Si wire (NW3), on the other hand, limits the extent of spatial diffusion and the initial feature shows no substantial broadening.

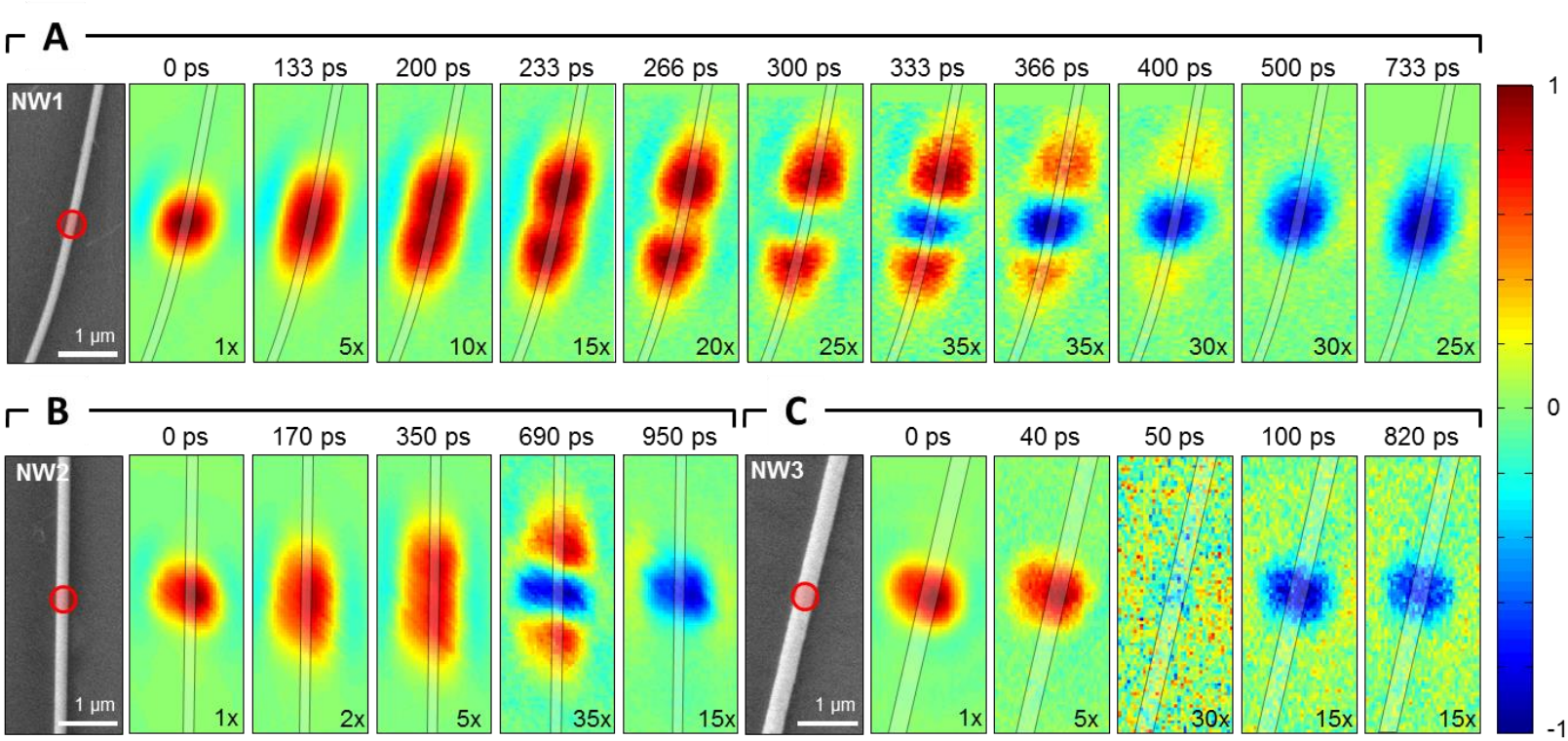

Figure 28: Time-resolved SSPP microscopy images. (A) NW1, (B) NW2, and (C) NW3. Left, SEM images of 5 µm sections of each wire centered around the pump laser excitation spot; (image sizes, 2 µm x 5 µm; scale bars, 1 µm). The location of the excitation spot is depicted by the red circle. For each sample, the tip of the wire lies beyond the top of the image. Right, series of SSPP images acquired at the pump-probe delay times denoted above each image. Location of the nanowire is depicted by the faint lines. Each image is 2 µm x 5 µm and is depicted using a normalized color scale with the relative amplitudes indicated by the scaling factors in the bottom-right corner of each image.

The second operational mode of the SSPP microscope fixes the displacement between the pump and probe laser spots and scans the delay time between them. Figure 29 shows decay traces for five different separations, Δ_{pp}, along the NW2 nanowire axis. When the pump and probe are spatially coincident ($\Delta_{pp} = 0$), the maximum signal intensity is observed at $\Delta t = 0$ ps. A delayed rise in the signal is observed when the probe pulse is positioned away from the excitation spot ($\Delta_{pp} > 0$), reflecting the time needed for carriers to migrate from the pump region to the probe region. There is also an overall decrease in the intensity of the signal as the pump-probe separation is increased. At $\Delta_{pp} = 2.32$ μm, the overall intensity of the signal makes it difficult to discern the arrival of carriers when depicted on an absolute scale (Figure 29); however, when the transients are displayed normalized to their respective maxima (Figure 30A), it is clear that free carriers are migrating as far as 2.7 μm from the excitation region. These time-resolved data indicate that the spatially coincident pump-probe transient signals shown in Figure 27 are influenced by the diffusional motion of charge carriers away from the excitation region. In principal, the summation of transient signals obtained at different pump-probe separations (shown as the curve Σ in Figure 29) should reflect the total free carrier population and remove effects from diffusional motion. This curve is well fit to a superposition of decays with positive and negative amplitudes; however, unlike the $\Delta_{pp} = 0$ μm signal, the decay of the positive signal in the superposition is reproduced by a single exponential with time constant of $\tau = 380$ ps, providing a more accurate measure of the free carrier lifetime. This value for τ gives a revised surface recombination velocity for NW2 of 1.4×10^4 cm/s, which is comparable to the value, $S = 7 \times 10^3$ cm/s, determined for wires grown under similar growth conditions[34].

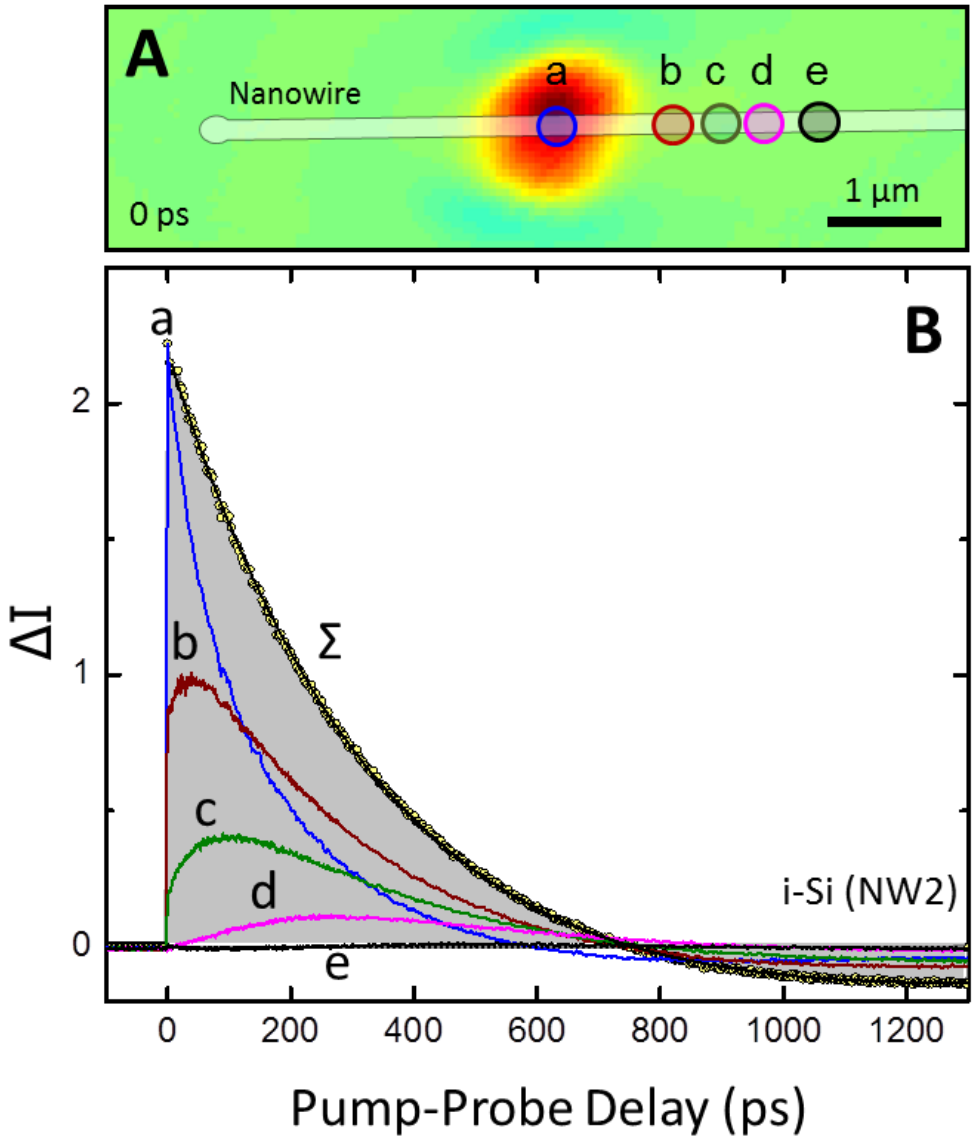

Figure 29: Spatially separated pump-probe (SSPP) transient signals. (A) SSPP image obtained at $\Delta t = 0$ overlaid with the spatial locations, a-e, of the displaced probe beam, which correspond to separations of $\Delta_{pp} = 0$, 1.02, 1.45, 1.83, and 2.32 µm, respectively; scale bar, 1 µm. (B) Transient signals obtained from NW2 by fixing the spatial separation, Δ_{pp}, between the pump and probe spots and scanning the pump-probe delay. The curves labeled a-e correspond to the positions indicated in panel A. Also shown is the transient signal, labeled Σ, obtained by summation of the individual SSPP signals. Individual data points are denoted by open yellow circles and the solid line is a fit to $\Delta I(t) = A_1 e^{-t/\tau 1} + A_2 e^{-t/\tau 2}$ with τ_1 = 380 ps (A_1 = 3.21) and τ_2 = 900 ps (A_2 = -1.02).

In order to quantitatively interpret the charge carrier motion observed with SSPP microscopy, we have developed a simple model that includes ambipolar diffusion of the free carrier population, a recombination process with a single first-order rate constant ($1/\tau$), and Gaussian profiles that represent the pump and probe laser beams centered at x = 0 and $x = \Delta_{pp}$, respectively. In this model, the number of carriers interacting with the displaced probe beam can be written as:

$$N(\Delta_{pp}, t) = \int_{-\infty}^{\infty} I(x - \Delta_{pp})\eta(x,t)dx, \quad (1)$$

where $I(x\text{-}\Delta_{pp})$ is a normalized Gaussian centered at $x = \Delta_{pp}$ that describes the intensity profile of the probe beam, and $\eta(x,t)$ is the carrier distribution created by the pump pulse. At t = 0 this distribution will mirror the intensity profile of the pump beam and spread with increasing time. It can be written as:

$$\eta(x,t) = \int_{-\infty}^{\infty} I(x')p(x - x', t)dx, \quad (2)$$

where $I(x)$ is the optical intensity profile of the focused pump laser beam used in the experiment (represented by a normalized Gaussian) and $p(\xi,t)$ describes the diffusional spreading of N carriers from an initial point located at ξ=0, i.e.:

$$p(\xi, t) = \frac{N}{\sqrt{4\pi Dt}} \exp\left(-\frac{1}{t}\right) \exp\left(-\frac{\xi^2}{4Dt}\right). \quad (3)$$

In this expression τ is the free carrier lifetime and D is the ambipolar diffusion constant[58].

Figure 30 compares this diffusional model (Eq. 1) with the experimentally observed SSPP transient signals from NW2. The experimental data shows a steady increase in the spreading of the carrier cloud, reaching several microns in a few hundred picoseconds. The calculated curves (Figure 30B) were obtained using the ambipolar diffusion constant

for bulk Si ($D \sim 18$ cm^2/s) and a carrier lifetime $\tau = 380$ ps. The calculated curves qualitatively resemble those observed in the SSPP experiment, indicating that diffusional processes in Si nanowires grown by a VLS mechanism are remarkably similar to those in single-crystalline bulk Si materials. There are differences, however, particularly at smaller pump-probe displacements and shorter time delays. In this regime, the model predicts a greater extent of diffusion than observed experimentally, a difference which could be the result of changes in the diffusion constant because of carrier scattering within the nanowires. The exact reasons are currently under investigation.

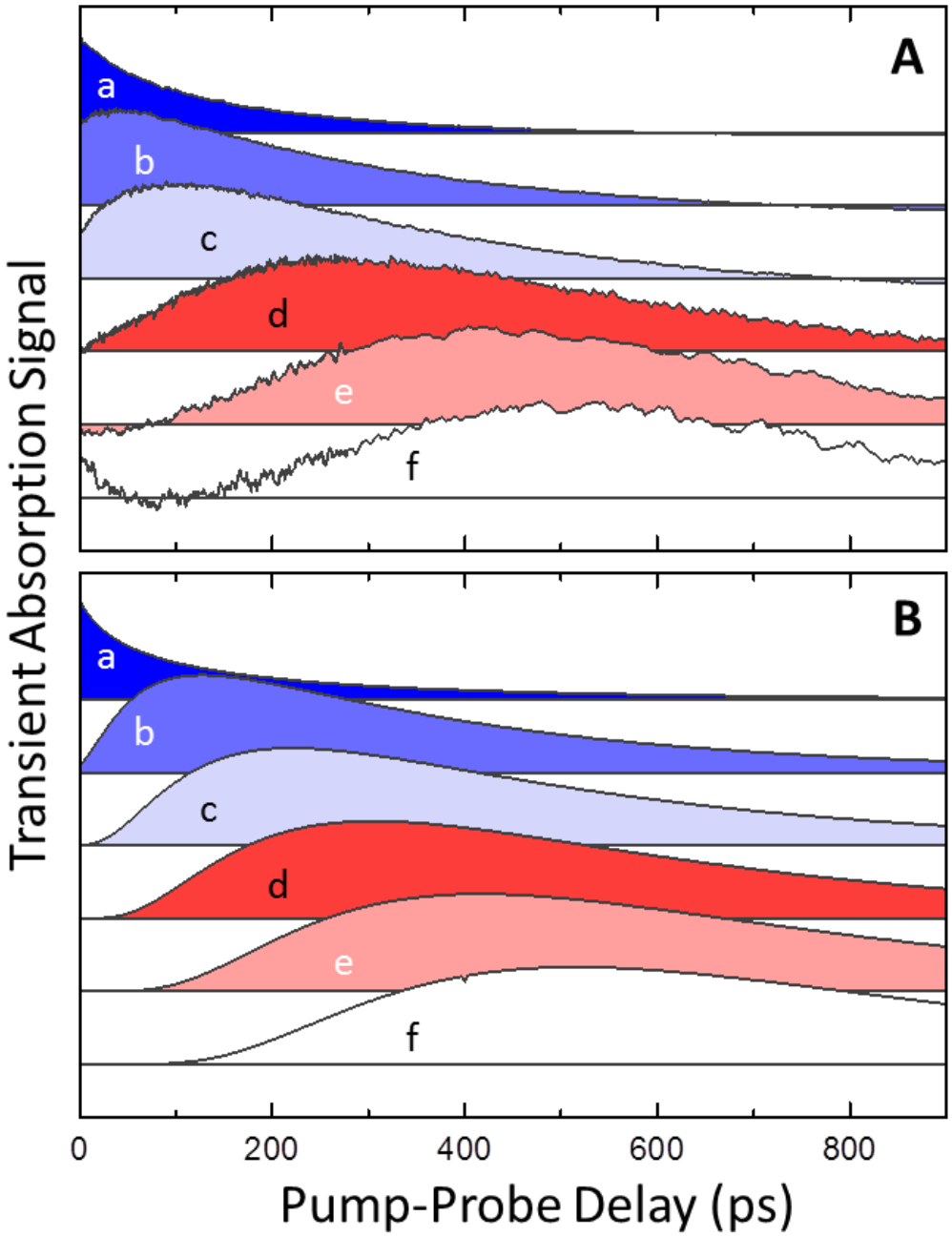

Figure 30: Experimental and simulated transient signals (A) Normalized SSPP transient signals obtained from NW2. The curves labeled a-f correspond to separations Δ_{pp} = 0, 1.02, 1.45, 1.83, 2.32 and 2.76 µm, respectively. (B) Analogous set of SSPP curves predicted by Eq. 1 using D = 18 cm^2/s and τ = 380 ps. The pump and probe laser profiles have FWHM values of 350 nm and 700 nm, respectively, and are included in the simulation curves.

4.5. Conclusions

We have developed a pump-probe microscope capable of photoexciting a single nanostructure in one location and probing it in another. Experiments performed on Si nanowires enable a direct visualization of the charge cloud produced by photoexcitation of a localized spot and spreading of this cloud along the nanowire axis. The time resolved images show clear evidence of rapid diffusion and recombination of the free carries followed by trap carrier migration on slower time scales.

4.6. Acknowledgement

This work was supported by a grant from the National Science Foundation (CHE-1213379). J.D.C, C.W.P, and J.F.C acknowledge support from UNC-Chapel Hill start-up funding.

CHAPTER 5. ANALYSIS OF RECOMBINATION MECHANISMS IN HIGHLY DOPED SILICON NANOWIRES

5.1. Abstract

Ultrafast pump-probe microscopy was used to characterize the surface recombination velocities of phosphorous-doped silicon nanowires. Electron-hole recombination kinetic scans were collected on silicon nanowires containing regions with different phosphorous doping concentration in order to investigate the effect of doping on the surface recombination velocity. Additionally, the effects of surface trap passivation on the recombination velocity were studied by comparing three different surface treatments. The wires showed faster recombination rates in the higher doped segments, which can be attributed to a combination of Auger and surface recombination. Application of the surface treatments lowered the calculated recombination velocities in the nanowires, most likely due to improved surface quality.

5.2. Background

Recent attempts to enhance charge separation in solar cells have placed a greater focus on using silicon nanowires in solar devices. While nanowire based solar cells have the potential to provide higher conversion efficiency, they generally have higher recombination values, which shortens the free carrier lifetime by several orders of magnitude[57]. Shorter lived carriers greatly reduce the solar conversion efficiency of nanowire-based devices, limiting them to only a few percent[59-61].

Carrier recombination in semiconductors is attributed to several processes occurring at both the material surface and in the bulk: Surface Recombination, Shockley-Read-Hall (SRH), and Auger, and radiative recombination. However, in indirect band-gap semiconductors the process of radiative recombination requires interaction with a phonon, drastically lowering the probability of occurrence to the point where it can be neglected. Both Auger and Shockley-Read-Hall (bulk) recombination are dependent on the concentration of dopants and traps in the material[62, 63]. However, Auger recombination is dependent on the total carrier concentration, meaning that it takes into account the population of carriers created by the excitation. This makes Auger recombination much faster than SRH, making it the dominant mechanism in systems where excitation creates a large population of carriers. The effects of doping density on the recombination rate of carriers in silicon films is well documented[64-66], however, nanowires are still relatively undocumented.

The available studies to date suggest that the higher surface to volume ratio makes surface recombination is the dominant mechanism in silicon nanowires[57, 67, 68]. As such, there have been several methods developed to passivate the surface trap states, typically by coating the surfaces with oxides or amorphous silicon[68-70]. These coatings effectively eliminate dangling bonds and surface traps in the nanowire, overall improving the surface quality and resulting in longer carrier lifetimes. As these surface treatments are developed, new methods must be designed to characterize their efficacy[70, 71].

Using the spatially-separated pump-probe microscope, we have been able to take advantage of ultrafast high-resolution transient absorption measurements to analyze silicon nanowires with segments of various phosphorous doping concentrations ranging

from $5x10^{17}$ cm^{-3} to $5x10^{19}$ cm^{-3} separated by segments of intrinsic doping. Furthermore, we have been able to characterize the effects of various surface treatments on the surface recombination rate.

5.3. Experimental

The experiments were conducted using the pump-probe microscope configuration shown in Figure 31A. The pulse train from the mode-locked Ti:Sapphire was tuned to 850 nm and split into two beams. The probe beam was kept at 850 nm, and the pump beam was frequency doubled (BBO crystal) to 425 nm. Both pump and probe were sent through pulse pickers to produce a 1.6 MHz pulse rate. The pump beam was then modulated at a rate of 16 kHz (50% duty cycle) before being directed into the sample. The power of the pump beam was 10 pJ per pulse, corresponding to ~10^{19}-10^{20} carriers/cm^3 created per pump pulse given 10-100% absorption dependent on the silicon nanowire.

The silicon nanowires were grown by Dr. James Cahoon's group at UNC using a home-built, hot-wall chemical vapor deposition (CVD) system, consisting of a quartz tube furnace, mass-flow controllers, a pressure control system, and a high-throughput vacuum system. A more detailed description of the system is discussed in previous literature[34, 72].

For a typical NW growth run, 100 nm Au catalysts were dispersed on a silicon wafer substrate. These growth substrates were inserted into the center of the tube furnace, and the furnace temperature was ramped to 450° C to nucleate NW. The reactor temperature was then cooled (1 °C/min) to 420° C and different doping levels were encoded by introducing PH_3 gas with a tightly controlled flow profile, as discussed in the text[34, 72].

After growth, wires from the sample were transferred to three different substrates for surface treatment. Three different surface treatments were applied to the wires: native (untreated) oxide, thermal oxide, and thermal oxide followed by annealing in a hydrogen rich environment.

The native oxide samples were transferred to a slide with no surface modification allowing for the formation of a native silicon dioxide layer. This naturally occurring layer is approximately 1 nm thick and is formed when silicon is exposed to air under ambient conditions[73, 74].

The thermal oxide treatment consisted of holding the sample at 1000°C in a 100 Torr oxygen environment, resulting in the formation of a silicon dioxide (SiO_2) layer of 8-9 nm thickness. Two samples were exposed to this surface treatment, one of which was further treated with a hydrogen anneal.

The hydrogen annealed treatment consisted of placing a thermally oxidized sample in a 95:5 Argon/Hydrogen environment. The temperature was held at 600° C for 20 min, slowly ramped down to 300° C over the course of 110 minutes, and held for an additional 30 minutes.

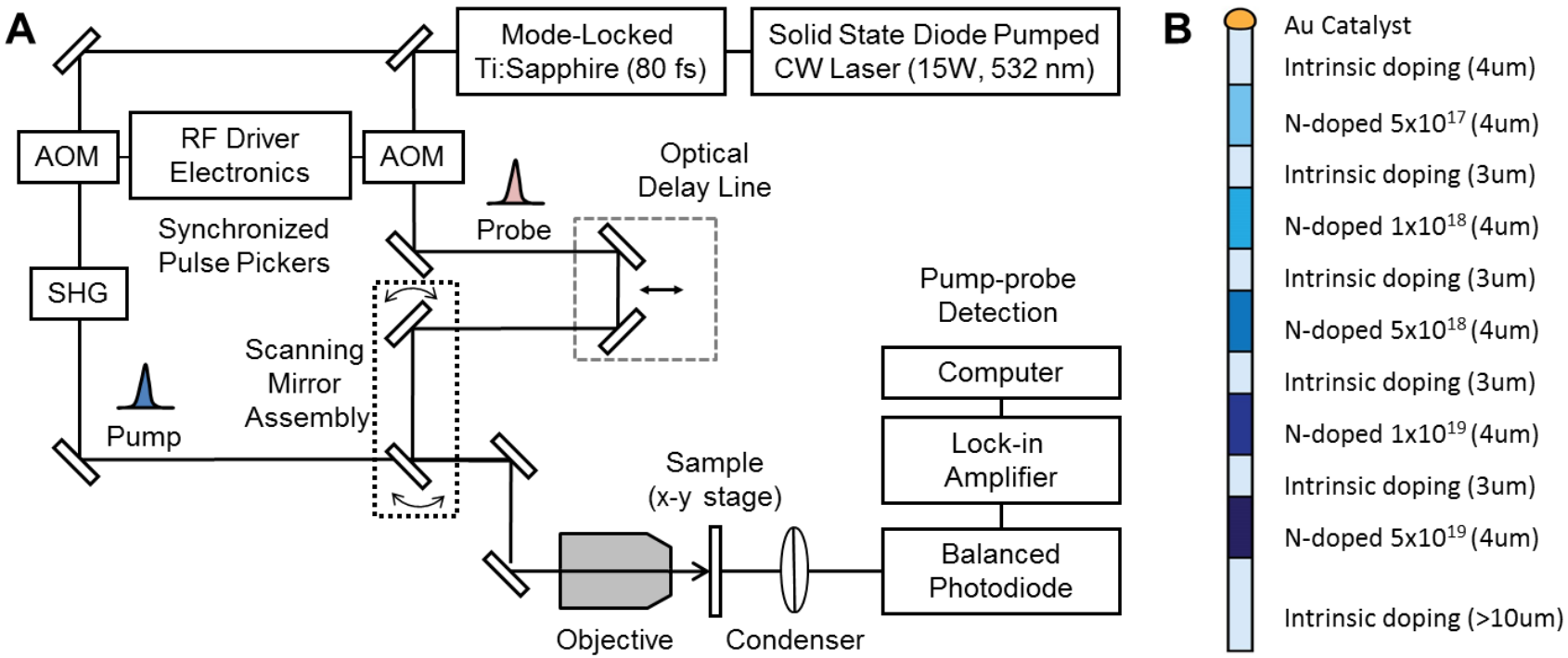

Figure 31: Experimental overview. (A) Illustration of the spatially-separated pump-probe (SSPP) microscope. (B) Diagram of the doping composition of the wires studied.

5.4. Results and Discussion

Experiments to characterize the recombination rates in the segmented silicon nanowires consisted of collecting images and transient absorption scans with the pump and probe beam spatially overlapped.

Spatially-overlapped pump-probe images were collected by setting the probe beam at a constant delay and raster scanning the sample stage under the collinear pump and probe beams. The resulting transient absorption signal at each coordinate was plotted as a function of the position of the stage, forming a 2-D map of the pump-induced transient absorption at that delay. By collecting images at different delays, the evolution of the pump-induced effect on the wire can be visualized as a function of time.

Using the collected images, points were selected that correspond to the middle of each of the doped segments in a nanowire. By placing the overlapped beams over the selected locations in the sample, transient absorption measurements were collected by scanning the delay line and recording the pump-induced changes in the probe intensity.

These spatially overlapped pump probe (SOPP) measurements are similar to the transient absorption measurements discussed in previous literature from our group[26, 75]. The decay kinetics of the transient absorption signal can be attributed to a superposition of contributions from several physical processes in the wire. Each of these change the amount of pump intensity transmitted through the sample, resulting in either a lower optical density (positive signal) or a higher optical density (negative signal). In these experiments, the higher doped regions of the nanowires were strongly dominated by the faster Auger recombination process, while the recombination in the lower doped regions was attributed to slightly slower surface recombination.

5.4.1. Auger Recombination

Auger recombination is a three-particle interaction process where an excited electron-hole pair transfers its energy into a third carrier. The third carrier is excited and releases its energy non-radiatively, in the form of phonon modes. Because this process requires the interaction of an excited e-h pair with a third carrier, it typically only occurs in non-equilibrium systems[76-79]. The higher n-doped regions of the silicon nanowires, paired with Exciton formation by the laser pulses, create conditions that are favorable for Auger recombination.

Using the number of carriers created by the pump excitation, and the materials doping concentration, Auger decay times can be predicted by the relationship[76-79]:

$$\tau_{Aug} = 1/\beta n^2 \quad (1)$$

where β is the material dependent Auger coefficient (1.6 x 10^{-30} cm^6/s for silicon)[80] and n is the concentration of majority carriers. The value of n used in this calculation is the sum of the number of doped electrons and the number of electron-hole pairs created by each pump pulse.

Table 11 contains the predicted Auger lifetimes expected for various doping concentrations and pulse energies. The highlighted line contains the values for the number of carriers expected for the laser power used for these experiments.

Table 11: Calculated Auger Recombination Decay Constants at Relevant Laser Powers.

Pulse Energy (pJ/pulse)	Phosphorous Doping Concentration					
	$5x10^{20}$ cm^{-3}	$1x10^{20}$ cm^{-3}	$5x10^{19}$ cm^{-3}	$1x10^{19}$ cm^{-3}	$5x10^{18}$ cm^{-3}	$1x10^{18}$ cm^{-3}
15	1.96	23.12	47.76	112.91	129.77	146.12
8	2.19	34.65	87.95	318.47	404.66	501.57
2.5	2.40	51.65	173.61	1562.50	2777.78	5165.29

5.4.2. Native Oxide Nanowires

Transient absorption pump-probe images of a native oxide wire taken at different delays are shown in Figure 32. There are distinct regions of the wire that decay at different rates. Measurements taken from the images match the size and placement of the regions in the images to those expected by the doping profile shown in Figure 31B. These indicate that the regions with higher doping concentrations (red, green, and magenta arrows) correspond to locations where the signal fades faster, implying faster recombination in these regions, consistent with results seen in previous work on doped silicon[64-66].

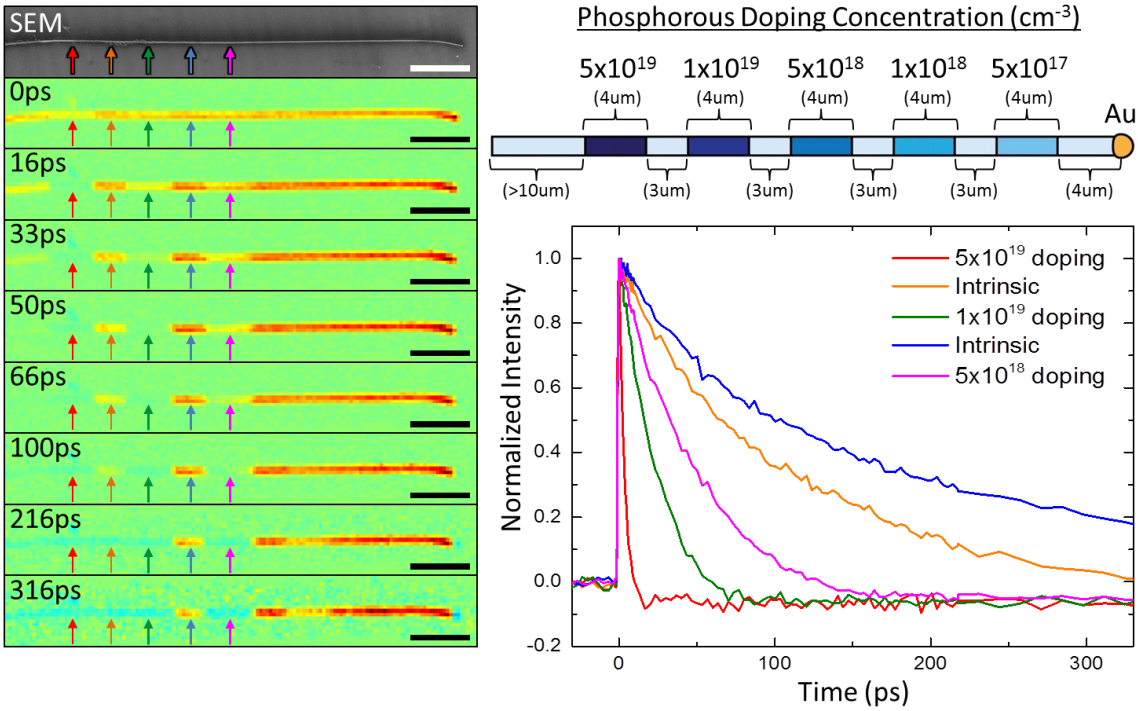

Figure 32: Data from a native oxide wire. (Left) Spatially overlapped images of a single wire with a 5um scale bar. Arrows indicate the locations where SOPP scans were collected. (Upper right) Map of the doping concentration in a wire. (Lower right) Transient absorption pump-probe scans collected at the points along the wire. The color of the arrows in the spatially overlapped images match the color of the data collected at that location.

Transient absorption pump-probe scans were collected at the points marked by the corresponding colored arrows shown in Figure 32. For each native oxide wire studied, the decay kinetics for each doping level were fit to a superposition of a positive going signal that decays with either single or bi-exponential kinetics. The highest doping levels ($5x10^{20}$ cm^{-3}, $1x10^{20}$ cm^{-3}, $5x10^{19}$ cm^{-3}) fit better to a single exponential decay, and the remaining two doping levels ($1x10^{19}$ cm^{-3}, $5x10^{18}$ cm^{-3}) had a longer decay term that required a bi-exponential fit. Table 12 contains the average of the bi-exponential fit parameters (τ1, τ2, A1, A2) from all the studied native oxide wires.

Table 12: Averaged Fitting Parameters For the Native Oxide Sample.

Parameters Used to Fit Native Oxide Wires, $\Delta I(t) = A_1 e^{-t/\tau_1} + A_2 e^{-t/\tau_2}$

Doping (cm^{-3})	τ_1 (A_1) (ps)	τ_2 (A_2) (ps)	T_{avg}^{α} (ps)	T_{adj} (ps)	SRV (cm/s)
$5x10^{20}$	2.31 (1.10)	-	2.31	3.68	8.55E+05
$1x10^{20}$	19.79 (1.03)	-	19.79	31.66	8.29E+04
$5x10^{19}$	47.30 (1.06)	-	47.30	75.68	3.47E+04
$1x10^{19}$	79.54 (0.37)	512.04 (0.62)	168.41	269.46	9.74E+03
$5x10^{18}$	108.17 (0.37)	691.87 (0.57	221.96	355.14	7.39E+03

$^{\alpha}$Average decay time for the components, i.e. $(1/\tau_{avg}) = [(A_1/\tau_1) + (A_2/\tau_2)]/(A_1+A_2)$.

Previous studies have attributed this dopant dependent relationship is largely attributed to a combination of effects such as: Auger recombination, majority and minority carrier scattering, and surface aided recombination[64-66, 68, 81]. The lifetimes of the faster decay components (τ_1) are qualitatively similar to the calculated Auger lifetimes (Table 11), indicating that the faster term in the bi-exponential can be assigned to Auger recombination. The longer lifetime of the slower component is most likely due to surface aided recombination.

The regions corresponding to the intrinsically doped segments (orange and blue arrows) experience an overall slower decay than the doped segments, which is expected with a lower doping level. However, all of the intrinsic segments do not decay at the same speed despite being grown under the same conditions. Previous studies have shown that a layer of polycrystalline silicon builds up on the surface of the nanowire, which leads to shorter carrier lifetimes(ref). However, this effect is drastically reduced by lowering the growth temperature, which was done during the growth procedure for these nanowires(ref).

The images show that the decay rate is constant throughout each intrinsic region, which implies that the entire region is uniformly affected during growth. If it were due to the buildup of a polycrystalline coating, the half of the region furthest from the gold catalyst would have a thicker coating and thus, faster decays. This effect is most likely due to small amounts of dopant diffusion radially into the wire during the growth. During the growth of each doped region, all of the previous intrinsic regions would be uniformly exposed to the dopant gas. This means that the doping concentration for the intrinsic unknown, making quantitative analysis of their decay rates impossible.

For ease of comparison between the different samples and doping levels, the biexponential fitting parameters were used to calculate a single term for the average decay time (τ_{avg}) for each doping level using the following relationship:

$$(1/\tau_{avg}) = [(A_1/\tau_1) + (A_2/\tau_2)]/(A_1+A_2) \quad (2)$$

Data from previous SSPP experiments indicated that the time constants found by fitting the obtained transient absorption decays must be adjusted to compensate for the additional decrease in signal from carriers migrating out of the excitation area. Spatially

separated imaging showed that signal decays 60% faster than it would in the absence of carrier motion[75]. Therefore, the average decay times were adjusted to compensate by adding an additional 60%. This adjusted decay constant (τ_{adj}) is listed in Table 12 for each doping concentration.

If we assume that the carrier recombination is dominated by surface recombination as suggested in previous literature[57, 67, 68] an effective surface recombination velocity (SRV) can be calculated from the decay lifetimes. The relationship between surface recombination velocity (SRV) and effective decay constant (τ_{eff}) is defined as[82-84]:

$$\frac{1}{\tau_{eff}} = k_{bulk} + \frac{4(SRV)}{d} \quad (3)$$

where SRV is the surface recombination velocity, d is the nanowire diameter, and k_{bulk} is the bulk recombination rate. Assuming surface recombination is the dominant recombination mechanism in nanowires[57, 67, 68] the bulk recombination rate can be ignored, and the equation simplifies to:

$$SRV = \frac{d}{4\tau} \quad (4)$$

Measurements of the wire diameters were made in the SEM and averaged to provide a collective diameter for the native oxide sample. Using this average diameter and the adjusted decay constant (τ_{adj}) the SRV for each doping concentration was calculated and the results are posted in Table 12.

5.4.3. Thermal Oxide Nanowires

The reduction of the surface recombination velocities of silicon nanowires by thermal oxidation has been shown previously[68, 69]. This had been attributed to a reduction of defects at the nanowire surface, which quenches surface recombination and lengthens

carrier lifetimes. Therefore, thermal oxidation of the segmented nanowires should decrease the decay rates compared to the ones seen in the native oxide sample.

Images and transients absorption scans were collected for several wires with the thermal oxide surface treatment and are presented in Figure 33. The doped regions are still present in the images, although their contrast has decreased. This is better illustrated in the decay plots of the various regions collected at the locations of the colored arrows. The locations were chosen to be the center of the segments as observed in the collected images. Aside from the highest doped region, the transient absorption data for the different regions show similar kinetics.

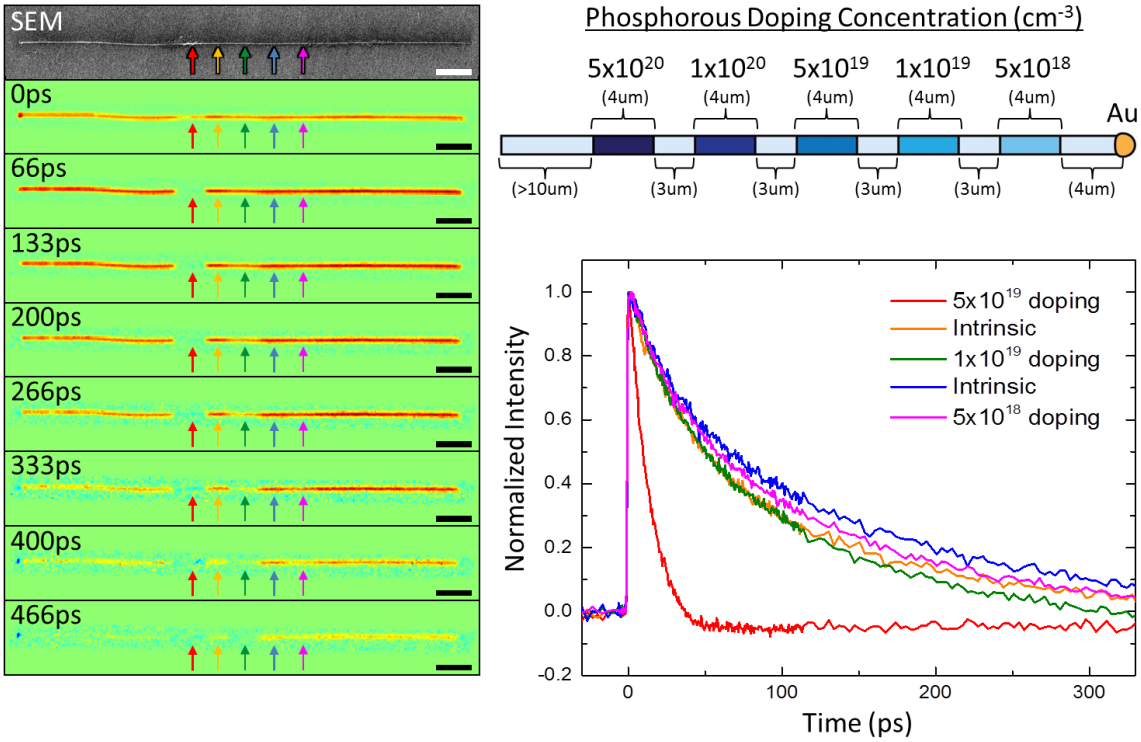

Figure 33: Data from a wire from the thermally oxidized sample. (Left) Spatially overlapped images of a single wire with a 5um scale bar. Arrows indicate the locations where SOPP scans were collected. (Upper right) Map of the doping concentration in a wire. (Lower right) Transient absorption pump-probe scans collected at the points along the wire. The color of the arrows in the spatially overlapped images match the color of transient scan collected at that location.

The averaged bi-exponential fitting parameters for the decay traces of the thermal oxide wires are summarized in Table 13. When compared with the adjusted decay lifetimes from the native oxide sample, the lifetimes from the thermal oxide sample were longer, as expected. Segments of higher doping saw a larger magnitude of change in their decay lifetime. The highest doped segment required a single exponential fit, but the decay time increased by nearly 650%. The next doped region saw ~180% lifetime increase when compared to the native oxide wires, while the $5x10^{19}$ cm^{-3} doped region only increased by ~30%. The transient absorption decay traces from the regions with doping concentrations of $1x10^{19}$ cm^{-3} and $5x10^{18}$ cm^{-3} also required a single exponential fit, due to an absence of the fast decay component.

Table 13: Averaged Fitting Parameters For the Thermal Oxide Sample.

Parameters Used to Fit Thermal Oxide Wires, $\Delta I(t) = A_1 e^{-t/\tau_1} + A_2 e^{-t/\tau_2}$

Doping (cm^{-3})	τ_1 (A_1) (ps)	τ_2 (A_2) (ps)	T_{avg}^{α} (ps)	T_{adj} (ps)	SRV (cm/s)
$5x10^{20}$	14.88 (1.03)	-	14.88	23.80	1.19E+05
$1x10^{20}$	23.81 (0.36)	120.33 (0.69)	54.77	87.63	2.35E+04
$5x10^{19}$	28.20 (0.43)	160.60 (0.61)	60.34	96.55	1.76E+04
$1x10^{19}$	-	212.60 (1.03)	212.60	340.16	7.72E+03
$5x10^{18}$	-	224.38 (1.05)	224.40	359.04	7.31E+03

$^{\alpha}$Average decay time for the components, i.e. $(1/\tau_{avg}) = [(A_1/\tau_1) + (A_2/\tau_2)]/(A_1+A_2)$.

5.4.4. Hydrogen Annealed Nanowires

High temperature annealing in hydrogen following the thermal oxidation process is often performed in order to passivate any remaining trap states at the Si-SiO_2 interface. This has been shown to decrease the interfacial defect density by an order of magnitude[53, 58]. Therefore, the decay lifetimes for the hydrogen annealed sample should be longer than in the thermal oxide wires.

The images and transients from the hydrogen annealed sample are shown in Figure 34. Unexpectedly, the different decay rates in the segments are no longer observable in the images. Because the sample was treated with the thermal oxide prior to the hydrogen anneal, transients were collected at distances from the gold catalyst corresponding to the center of the regions in the thermal oxide sample. These transients are color matched to the corresponding arrows in the images. While a general trend of increasing decay time as the distance from the gold catalyst is increased, the previously observed differences between regions are now indiscernible.

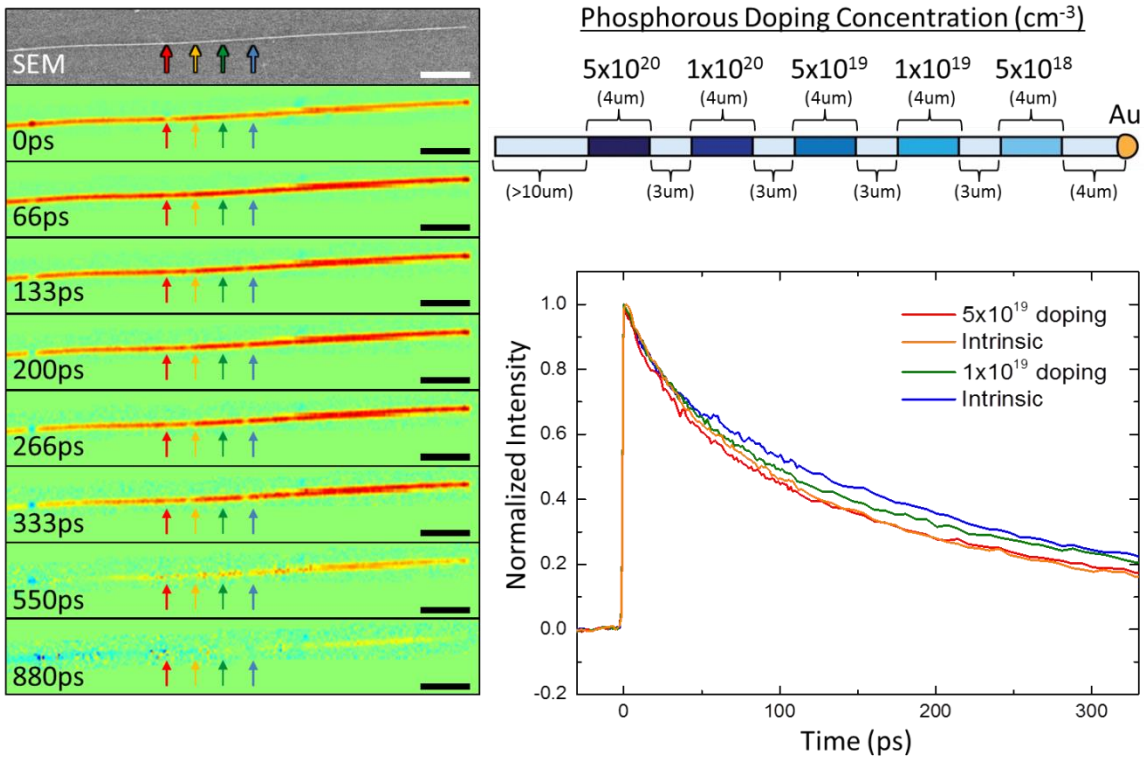

Figure 34: Data from a wire from the hydrogen annealed sample. (Left) Spatially overlapped images of a single wire with a 5um scale bar. Arrows indicate the locations where SOPP scans were collected. (Upper right) Map of the doping concentration in a wire. (Lower right) Transient scans collected at the points along the wire. The color of the arrows in the spatially overlapped images match the color of transient scan collected at that location.

The calculated fitting parameters for the predicted doping levels for the hydrogen annealed wires are shown in Table 14. The transients collected at all points on the hydrogen annealed wires well to a bi-exponential decay function, showing lower decay lifetimes throughout the wire, which agrees with the expected result.

Table 14: Averaged Fitting Parameters For the Hydrogen Annealed Sample.

Parameters Used to Fit Hydrogen Annealed Wires, $\Delta I(t) = A_1 e^{-t/\tau_1} + A_2 e^{-t/\tau_2}$

Doping (cm^{-3})	τ_1 (A_1) (ps)	τ_2 (A_2) (ps)	T_{avg}^{α} (ps)	T_{adj} (ps)	SRV (cm/s)
$5x10^{20}$	47.69 (0.30)	273.15 (0.74)	56.74	90.78	2.89E+04
$1x10^{20}$	56.58 (0.38)	384.87 (0.68)	119.11	190.58	1.38E+04
$5x10^{19}$	95.51 (0.40)	494.38 (0.61)	158.44	253.51	1.04E+04
$1x10^{19}$	79.61 (0.39)	532.92 (0.56)	218.68	349.88	7.50E+03
$5x10^{18}$	74.31 (0.39)	684.93 (0.77)	217.38	347.81	7.55E+03

$^{\alpha}$Average decay time for the components, i.e. $(1/\tau_{avg}) = [(A_1/\tau_1) + (A_2/\tau_2)]/(A_1+A_2)$.

The nearly uniform decay rate throughout the wire suggests that the dopants may have diffused evenly throughout the wire. However, calculations of dopant diffusion distances in silicon at 600° C limit motion to less than 100 nm[58]. The etching rates of silicon nanowires are dependent on the dopant concentration; therefore the existence of the doped segments after the hydrogen annealing process was verified by etching wires from the sample.

A plot of surface recombination velocity versus doping level for all three surface treatments is shown in Figure 35. As a reference, data collected on the effect of doping density on surface recombination velocities in silicon slabs is plotted[64, 66]. The linear regression of this data is represented as a solid black line. To date, no comparable study exists that discusses the effects of doping concentration on surface recombination velocities in silicon nanowires. The available literature on the subject suggests that the large surface to bulk ratio will result in higher SRV values overall[57, 67, 68].

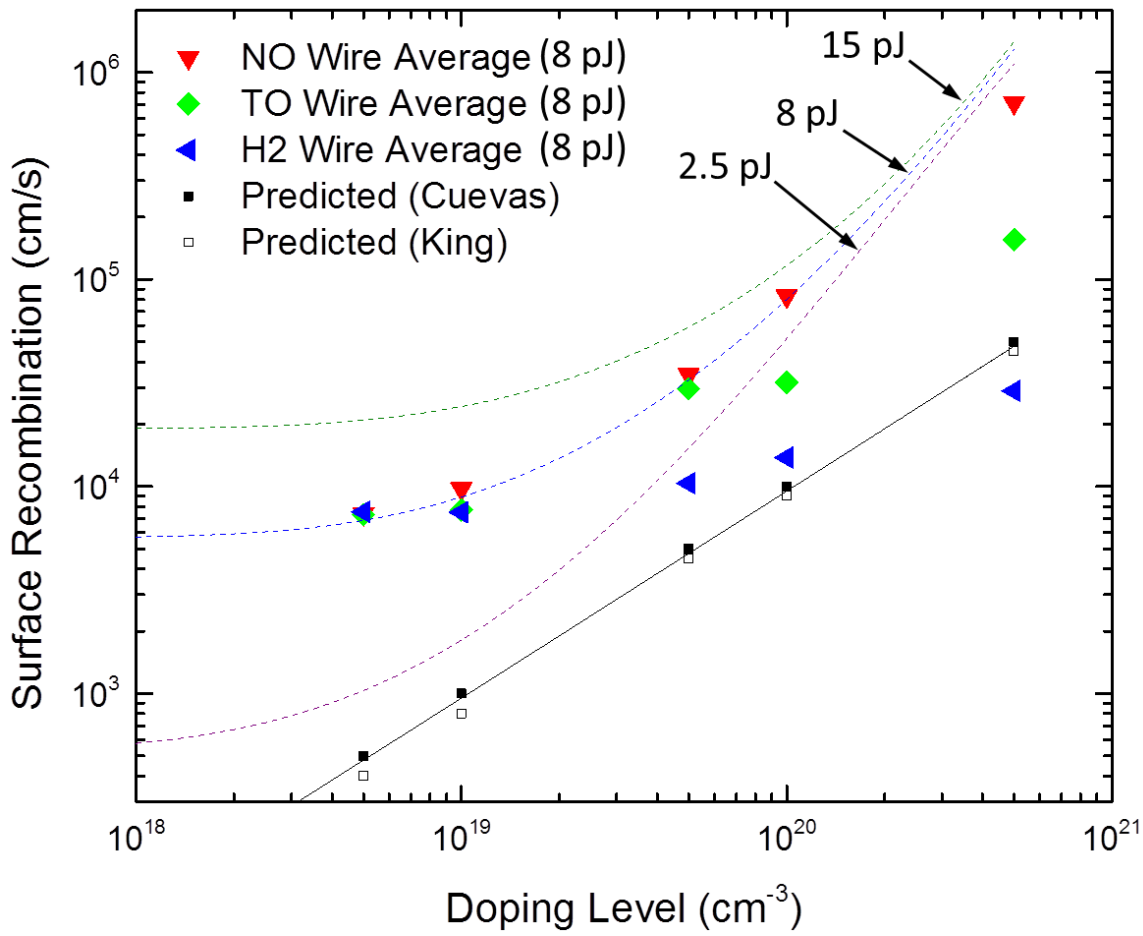

Figure 35: Surface recombination rate as a function of doping concentration for all three surface treatments. Values from previous literature (King, Cuevas) are plotted (black and white squares) for reference along with the fit shown as a solid black line. The dashed lines represent the calculated Auger upper limits in Table 11 for three pulse energies: 15 pJ, 8 pJ, and 2.5 pJ.

To provide an upper limit for the surface recombination values, the calculated Auger decay lifetimes from Table 11 were substituted into equation 4 for τ. This effectively returns SRV values for the case that Auger is the only recombination mechanism.

The dotted lines on the plot represent the surface recombination values calculated from the Auger lifetimes for different pulse energies. The dotted curve for the 8 pJ pulse energy is closest to what would be expected given the laser powers used in this experiment. The data point for the highest doping level falls below this curve, which

could be attributed to dopant saturation preventing doping concentrations over the previously observed $1.5x10^{20}$ cm^{-3} limit[85]. However, overall the points corresponding to the native oxide wires closely follow the Auger curve for the experimental pulse energy. This supports the idea that Auger is the dominant recombination process in native oxide wires. The calculated SRV values for the thermal oxide and hydrogen annealed samples remain below the plotted 8 pJ curve, implying that Auger plays less of a role in their decay. At lower doping concentrations the SRV values decrease for all samples; however, they remain an order of magnitude above the literature values for bulk silicon.

The plots for all three samples show the trend of increasing surface recombination velocity as the doping level increases, but the trend is different for each sample. The hydrogen annealed sample has the lowest slope, and the native oxide sample has the highest. This indicates that the surface treatments have reduced the dependence of the SRV values on the doping concentration, which agrees with previous reports[53, 58, 68-70]. This is good evidence that the thermal oxide and hydrogen annealing surface treatments effectively passivate the surfaces of the wire with a high quality layer of SiO_2.

However, at lower doping concentrations the data from all three samples converge to an asymptotic value. The change in surface recombination due to surface passivation diminish as the lower doping concentrations studied, resulting in all three samples having the same SRV in the $5x10^{18}$ cm^{-3} doped region. Interestingly, this asymptotic limit is quantitatively similar to the upper limit predicted from the Auger decay rates for the pump powers used in these experiments. This suggests that as the number of carriers created in each laser pulse approaches the doping concentration, the Auger recombination begins to overpower the surface recombination mechanism. Doping concentrations over

$1x10^{18}$ cm^{-3} are considered to be in the high injection regime, where Auger processes are considered to play a role.

Reducing the pump power until the number of carriers introduced into the sample is below the doping level may be the only way to find accurate values of surface recombination velocity at lower doping levels. Further experiments that vary both the doping level and the excitation power would provide a better understanding of how Auger recombination affects the pump probe signal in silicon nanowires.

5.5. Conclusions

Wires with segments of different doping concentrations and surface treatments were studied using ultrafast pump-probe microscopy. While a direct relationship exists between doping concentration and surface recombination velocity, the faster Auger recombination process tends to dominate the slower surface recombination process. This makes it difficult to extract accurate surface recombination velocities for higher doped silicon nanowires.

Overall, the thermal oxidation and hydrogen annealing surface treatments reduced the recombination rates. The higher doped regions of the wires saw a drastic increase in carrier lifetime after surface treatment, while the lower doped regions approached an asymptotic limit.

Reliable quantitative analysis will require experiments that investigate lower excitation powers to fully eliminate the contribution of Auger recombination in the measured signal decay. In future experiments, care should be taken to ensure that excitation powers used are low enough to reduce the effects of Auger recombination to a negligible amount.

CHAPTER 6. CONCLUSIONS

The constant opposition between carrier creation and recombination in semiconductor materials is a complex dynamic. Excited charge carriers must interact with defects, surfaces, lattice vibrations, and even other charge carriers, each of which offers a new obstacle to impede their motion. In nanoscale materials, this is further complicated by a greater degree of confinement, larger surface to volume ratio, and other shape dependent complications. Characterizing the role of these processes in nanomaterials and using the information to increase carrier lifetimes is important to the incorporation of nanoscale-materials into novel optical and electrical technologies. To improve the performance of these materials, researchers seek answers to questions such as: How does a particle's geometry affect carrier creation and migration?

Answering this question is the main focus of this dissertation. While this is a formidable task that will most likely require decades of research, experiments performed using the spatially-separated pump-probe microscope has revealed preliminary glimpses at the answers. Analyzing the role that geometry plays in the spatial distribution of excited carriers in single nanostructures is addressed for the hexagonal ZnO nanowires (Chapter 3). Excited carrier behavior in silicon nanowires was investigated by direct imaging (Chapter 4) and doping dependent transient absorption studies (Chapter 5). These preliminary results pave the way for future experiments which will be continued by future graduate students in the Papanikolas group. As these experimental techniques

are used and further developed, they will have a great impact on the understanding of nanomaterial properties.

REFERENCES

1. Zewail AH, Ortalan V. 4D scanning transmission ultrafast electron microscopy: Single-particle imaging and spectroscopy. Journal of the American Chemical Society. 2011 Jul 20;133(28):10732-5.

2. Pohl DW, Denk W, Lanz M. Optical stethoscopy - image recording with resolution lambda/20. Applied Physics Letters. 1984;44(7):651-3.

3. Betzig E, Trautman JK. Near-field optics - microscopy, spectroscopy, and surface modification beyond the diffraction limit. Science. 1992 Jul 10;257(5067):189-95.

4. Binning G, Rohrer H, Gerber C, Weibel E. Surface studies by scanning tunneling microscopy. Physical Review Letters. 1982;49(1):57-61.

5. Mehl BP. Investigation of optical cavity modes and ultrafast carrier dynamics in ZnO rods using second-harmonic generation and transient absorption pump-probe microscopy electronic resource] [dissertation]. Chapel Hill, N.C.: University of North Carolina at Chapel Hill; 2011.

6. Wang ZL. Zinc oxide nanostructures: Growth, properties and applications. Journal of Physics: Condensed Matter. 2004;16(25):R829.

7. Ozgur U, Alivov YI, Liu C, Teke A, Reshchikov MA, Dogan S, et al. A comprehensive review of ZnO materials and devices. Journal of Applied Physics. 2005 Aug 15;98(4):041301.

8. Djurišić AB, Leung YH. Optical properties of ZnO nanostructures. Small. 2006;2(8-9):944-61.

9. van Vugt LK, Rühle S, Ravindran P, Gerritsen HC, Kuipers L, Vanmaekelbergh D. Exciton polaritons confined in a ZnO nanowire cavity. Phys Rev Lett. 2006;97(14):147401.

10. Rühle S, Van Vugt L, Li H, Keizer N, Kuipers L, Vanmaekelbergh D. Nature of sub-band gap luminescent eigenmodes in a ZnO nanowire. Nano letters. 2008;8(1):119-23.

11. Zimmler MA, Bao J, Capasso F, Muller S, Ronning C. Laser action in nanowires: Observation of the transition from amplified spontaneous emission to laser oscillation. Appl Phys Lett. 2008;93(5):051101,051101-3.

12. Dai J, Xu CX, Wu P, Guo JY, Li ZH, Shi ZL. Exciton and electron-hole plasma lasing in ZnO dodecagonal whispering-gallery-mode microcavities at room temperature. Appl Phys Lett. 2010 Jul;97(1).

13. Nobis T, Kaidashev EM, Rahm A, Lorenz M, Grundmann M. Whispering gallery modes in nanosized dielectric resonators with hexagonal cross section. Phys Rev Lett. 2004;93(10):103903.

14. Czekalla C, Sturm C, Schmidt-Grund R, Cao B, Lorenz M, Grundmann M. Whispering gallery mode lasing in zinc oxide microwires. Appl Phys Lett. 2008;92(24):241102,241102-3.

15. Yang YH, Zhang Y, Wang NW, Wang CX, Li BJ, Yang GW. ZnO nanocone: Application in fabrication of the smallest whispering gallery optical resonator. Nanoscale. 2011;3(2):592-7.

16. Sun L, Chen Z, Ren Q, Yu K, Bai L, Zhou W, et al. Direct observation of whispering gallery mode polaritons and their dispersion in a ZnO tapered microcavity. Phys Rev Lett. 2008;100(15):156403.

17. Liu J, Lee S, Ahn Y, Park J, Koh KH, Park KH. Identification of dispersion-dependent hexagonal cavity modes of an individual ZnO nanonail. Appl Phys Lett. 2008;92(26):263102,263102-3.

18. Czekalla C, Nobis T, Rahm A, Cao BQ, Zuniga-Perez J, Sturm C, et al. Whispering gallery modes in zinc oxide micro- and nanowires. Phys Status Solidi B. 2010 Jun;247(6):1282-93.

19. Nobis T, Grundmann M. Low-order optical whispering-gallery modes in hexagonal nanocavities. Physical Review A. 2005;72(6):063806.

20. Zhang Y, Zhou HJ, Liu SW, Tian ZR, Xiao M. Second-harmonic whispering-gallery modes in ZnO nanotetrapod. Nano Letters. 2009 May;9(5):2109-12.

21. Gargas DJ, Moore MC, Ni A, Chang S, Zhang Z, Chuang S, et al. Whispering gallery mode lasing from zinc oxide hexagonal nanodisks. ACS nano. 2010;4(6):3270-6.

22. Yang YH, Dong JW, Wang NW, Yang GW. Whispering gallery mode enhanced luminescence from an individual ZnO micro- and nanoscaled optical resonator. J Appl Phys. 2011 May 1;109(9):093511-7.

23. House RL, Kirschbrown JR, Mehl BP, Gabriel MM, Puccio JA, Parker JK, et al. Characterizing Electron–Hole plasma dynamics at different points in individual ZnO rods. The Journal of Physical Chemistry C. 2011;115(43):21436-42.

24. Mehl BP, House RL, Uppal A, Reams AJ, Zhang C, Kirschbrown JR, et al. Direct imaging of optical cavity modes in ZnO rods using second harmonic generation microscopy†. The Journal of Physical Chemistry A. 2009;114(3):1241-6.

25. Mehl BP, Kirschbrown JR, House RL, Papanikolas JM. The end is different than the middle: Spatially dependent dynamics in ZnO rods observed by femtosecond Pump–Probe microscopy. The Journal of Physical Chemistry Letters. 2011;2(14):1777-81.

26. Mehl BP, Kirschbrown JR, Gabriel MM, House RL, Papanikolas JM. Pump-probe microscopy: Spatially resolved carrier dynamics in ZnO rods and the influence of optical cavity resonator modes. Journal of Physical Chemistry B. 2013:ASAP Article (10.1021/jp307089h).

27. House RL, Mehl BP, Kirschbrown JR, Barnes SC, Papanikolas JM. Characterizing the ultrafast charge carrier trapping dynamics in single ZnO rods using two-photon emission microscopy. The Journal of Physical Chemistry C. 2011;115(21):10806-16.

28. Nobis T, Grundmann M. Low-order optical whispering-gallery modes in hexagonal nanocavities. Physical Review A. 2005;72(6):063806.

29. Cheng B, Samulski ET. Hydrothermal synthesis of one-dimensional ZnO nanostructures with different aspect ratios. Chemical Communications. 2004(8):986-7.

30. Li F, Li Z, Jin FJ. Structural and luminescent properties of ZnO nanorods prepared from aqueous solution. Mater Lett. 2007;61(8):1876-80.

31. Zipfel WR, Williams RM, Webb WW. Nonlinear magic: Multiphoton microscopy in the biosciences. Nat Biotechnol. 2003;21(11):1369-77.

32. Postava K, Sueki H, Aoyama M, Yamaguchi T, Ino C, Igasaki Y, et al. Spectroscopic ellipsometry of epitaxial ZnO layer on sapphire substrate. J Appl Phys. 2000 Jun 1;87(11):7820-4.

33. Kelzenberg MD, Turner-Evans DB, Putnam MC, Boettcher SW, Briggs RM, Baek JY, et al. High-performance si microwire photovoltaics. Energ Environ Sci. 2011 Mar;4(3):866-71.

34. Christesen JD, Zhang X, Pinion CW, Celano TA, Flynn CJ, Cahoon JF. Design principles for photovoltaic devices based on si nanowires with axial or radial p-n junctions. Nano Lett. 2012 Nov;12(11):6024-9.

35. Kempa TJ, Cahoon JF, Kim SK, Day RW, Bell DC, Park HG, et al. Coaxial multishell nanowires with high-quality electronic interfaces and tunable optical cavities for ultrathin photovoltaics. P Natl Acad Sci USA. 2012 Jan 31;109(5):1407-12.

36. Kim SK, Day RW, Cahoon JF, Kempa TJ, Song KD, Park HG, et al. Tuning light absorption in core/shell silicon nanowire photovoltaic devices through morphological design. Nano Lett. 2012 Sep;12(9):4971-6.

37. Tahara T, Fujino T, Fujima T. Femtosecond fluorescence dynamics imaging using a fluorescence up-conversion microscope. Journal of Physical Chemistry B. 2005 Aug 18;109(32):15327-31.

38. Warren WS, Fu D, Ye T, Matthews TE, Grichnik J, Hong L, et al. Probing skin pigmentation changes with transient absorption imaging of eumelanin and pheomelanin. Journal of Biomedical Optics. 2008 Sep-Oct;13(5).

39. Johnson JC, Knutsen KP, Yan H, Law M, Zhang Y, Yang P, et al. Ultrafast carrier dynamics in single ZnO nanowire and nanoribbon lasers. Nano Letters. 2004;4(2):197-204.

40. Djurišic AB, Kwok WM, Leung YH, Phillips DL, Chan WK. Stimulated emission in ZnO nanostructures: A time-resolved study. The Journal of Physical Chemistry B. 2005;109(41):19228-33.

41. Fujino T, Fujima T, Tahara T. Femtosecond fluorescence dynamics imaging using a fluorescence up-conversion microscope. The Journal of Physical Chemistry B. 2005;109(32):15327-31.

42. Fu D, Ye T, Matthews TE, Grichnik J, Hong L, Simon JD, et al. Probing skin pigmentation changes with transient absorption imaging of eumelanin and pheomelanin. J Biomed Opt. 2008;13(5):054036,054036-7.

43. Gundlach L, Piotrowiak P. Femtosecond kerr-gated wide-field fluorescence microscopy. Opt Lett. 2008;33(9):992-4.

44. Song JK, Willer U, Szarko JM, Leone SR, Li S, Zhao Y. Ultrafast upconversion probing of lasing dynamics in single ZnO nanowire lasers. The Journal of Physical Chemistry C. 2008;112(5):1679-84.

45. Carey CR, Yu Y, Kuno M, Hartland GV. Ultrafast transient absorption measurements of charge carrier dynamics in single II− VI nanowires. The Journal of Physical Chemistry C. 2009;113(44):19077-81.

46. House RL, Kirschbrown JR, Mehl BP, Gabriel MM, Puccio JA, Parker JK, et al. Characterizing Electron–Hole plasma dynamics at different points in individual ZnO rods. The Journal of Physical Chemistry C. 2011;115(43):21436-42.

47. Huang L, Hartland GV, Chu L, Feenstra RM, Lian C, Tahy K, et al. Ultrafast transient absorption microscopy studies of carrier dynamics in epitaxial graphene. Nano letters. 2010;10(4):1308-13.

48. Polli D, Grancini G, Clark J, Celebrano M, Virgili T, Cerullo G, et al. Nanoscale imaging of the interface dynamics in polymer blends by femtosecond Pump-Probe confocal microscopy. Adv Mater. 2010;22(28):3048-51.

49. Ruzicka BA, Zhao H. Optical studies of ballistic currents in semiconductors [invited]. JOSA B. 2012;29(2):A43-54.

50. Seo M, Yoo J, Dayeh S, Picraux S, Taylor A, Prasankumar R. Mapping carrier diffusion in single silicon Core–Shell nanowires with ultrafast optical microscopy. Nano letters. 2012;12(12):6334-8.

51. Kumar N, Ruzicka BA, Butch N, Syers P, Kirshenbaum K, Paglione J, et al. Spatially resolved femtosecond pump-probe study of topological insulator bi_ {2} se_ {3}. Physical Review B. 2011;83(23):235306.

52. Seo MA, Dayeh SA, Upadhya PC, Martinez JA, Swartzentruber BS, Picraux ST, et al. Understanding ultrafast carrier dynamics in single quasi-one-dimensional si nanowires. Applied Physics Letters. 2012 Feb 13;100(7):071104.

53. Schmidt V, Wittemann JV, Gosele U. Growth, thermodynamics, and electrical properties of silicon nanowires. Chem Rev. 2010 Jan;110(1):361-88.

54. Kar A, Upadhya PC, Dayeh SA, Picraux S, Taylor AJ, Prasankumar RP. Probing ultrafast carrier dynamics in silicon nanowires. Selected Topics in Quantum Electronics, IEEE Journal of. 2011;17(4):889-95.

55. Kelzenberg MD, Turner-Evans DB, Putnam MC, Boettcher SW, Briggs RM, Baek JY, et al. High-performance si microwire photovoltaics. Energy & Environmental Science. 2011;4(3):866-71.

56. Mohite AD, Perea DE, Singh S, Dayeh SA, Campbell IH, Picraux ST, et al. Highly efficient charge separation and collection across in situ doped axial VLS-grown si nanowire p-n junctions. Nano Lett. 2012 Apr;12(4):1965-71.

57. Allen JE, Hemesath ER, Perea DE, Lensch-Falk JL, Li ZY, Yin F, et al. High-resolution detection of au catalyst atoms in si nanowires. Nat Nanotechnol. 2008 Mar;3(3):168-73.

58. Sze SM, Ng KK. Physics of semiconductor devices. In: Physics of Semiconductor Devices. 3rd Edition ed. Wiley-Interscience; 2007. p. 566.

59. Kempa TJ, Tian BZ, Kim DR, Hu JS, Zheng XL, Lieber CM. Single and tandem axial p-i-n nanowire photovoltaic devices. Nano Lett. 2008 Oct;8(10):3456-60.

60. Tsakalakos L, Balch J, Fronheiser J, Korevaar B, Sulima O, Rand J. Silicon nanowire solar cells. Appl Phys Lett. 2007;91:233117.

61. Kelzenberg MD, Turner-Evans DB, Kayes BM, Filler MA, Putnam MC, Lewis NS, et al. Photovoltaic measurements in single-nanowire silicon solar cells. Nano letters. 2008;8(2):710-4.

62. Gaubas E, Vanhellemont J. Comparative study of carrier lifetime dependence on dopant concentration in silicon and germanium. J Electrochem Soc. 2007;154(3):H231-8.

63. Bleichner H, Jonsson P, Keskitalo N, Nordlander E. Temperature and injection dependence of the Shockley–Read–Hall lifetime in electron irradiated n-type silicon. J Appl Phys. 1996;79(12):9142-8.

64. Cuevas A, Basore PA, Giroult-Matlakowski G, Dubois C. Surface recombination velocity of highly doped n-type silicon. J Appl Phys. 1996;80(6):3370-5.

65. King R, Sinton R, Swanson R. Studies of diffused phosphorus emitters: Saturation current, surface recombination velocity, and quantum efficiency. Electron Devices, IEEE Transactions on. 1990;37(2):365-71.

66. King RR, Swanson RM. Studies of diffused boron emitters: Saturation current, bandgap narrowing, and surface recombination velocity. Electron Devices, IEEE Transactions on. 1991;38(6):1399-409.

67. Gunawan O, Guha S. Characteristics of vapor–liquid–solid grown silicon nanowire solar cells. Solar Energy Mater Solar Cells. 2009;93(8):1388-93.

68. Dan Y, Seo K, Takei K, Meza JH, Javey A, Crozier KB. Dramatic reduction of surface recombination by in situ surface passivation of silicon nanowires. Nano letters. 2011;11(6):2527-32.

69. Krylyuk S, Davydov AV, Levin I, Motayed A, Vaudin MD. Rapid thermal oxidation of silicon nanowires. Appl Phys Lett. 2009;94(6):063113,063113-3.

70. Seo K, Sharma S, Yasseri AA, Stewart DR, Kamins TI. Surface charge density of unpassivated and passivated metal-catalyzed silicon nanowires. Electrochemical and solid-state letters. 2006;9(3):G69-72.

71. Stan G, Krylyuk S, Davydov A, Cook R. Compressive stress effect on the radial elastic modulus of oxidized si nanowires. Nano letters. 2010;10(6):2031-7.

72. Zhang X, Pinion CW, Christesen JD, Flynn CJ, Celano TA, Cahoon JF. Horizontal silicon nanowires with radial pn junctions: A platform for unconventional solar cells. The Journal of Physical Chemistry Letters. 2013.

73. Morita M, Ohmi T, Hasegawa E, Kawakami M, Ohwada M. Growth of native oxide on a silicon surface. J Appl Phys. 1990;68(3):1272-81.

74. Riordan M. The silicon dioxide solution. Spectrum, IEEE. 2007;44(12):51-6.

75. Gabriel MM, Kirschbrown JR, Christesen JD, Pinion CW, Zigler DF, Grumstrup EM, et al. Direct imaging of free carrier and trap carrier motion in silicon nanowires by

spatially-separated femtosecond Pump–Probe microscopy. Nano letters. 2013;13(3):1336-40.

76. Haug A. Carrier density dependence of auger recombination. Solid-State Electronics. 1978;21(11):1281-4.

77. Schmid W. Experimental comparison of localized and free carrier auger recombination in silicon. Solid-State Electronics. 1978;21(11):1285-7.

78. Burhop EHS, Burhop E. The auger effect and other radiationless transitions. University Press Cam-bridge; 1952.

79. Chattarji D. The theory of auger transitions. Academic press; 1976.

80. Goetzberger A, Knobloch J, Voss B. Crystalline silicon solar cells. Wiley; 1998.

81. Klaassen D. A unified mobility model for device simulation—I. model equations and concentration dependence. Solid-State Electronics. 1992;35(7):953-9.

82. Léonard F, Talin AA, Swartzentruber B, Picraux S. Diameter-dependent electronic transport properties of au-catalyst/ge-nanowire schottky diodes. Phys Rev Lett. 2009;102(10):106805.

83. Sinton RA, Swanson RM. Recombination in highly injected silicon. Electron Devices, IEEE Transactions on. 1987;34(6):1380-9.

84. Hangleiter A, Häcker R. Enhancement of band-to-band auger recombination by electron-hole correlations. Phys Rev Lett. 1990;65(2):215.

85. Schmid H, Björk MT, Knoch J, Karg S, Riel H, Riess W. Doping limits of grown in situ doped silicon nanowires using phosphine. Nano Letters. 2008;9(1):173-7.